Dynamics of high-speed-resolved wing and body kinematics of freely flying houseflies responding to directed and undirected air turbulence

Vom Fachbereich Maschinenbau
an der Technischen Universität Darmstadt
zur
Erlangung des Grades eines Doktor-Ingenieurs (Dr.-Ing.)
genehmigte

DISSERTATION

vorgelegt von

M. Nazri M. Nasir, M.Sc.

aus Melaka, Malaysia

Berichterstatter:	Prof. Dr.-Ing. Cameron Tropea
	Prof. Dr. Fritz-Olaf Lehmann
Mitberichterstatter:	
Tag der Einreichung:	8.11.2016
Tag der mündlichen Prüfung:	10.01.2017

Darmstadt 2017
D17

Erklärung

Hiermit erkläre ich, dass ich die vorliegende Arbeit, abgesehen von den in ihr ausdrücklich ge-nannten Hilfen, selbständig verfasst habe.

Kuala Lumpur, 28.10.2016 M. Nazri, M. Nasir

For my late father, Nasir Rahman (1930-2012)

Preface

All praise to all mighty God.
The Lord of the Creation. The Compassionate, the Merciful.

It is a pleasure for me to thank those who made this doctoral thesis possible.

This thesis would not have been possible without the full support of my advisers, Prof. Dr. Fritz-Olaf Lehmann and Prof. Dr.-Ing. Cameron Tropea. Their advice, feedback, scientific guidance, and supervision have enabled me to develop a deep understanding on how insects fly. I highly acknowledge their input that has improved the quality of the thesis significantly. Their kindness, understanding and motivation have been truly invaluable on both academic and personal matters, for which I am profoundly grateful.

I would like to express my deepest and humble gratitude to Universiti Teknologi Malaysia, UTM and Ministry of Education, Malaysia for their financial support and for giving me the ample opportunity to conduct my PhD study in Germany.

I owe sincere and earnest thanks to the management of UTM, especially to the previous Deputy Vice-Chancellor, the late Prof. Dr. Marzuki Khalid who granted my PhD scholarship with one sentence "Nazri, have a good time in Germany!" and to my former Head of Department of Aeronautic, Prof. Dr. Mohammad Nazri bin Mohd Jaafar. His comments and recommendations during selection of the scholarship interview are highly appreciated. I am also deeply indebted to the Dean of the Faculty of Mechanical Engineering Prof. Dr. Roslan Abdul Rahman and Mrs. Norafidah Mohd Mohedin who assisted with my PhD prolongation.

I am most grateful for the given opportunity to work in a state-of-the-art technology laboratory and with an apparatus, provided and supported by the German Science Foundation (DFG). I valued the technical support, equipment, organized seminars and discussions. I appreciate the supplementary financial support by the hosting lab at the University of Ulm.

I would also like to thank Ms Ursula Seifert, for her efficient administrative help throughout my stay in Germany. Ms Seifert has helped me and my family on visa processing, accommodation and office related matters. She often helped me on a last-minutes basis.

Special dedication belongs to my colleagues at the Institute of Neurobiology, University of Ulm. In particular, I would like to mention Dr. Peter Schützner, Dr. Ruben Berthé and Dr. Hao Wang for their warm friendship, help and professional discussions. I also thank the lab technical assistants with whom I worked Hanif Khan, Violetta Cierotzki and Melissa Sonensommer for their support. Next, I thank Dr. Shafiq Flynn for constructive comments and valuable inputs on this thesis.

This PhD thesis would not have been possible without the unwavering support from my family. The thesis is dedicated to my parents, my late father (Nasir Rahman) and mother (Esah Jakip). I owe the deepest gratitude to my father-in-law (Muhamad Mahmood) and mother-in-law (Che Rahmah Mustapha) for their continuous support and prayers. Special thanks also belong to my brothers and sisters (Hajar, Nizar, Ayub, Ramlan, Azizah, Ariffin, Ikram, Azim, Zahid and Zarif), nephews and the community of Chenderah, Jasin.

Last but not least, I am truly thankful to my wife Sarah Azreen for her personal support and patience, our children Ayman Nasaie and Azzan Nasaie, which paved the way to my success. We are very grateful for having such an amazing adventure, beautiful and blissful life in Germany.

Kuala Lumpur, 28.10.2016 M. Nazri, M. Nasir

Abstract

From tiny flies to huge dragonflies, aerial locomotion of insects requires sophisticated biological control strategies and unusual aerodynamic mechanisms. During flight, unpredictable changes of ambient air flow may destabilize body posture and control owing to changes in aerodynamic force production. Pioneering discoveries demonstrated that insects such as flies actively regulate body appendages such as wings, legs and the abdomen to encounter aerial perturbations. To quantify this behaviour, I thus investigated how housefly *Musca domestica* behaved in response to undirected, turbulent air flows and directed impulsive wind gusts. To evaluate theoretical predictions, I three-dimensionally reconstructed body and wing motion using time-resolved high-speed videography and stimulated the freely flying animals under laboratory conditions. Impairments of mechanosensory receptors functionality allowed me to distinguish between active and passive behavioural responses and to investigate the role of sensory feedback for flight control during perturbations.

The results show that houseflies typically do not take-off when mean air velocity exceed ~0.63ms^{-1}, which compares to ~2% relative turbulence intensity. In still air, flies take-off immediately after releasing them and respond to impulsive wind gusts by uniform changes in body posture. The directional dependency of these changes is explained by a numerical aerodynamic based on quasi-steady considerations of interaction between wind gust, body and wing velocities. Shortest behavioural response delays were measured during anterior perturbation, amounting to 2.4ms (yaw axis), 5ms (roll axis) and 7.3ms (pitch axis). Under this condition, flies showed the shortest alteration period of 8ms (pitch), 13ms (roll) and 17.5ms (yaw) compared to other direction of perturbations. Body roll angle changes more strongly (18.5-fold increase) than yaw (7-fold increase) and pitch (6.4-fold increase) in response to gusts, suggesting that roll stability is most sensitive. Houseflies also actively modulate the wing kinematics to recover from aerial perturbations. In response to anterior perturbation, flies reduce mean wingbeat amplitude by ~25%, mean wing elevation angle by ~29% compared to non-perturbated controls. Approximately ~2.5 stroke cycles (~15ms) after perturbation onset, mean wingtip velocity hit the minimum of 3ms^{-1} and flies dynamically soars with little wing movement for 1 stroke cycles within the air stream. While responding to the gust, wing angle of attacks decreases during downstroke by ~45.5% (~60.5° at t=13.5ms) that leads to a decrease in the lift coefficient. This stabilizes lift and body position in vertical axis. During upstroke, by contrast, wing angle of attacks increases 1-fold (~-0.5°

at t=12ms) compared to non-perturbated controls (63±5.4°), which elevates aerodynamic drag on the flapping wings. Owing to the horizontal stroke plane, the latter change augments thrust, propelling forward and compensating for gust-induced forces. The measured response times suggest that the changes in wing kinematics cannot be explained by sensory feedback from the antennae because delays of antennae- and vision-mediated feedback are higher than the measured ones. This suggests that posture stabilization reflexes in flies likely results from feedback mediated by the fly's gyroscopic halteres, signalling postural changes within ~6.7ms (a single wing stroke cycle). This thesis extends our current knowledge on insect free flight control during aerial perturbations by quantifying kinematics and behavioural response delays in houseflies.

Collectively, the study provides time-resolved kinematic data on how flies cope with turbulent and wind gust. Our research delivers a contribution to the answer of the question on how insects achieve their superior flight performance. The presented data on the housefly complement recent studies in other species of flying insects and the findings are also useful in a wide scientific context. The biological flight control strategies may be transferred to the biomimetic, miniaturized micro aerial vehicles propelled by flapping wing motion.

Symbols

	Explanation	Unit
A	Maximum body velocity; amplitude	
c	Chord length of the wing	meter, m
D	Drag	N
DC	Duty cycle	%
I	Turbulence intensity	%
L	Lift	N
l	Height above take-off platform	milimeter, mm
m	Mass	gram, g
N	Number of flies	
n	Wingbeat frequency measured when wing chord was perpendicular to stroke plane	Hertz, Hz
n.s.	$p > 0.05$ (statistically not significant)	
P	Rate of change of body velocity in units per time; period	s
p	Critical level	
R	Wing length	meter, m
R^2	Coefficient of determination	
r	Pearson's correlation coefficient	
r_c	Angular linear correlation of circular statistical analysis	
S	Wing area (single wing)	m^2
t	Recording time (negative = prior the onset of perturbation, positive = during/after perturbation)	s
Δt	Delay or latency	s
u	Speed	ms^{-1}
v	Velocity	ms^{-1}
V	Voltage	V
W	Power	Watt
WBA	Wingbeat amplitude	degree, °
X	x-axis of global coordinate system	milimeter, mm
Y	y-axis of global coordinate system	milimeter, mm
Z	z-axis of global coordinate system	milimeter, mm
x	x-axis of fly centred body coordinate system	milimeter, mm
y	y-axis of fly centred body coordinate system	milimeter, mm
z	z-axis of fly centred body coordinate system	milimeter, mm

Greek symbols	Explanation	Unit
α	Angle between the wing chord and vertical axis; wing angle of attack	degree, °
γ	Direction of airflow or stimulus	degree, °
β	Horizontal deviation angle between flight direction of the fly's centre of gravity and body yaw angle in global coordinate frame	degree, °
ε	Angle between the flight path of an ascending fly and local horizon; body inclination	degree, °
η	Roll angle of the thorax with respect to fly's longitudinal body axis	degree, °
ϕ	Phase shift of the responses	
Φ	Stroke angle of the wing with respect to fly's transversal body axis	degree, °
θ	Elevation angle of the wing with respect to fly's longitudinal body axis	degree, °
ω	Yaw angle of fly's longitudinal axis about the vertical	degree, °
ζ	Offset of the responses	
σ	Standard deviation	
*	Probability, $p \leq 0.05$	
**	Probability, $p \leq 0.01$	
***	Probability, $p \leq 0.001$	
$\vec{\omega}$	Vorticity	s^{-1}
χ	Pitch angle of fly's longitudinal axis with respect to horizon	degree, °

Subscripts	Explanation
$(\ )_a$	Airflow
$(\ )_b$	Body
$(\ )_{ctrl}$	Controls/ non-perturbated
$(\ )_f$	Fly
$(\ )_{DU}$	Transition between downstroke and upstroke wing motion
$(\ )_{UD}$	Transition between upstroke and downstroke wing motion
$(\ )_{max}$	Maximum
$(\ )_{min}$	Minimum
$(\ )_{MD}$	Mid-downstroke
$(\ )_{MU}$	Mid-upstroke
$(\ )_{L/left}$	Left

$(\ )_{R/right}$	Right
$(\ )_{P}$	Pronation
$(\ )_{pert}$	Perturbated
$(\ )_{S}$	Supination
$(\ )_{T}$	Total
$(\ )_{t}$	Wingtip
$(\ )_{w}$	Wing
$(\ )_{DR}$	Dorsal stroke reversal
$(\ )_{VR}$	Ventral stroke reversal
$(\ )_{v}$	Vertical
$(\ )_{h}$	Horizontal
$(\ )_{\omega}$	Yaw
$(\ )_{\chi}$	Pitch
$(\ )_{\eta}$	Roll

Diacritic	**Explanation**	**Unit**
$(\dot{\ })$	First derivatives with respect to time	$(\ )s^{-1}$
$(\bar{\ })$	Average	

Abbreviations	**Explanation**
cw	Clockwise rotation
2D	2-dimensional space
3D	3-dimensional space
LE	Leading edge
TE	Trailing edge
PIV	Particle Image Velocimetry
ROI	Region-of-interest of high-speed cameras
s.d.	Standard deviation
s.e.	Standard error
T-O	Take-off
WISL	Wind-Induced Suppression of Locomotion
WH	Wing hinge
FFT	Fast-Fourier-Transformation

Table of contents

1. Introduction

Flight of animals and airplanes requires the production of aerodynamic forces that are high enough to compensate for both mass of the body and the instabilities of body posture owing to changing airflows and asymmetries in the flight apparatus (Abzug and Larrabee, 2005; Denker, 1996). Stable flight thus requires a set of consecutive corrections to cope with continuous flight instability (Dudley, 2002). Before the Second World War, contradictory control and stability in airplanes received little emphasis since being less stable was perceived as better for manoeuvres, though stability was required to reduce a pilot's workload to overcome unpredictable disturbances (Anderson and Eberhardt, 2009). Airplane flight stability can be ensured through careful weight distribution and accurate adjustment on lifting devices (Stengel, 2004). Similar constraints apply to natural fliers such as insects that produce aerodynamic forces by root flapping wing. They depend on moments of inertia, the symmetry of body posture, the characteristics of environmental airflow (e.g. wind gust, turbulence) and vortex shedding demands (Liu et al., 2012).

In this thesis, I studied the responses of freely flying houseflies, *Musca domestica*, operating in still air, during impulsive wind gust perturbation and turbulent flow under controlled laboratory conditions. I captured flight sequences using a high-speed video apparatus and examined how flies adjust wing and body motion to mitigate the effect of air perturbations. I also explored the link between flight behaviour and responsible elaborate sensory feedback.

This thesis provides results and approaches for researchers interested in motion tracking and videography, experimental fluid dynamics, aerodynamics, biomechanics and the neurobiology of insect.

1-1. Previous work

1-1-1. The differences between insect and airplane flight

The flight of flies differs greatly from a conventional fixed-wing airplane in many aspects including power, lift generation and flight control mechanisms.

Unlike an airplane which uses propellers to generate thrust, flies flap their deformable wings in a complex fashion to simultaneously produce both lift and thrust (Beenakkers, 1969; Dalton, 1975; Fry et al., 2005). Comparing to fixed-winged airplanes, flies unequivocally use different patterns of wing motion and wingtip paths such as the figure of eight, distorted ellipse (Hollick,

1940), with 1 (figure of eight), 2 (Ellington, 1984b) and 3 (Neuhaus and Wohlgemuth, 1960) crossing-overs. Airplanes generate aerodynamic forces by steadily translating the slightly inclined airfoils (ranging from 0 to 12° angle of attack) (Mattingly, 2002). During normal operation, these airfoils operate in laminar flow and at Reynolds number higher than 3×10^7 (Deck et al., 2014). Flies, by contrast, generate aerodynamic forces from time-invariant airflow driven by translating, rotating, wiggling and undulating wings at intermediate ranges of Reynolds number varying from 10-10^4 (Lehmann, 2004; Vogel, 1981; Wang, 2005).

1-1-2. Force and moment control in flying insects

Flight control is the ability to implement active commands to perform specific manoeuvres or to maintain or to change its conditions (Anderson and Eberhardt, 2009). The three primary airplane active flight control devices are the ailerons, elevators, and the rudder. Flies, by contrast, regulate the near-instantaneous alteration of aerodynamic forces by changing wing motion on a stroke-by-stroke basis (Ennos, 1989; Fry et al., 2003; Robertson and Johnson, 1993).

During aerial perturbation, a flying animal must balance the body posture while simultaneously producing sufficient aerodynamic forces to stay aloft. In insects, control mechanisms correct flight direction and compensate the unintended body moments during perturbation, which include the changes in speed and timing of asymmetric wing angle of attack (Dudley and Ellington, 1990; Faruque and Sean Humbert, 2010b), the vigorous changes in segmental or bilateral asymmetry of wingbeat amplitude and frequency (Lehmann and Dickinson, 1997; Lehmann and Dickinson, 1998), and change in kinematic phase between fore and hindwing motion in four-winged insects (Alexander, 1986; Berger and Kutsch, 2003), which regulated by complex joints and high power thoracic musculature. A behavioural response of insect flight during wind gust has also been demonstrated in stalk-eyes flies (Vance et al., 2013).

Flying animals actively position their body appendages such as extension of legs [crickets (May and Hoy, 1990), gliding ants (Yanoviak et al., 2010), bees (Combes and Dudley, 2009), birds (Pennycuick, 1960; Pennycuick, 1968), fruit flies (Berthé and Lehmann, 2015)] and use the abdomen as a rudder (Berthé and Lehmann, 2015; Dickerson et al., 2014; Taylor et al., 2013; Zanker, 1988).

1-1-3. Biological receptors used for flight control in flies

Flies do not carry a radar, Global Positioning System (GPS), or pitot tubes and do not communicate with an Air Traffic Controller (ATC), but use their assembly of sensory receptors (See section 1-1-3). Flies have multiple highly specialized sensory channels that extract information from the environment for adaptive motor actions and memory formation (Taylor and Krapp, 2007). For flight control, halteres are used to measure Coriolis forces during body rotation (Bender and Dickinson, 2006; Fraenkel and Pringle, 1938; Pringle, 1948), antennae measure changes in airflow velocity (Fuller et al., 2014b; Sane et al., 2007; Yorozu et al., 2009), compound eyes detect light and help to regulate flight speed in the visual field (Preiss and Gewecke, 1991; Taylor et al., 2013), and ocelli monitor movement of the visual horizon (Fuller et al., 2014a; Simmons, 1982). This multimodal sensory architecture requires sensory processing by the central nervous system that serves as a coordinating centre of motor control activity similar to the brain of a human pilot (Fuse and Truman, 2002; Parry, 1947; Figure 1-1).

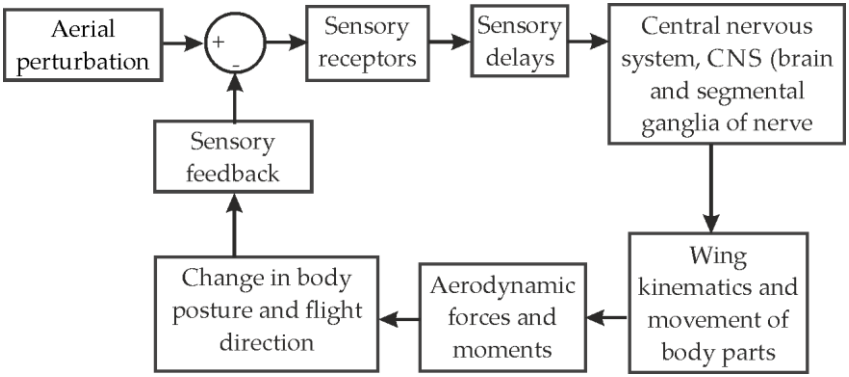

Figure 1-1: Schematic diagram of sensory feedback loop for flight.

Five senses allow insects to smell, see, taste, hear, and touch (Crespo et al., 2012).

Table 1-1: Categories of housefly's sensory inputs

	Category	Function	Receptors
1	Photoreceptor	detect light energy	compound eyes and ocelli[1]
2	Chemoreceptor	detect chemical substances including smell and taste	antennae[2]
3	Mechanoreceptor	encode mechanical energy including perception of air currents, surface and airborne vibrations and gravity	campaniform sensilla[3], antennae[4], wind-sensitive hairs[5] and halteres[6]

[1](Cornwell, 1955), [2](Marshall, 1935), [3](Dickinson, 1992), [4](Sane et al., 2007), [5](Weis-Fogh, 1949), [6](Sherman and Dickinson, 2003)

Receptors are transducers that encode energy into electrical signals transmitted to the brain or ventral nerve cord before appropriate responses can be stimulated (Suga and Katsuki, 1961). The working ranges of receptors are limited. Flies, for example, cannot see red light between 600-700 nm wavelength while dragonflies and some butterflies have additional colour receptors for this specific range (Briscoe and Chittka, 2001). While visual inputs are crucial to maintaining stability (Dyhr et al., 2013), delay in sensory feedback will cause operational failure and fast-growing unsteadiness (Aström and Murray, 2008). Visual delay ranges between 50 and 100ms (approximately 10-20 wing strokes) owing to the time required for photo-transduction and following visual motion computation (Rohrseitz and Fry, 2011). It has been reported that the shortest visual motor delay of houseflies is approximately 30ms (Wehrhahn et al., 1974).

Mechanosensory receptors such as wind-sensitive hairs deliver phasic feedback signals in each wing stroke cycle and instantaneously transmit the feedback (Bacon and Möhl, 1979). Furthermore, antennae-mediated feedback regulates wing motion at shorter delays of 20ms to control rapid changes in airspeed (Fuller et al., 2014b). In addition, halteres are directly connected with motor neurons of flight steering muscle (Fayyazuddin and Dickinson, 1996), require only 2.5-3ms latency for the activation of neck muscles during mechanical disturbances (Sandeman and Markl, 1980). Therefore, these proprioceptive mechanosensory receptors allow rapid reactions especially against close coupling of disturbances and responses (Ravi et al., 2013).
There are also possibilities that functional redundancy or across modalities among receptors might exist in flies (Christensen, 2004; Dudley, 2002; Fuller et al., 2014b; Taylor and Krapp, 2007). For example, halteres and visual input both encode body rotation known as "Visuo-mechanosensory fusion", which is likely

implemented by a high degree of aerial agility of flying insect (Christensen, 2004; Fuller et al., 2014b).

1-1-4. Muscle power generation and mechanical limits in flies

In insect flight, wing motion depends on several factors including the maximum power output, the mechanical constraints of the thoracic exoskeleton, the morphological limit of wing stroke and the temporal precision of neuromuscular activation (Chai and Dudley, 1995; Lehmann and Dickinson, 1997; Weis-Fogh and Alexander, 1977). Wing motion is driven by fibrillar flight muscle fibres located in the thoracic structure are exposed to specific capabilities and limitations (Ellington, 1985; Ellington, 1991).

The ability of flies to respond and modulate their wings' motions is due to a unique combination of wingbeat amplitude, frequency, and other flapping parameters, which are also constrained by morphological limits (Lehmann and Dickinson, 1998). During aerial perturbation, the adjustment of wingbeat amplitude and flapping frequency during modulations of flight force might cause monotonic change induced, profile and inertial power (Lehmann and Dickinson, 1997). Perturbation limits the duration of mobility, which might further impair flies' regular operational routine (Stuart, 1958). Orchid bees for instance eventually crash and cease flying completely when reaching flight speeds beyond $5.32 \pm 0.57 ms^{-1}$ due to a rise of turbulence strength including pressure drag (Combes and Dudley, 2009). In the broader context of ground locomotion, the walking fruit fly exhibits rapid arrest of locomotor activity known as Wind-Induced Suppression of Locomotion (WISL) in the presence of mechanical startle (Yorozu et al., 2009). Previous researcher also indicates this behaviour as adaptation period prior take-off, which occurred in the reaction of flies to the wind (Digby, 1958).

1-1-5. Manoeuvrability, flight performance and body stability

Flying insects may move along and rotate about three body axes i.e. yaw, pitch and roll (Casas and Simpson, 2008; Schilstra and Hateren, 1999). Body orientation with respect to a reference orientation is described by three angles in the Fick system, which rotated in fixed sequence starting with yaw and follows with pitch and roll (Haslwanter, 1995). The yaw, pitch and roll angles provide a complete description of all possible postures, and their temporal angular derivatives are the most important keys for flight stability and force production (Schilstra and Hateren, 1999).

Straight flight is insufficient to ensure aerial survival without control and instantaneous or sequential alteration of aerodynamic force output (Dudley, 2002). Thus, flight trajectories are dependent on the animal's locomotor capacity under perturbated flight condition (Hedrick et al., 2009). Agility is the ability to rotate around and translate along orthogonal body axes, while, manoeuvrability refers to the ability to control the movement or direction by complex manipulation of forces and moments (Dudley, 2002). Furthermore, stability is the ability to restore body orientation to its original value and is subjected to minor changes upset by gust or turbulence (Dudley, 2002; Voss, 1914). To date, several researchers have embarked on computational work (Gao et al., 2009; Gao et al., 2011; Sun et al., 2007; Zhang and Sun, 2010) as well as empirical assays (Combes and Dudley, 2009; Faruque and Sean Humbert, 2010a; Fuller et al., 2014b; Ravi et al., 2013; Vance et al., 2013) to explore posture stability in flying during aerodynamic perturbation.

There are ongoing debates whether insects are naturally unstable [hovering insect (Sun et al., 2007)] or naturally stable [general animal flight (Taylor and Thomas, 2002)] and even passively stable [hovering hawkmoth (Gao et al., 2009). Stability depends on animal's functional morphology, flight kinematics and also their operating conditions (Sponberg and Full, 2008). Passive aerodynamic characteristics provide partial compensation for unintended moments left by active mechanism induced by wings and other movable body appendages (Crall and Combes, 2013). Several studies highlighted the importance of passive damping to flight stability after perturbation that reduces neuromuscular and neurosensory requirements (Hedrick et al., 2009; Hesselberg and Lehmann, 2007). Aerodynamic perturbation induces instantaneous responses about roll axes, eventually followed by pitch and yaw axes [bees (Vance et al., 2013)]. High variation in roll angle occurs because no primary forces are actively generated in transversal body axis. Therefore, flies bank their body and manipulate the existing vertical lift vector in order to correct perturbation from lateral (Combes and Dudley, 2009; Ravi et al., 2013). Furthermore, rotational moment of inertia is the lowest around the roll axis followed by pitch and yaw axis (Dudley, 2002). Hawkmoth, by contrast, experienced greater fluctuation in yaw than in roll during feeding flight in vortex streets (Ortega-Jimenez et al., 2013).

1-1-6. Aerial turbulences

Turbulence is an unstable disorderly regime of flow in a highly irregular manner, which cannot be predicted simply by fluid dynamics theory. It is inevitable, fluctuating in terms of velocity and pressure, besides a complex or diversity in its fluid properties (Vogel, 1981; White, 2006). Turbulence eddies actively move

three-dimensionally and cause rapid diffusion of mass, momentum, and energy. This is not only due to variability in environmental airflows, but also vortex shedding during flapping flight [leading edge vortex (Ellington et al., 1996), wake capture during hovering (Dickinson et al., 1999), rotational circulation during stroke reversal (Dickinson et al., 1999), reduction of Wagner effect (Miller and Peskin, 2009) and peers-to-peers wake structure (Weimerskirch et al., 2001)]. Prior study has noted the importance of shedding vortices especially on dipole counter-rotating jet of tip vortices (Wang, 2000), which is modified immediately after flies experience aerial perturbation (Liu et al., 2012).

Turbulence disparity in the aerosphere has been related to daily routine and high levels of aerodynamic stability of flying creatures (Hanski et al., 2000; Kunz et al., 2008; McCay, 2003; Swartz et al., 2008). Within the atmospheric boundary layer that covers to a few hundred meters above the ground, the average wind speed, spatial scale, temporal scale and the wake region changes as level or turbulence intensities is altered (Combes and Dudley, 2009). Excluding extreme meteorological phenomena, average wind speed might vary from $0ms^{-1}$ to $10ms^{-1}$ including the rapid change of wind course (Stull, 1988). As turbulence wind speed surpasses typical insect flight speed, insect stability will gradually impair, thus requiring higher flight control demands. Previous studies have shown that insects respond to perturbation correlate with the strength of perturbation (Combes and Dudley, 2009) and its direction (Card and Dickinson, 2008b).

1-1-7. Reconstruction of flight behaviour

Measuring miniaturized insect behaviour in free-flight by videography is challenging because of fast flight speeds, small body size, rapid changes in body postures, and structural deformations especially wing [e.g. spanwise bending (Lehmann et al., 2011; Mountcastle and Daniel, 2009), wing torsion (Ennos, 1995; Wootton et al., 2003a) and cambering (Ennos, 1988)]. These problems can be solved by numerous techniques, which depend on experimental condition. The simplest approach consists of integrated mirrors and a single camera to capture multiple perspectives (Bomphrey et al., 2009; Tobalske et al., 2007; Zanker, 1990). More advanced approaches use two or more high-speed cameras to allow three-dimensional (3D) kinematic reconstruction as listed:

i. The *model-based approach* uses image measurement of silhouettes or optical flow, which matches with a model constructed separately (Moeslund et al., 2006). It provides better accuracy for images containing obstructions, clutters, poor contrast, low-lighting environment and can accurately estimate structural shapes.

ii. The *reconstruction-based approach*, on the other hand, does not require any preceding model (Hedrick, 2008; Hubel et al., 2010; Riskin et al., 2010; Shishkin et al., 2012). Body parts and wings are marked with dots, linked by connecting lines to describe motions. However, in this case, the accuracy of reconstruction depends on structural deformations of body and wings.

1-2. Research objectives and hypotheses

The motivation or the goal of this thesis is to obtain a complete description of body and wing motion in houseflies, responding to aerodynamic perturbations, by using automated 3D videography (*reconstruction-based approach*). The videos offer insights into the behavioural strategies of how flies control body motion and wing kinematics by altering aerodynamic forces.

In this thesis, I address several questions related to the performance of flies operating in changing flow condition:

1. How do flies cope with changing magnitude and direction of perturbation during flight?
2. How do wind gust and turbulence affect body motion and wing kinematics?
3. Does body orientation prior perturbation determine flight behaviour during perturbation?
4. Which sensory modalities encode aerodynamic perturbations (cf. Figure 1-2), thus keeping upright against instability?

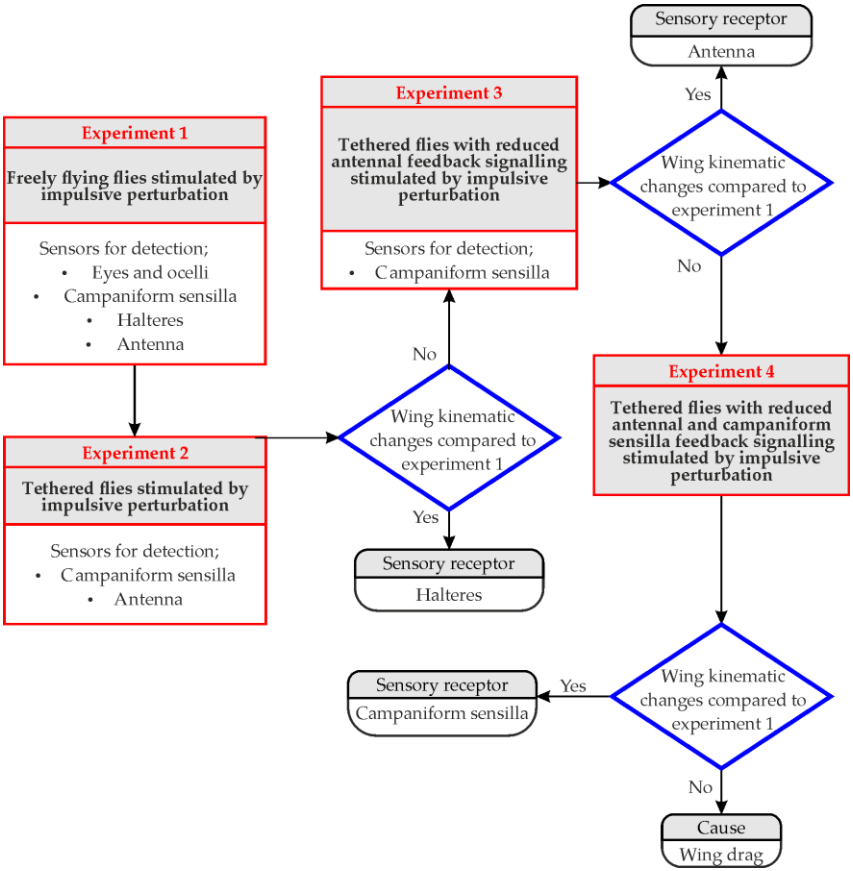

Figure 1-2: Overview of the experimental design and workflow used to determine the mechanosensor receptors of airflow sensation. Conceptual flowchart summarizes various treatments used to identify the effect of reduced sensory receptors during impulsive perturbations. Red boxes show the experimental details and sensory receptors for detection, blue rhombus indicates the decisions based on the change of wing kinematics and black rounded rectangles represent the terminal or end of experiment.

The research on how flies encounter aerial perturbation is worthy of study because changing flow condition or aerial perturbation may potentially;

1. change average air pressure at dorsal and ventral side of the wings;

2. modify flow and circulation around the flight envelope, including downwash, separation bubbles and wake geometry, which may lead to abrupt stall or operational failure;
3. alter existing and the newly created vortices, e.g. during stroke reversal; and
4. cause to the structural deformation of wing profile.

Thus, I tested the following hypotheses: (1) prior take-off, flies sense turbulence and entail a considerable degree of on-ground adaptation or exhibit suppression of ground locomotion under extreme windy condition, (2) flies immediately elicit passive body responses to gust, leaving the remaining task to active manoeuvring of movable body parts mainly wings, (3) flies have limited directional sensitivity and capability of body posture to response to impulsive perturbation (4) flies minimise the amounts of pressure drag by regulate projected area of the body and wing kinematics, and (5) flies require integrated multimodal of mechanosensory system, which predominantly mediated by fast reaction time receptors (e.g. antenna and halteres) to maintain stability.

It took approximately 2 years to develop the necessary experimental setups, 2 years of video digitisation and kinematic reconstruction, and another year for data and statistical analysis.

1-3. Thesis outline and organisation

This thesis consists of five chapters. Following this introduction, Chapter 2 offers a brief description of the experimental apparatus and methods used to record flight sequences, animal handling, airflow quantification, and documentation of relevant experimental procedures.

Chapter 3 presents experimental results including schematic diagrams, tables, and plots from the experiment of flies' responses to impulsive and continuous turbulent perturbation. The consequences of the lack of antennal feedback and the impairment of halteres functionality are also presented.

Chapter 4 give a complete interpretation and significance of the findings. Important discoveries are highlighted, and relevant issue are discussed. Brief data analysis including comparisons, modelling, and statistical analysis are also explained.

Chapter 5 concludes the study with an overall summary of the research findings, implications, limitations, and suggestions for future research.

2. Materials and methods

This chapter covers all methods and materials used in the thesis. It includes: (1) animals and breeding procedure, (2) how flies were tethered to a wire for tethered flight experiments, (3) the disabling of sensory feedback, (4) marking procedure by droplets of paint, (5) the experimental setups and videography, and (6) 3D-reconstruction of body and wings' motions.

2-1. Animals and pre-experimental procedures

2-1-1. Animals

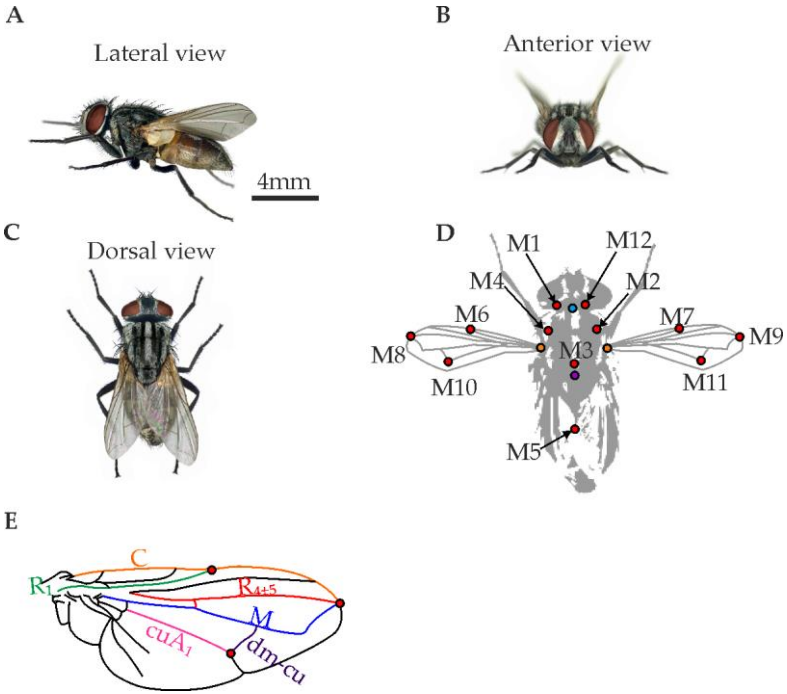

Figure 2-1: (A-C) Morphology of a housefly, *Musca domestica* (Hastings A. et al., 2004). (D) Fluorescent markers were placed on head, thorax, abdomen, and wings. Marker 1 and 12 were positioned between compound eyes and postocular satae, marker 2 and 4 marked on right and left presutural setae, marker 3 on dorsal thorax, in front of scutellum and marker 5 on dorsal abdomen at the centre of tegite 4. (C) Marker 6 and 7 were marked at the leading edge of the wings,

which connect end of vein C and vein R_1. Marker 8 and 9 were positioned on the left and right wingtips, which connect end of vein R_{4+5}, vein M, and vein C. Marker 10 and 11 were placed on the left and right wing, which connect end of vein dm-cu and vein CuA_1. The expanded virtual markers reconstructed from fly's morphology are the centre of gravity (purple dot), centre of head rotation (cyan dot) and the wing hinges (orange dots).

Data were collected from all-weather foragers, houseflies *Musca domestica* (Diptera, Muscidae) (Figure 2-1A-C). The flies arrived in 2009 from the Department of Animal Ecology and Tropical Biology, University of Würzburg, Germany and reared at the Department of Neurobiology, University of Ulm, Germany. Approximately 30-40 flies were kept inside a transparent glass aquarium (50cm × 30cm × 30cm) with sugar cubes and water as their daily nutrition. I kept the flies on a 16:8-hour light:dark cycle. In all experiments, I used 5-10 days old wild type female houseflies.

The animals' wet body mass, m_b was 18.39±2.02mg (mean±s.d, N=10) and wet translucent wing mass, m_w taken as 8.32±52.32μg (mean±s.d., N=20) both measured using a microgram balance (Model AT21 Comparator microgram balance, Mettler Toledo International Inc., Greifensee, Switzerland). Body length was 9.62±0.02mm (mean±s.d.) and wing length 6.98±0.03mm (mean±s.d.). The location of the wing's rotational axis is 2.55% wing length from the leading edge, the mean wing chord is 31% wing length, and total wing area is 14.7mm^2.

For the experiment, I pre-selected up to 4 flies using a light trap placed at the aquarium's ceiling. The cylindrical trap was made from opaque and acrylic vials, mounted with an attractive white light source in order to select active flies.

2-1-2. Breeding

The flies were bred at room temperature of approximately 22±2°C (mean±tolerance) and 45% humidity. After 10 days of hatching, adult flies were supplied with beer yeast dissolved in the water to promote reproduction. Over the next three days, female flies laid eggs on fresh beef liver placed inside a 5.5cm diameter petri dish. A wet tissue kept the liver moist for two days. I then transferred 30-40 eggs to a 20cm×9cm×9cm (length×width×height) plastic container that contained 500gram "bio-speisequark" (farmer cheese), two cups of bio-wheat bran (Firma Lucky Land Shop, Germany), and two cups of sawdust (Fressnapf Vertrieb Süd GmbH, Germany). The container was covered by a lid

equipped with a metal square-meshes window to release water vapour and supply fresh air. After two weeks, flies hatched and later died after 15-17 days.

2-1-3. Tethering procedure

Anesthetized flies were attached to a hollow stainless steel needle of 0.6mm diameter (Sterican, Braun Melsungen AG, Germany) by using ultraviolet-light-activated adhesive (Clear Glass, Henkel Loctite, Düsseldorf, Germany). Curing time was 20s by using a halogen lamp (150W, OSRAM GmbH, Garching, Germany). A needle was glued to head and notum so that head and thorax were fixed, and head motion could not be used for visual motion detection (Dickinson, 1999). To standardise the alignment of each fly during the experiment, I attached the needle to a metal holder, which was clamped to a micrometer positioner. The fly's body was inclined by 35° with respect the lab horizon, which is the typical hovering flight body posture (Ellington, 1984c). Flies recovered from anaesthesia after 3-4 minutes. I then placed the fly in the recording arena and waited for 2-5 minutes to allow the fly to exhibit a stable flapping cycle before starting the experiment.

The tethering protocol causes thoracic immobilisation and impairs the functionality of the flies' halteres to transduce fast information about body angle (Bender and Dickinson, 2006; Dickinson, 1999; Sane et al., 2007; Sherman and Dickinson, 2003).

2-1-4. Immobilisation of fly's antennae

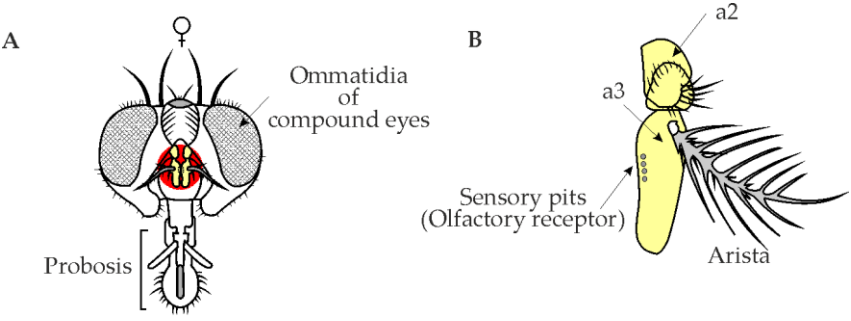

Figure 2-2: (A) Morphology of female housefly head capsule. Red indicates the area where adhesive was applied. (B) Morphology of the housefly antennae.

Antenna is a pair of sensory organs located in the anterior part of the head capsule. One of the three segments is the arista, a pouch-like structure (Figure

2-2B). The pedicel organ (Johnston's organ) is located at the antennae base, and campaniform sensillae are located between the second and third antennal segments.

To test the role of antennae in sensing wind changes, I glued all three segments of the left and right antennae including the arista (fourth antennal segment) and several sensory pits using a small droplet ultraviolet-activated adhesive (Figure 2-2A). Curing time was 20s using a halogen lamp (150Watt OSRAM GmbH, Garching, Germany). The responses of flies with manipulated antennae can only be characterised by tethering experiments because flies lose the response of the ventral cervical nerve motor neuron (VCNM) and thus unable to perform free-flight with restrained antennae (Haag et al., 2010).

2-1-5. Marking procedure

Flies were anesthetized for 4 minutes on ice flakes (2-4°C) before I marked them with 12 fluorescent dots (Pedeko, Monchengladbach, Germany) on their head (2 markers), thorax (3 markers), abdomen (1 marker), and left and right wing (6 markers). The marking procedure took approximately 5 minutes. Each kinematic marker had an average mass of 0.1μg to avoid wing deformation due to inertia. The average size of each dot was 0.25mm (3-5 video pixels) in diameter. The flies were taken to the take-off platform immediately after marking in which they were allowed to recover. The take-off platform was surrounded by water to prevent the fly from escape.

Single flies were placed on the take-off platform. To guide the animal during vertical take-off, I mounted three white LEDs (5mm diameter, Cree, NC, US) around the phototransistor housing (Figure 2-4A).

2-2. Experimental setups

The results in this thesis were derived from two experimental setups for free and tethered flight experiment (see Figure 2-6 for the number of tested flies). Both setups were equipped with an optical detection system (see Chapter 2-2-4). The setups generated two types of aerodynamic perturbations: (1) long lasting, continuous turbulent flow and (2) a horizontal, impulsive vortex jet. Throughout the thesis, the fully developed turbulence is termed "continuous perturbation" and the impulsive laminar vortex jet is termed "impulsive perturbation or wind gust". In both cases, I varied the average flow speed to highlight the dependency of wings and body kinematics on the strength of perturbation.

2-2-1. Experimental setup for application of turbulent perturbation

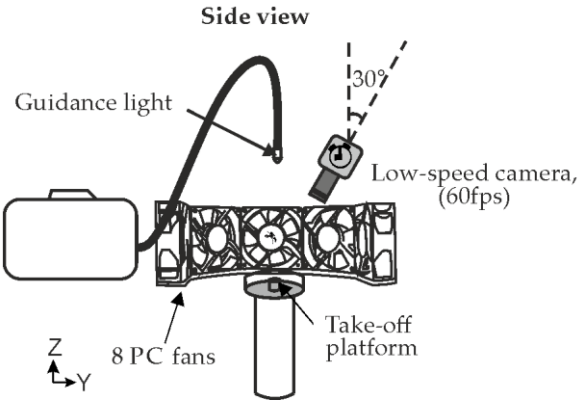

Figure 2-3: First experimental setup to record flight of freely flying flies behaviour during the application of continuous turbulence. White light provides visual guidance. See text for details.

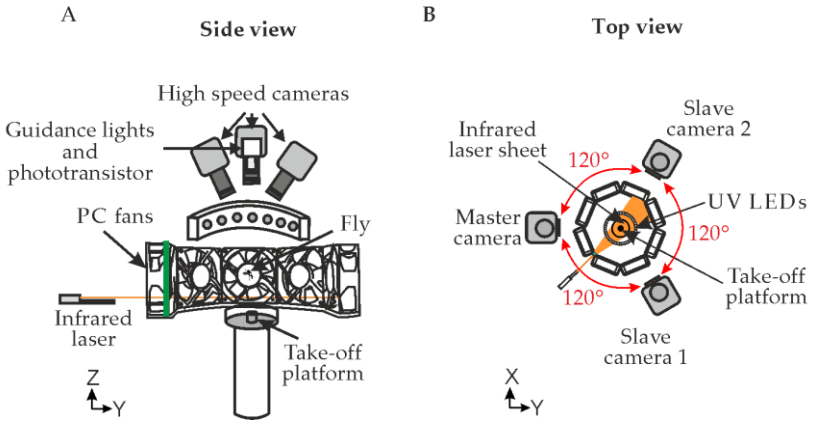

Figure 2-4: Experimental setup for generation of continuous turbulence produced by 8 rotating computer fans. (A) Arrangement of high-speed cameras and ultraviolet LED. The green bar indicates a cylinder lens between two fans that produced an infrared laser sheet for camera triggering. (B) Top view of the experimental video setup. Sampling frequency was 6000fps.

The first setup used to score: (1) the take-off delay of unrestrained flies during continuous turbulence using a single low-speed video camera (Figure 2-3) and (2) body and wings motion in freely flying animal using 3D-high-speed

videography and positional reconstruction of the painted markers (Figure 2-4, see Chapter 2-2-1 and Chapter 2-3).

For take-off delay measurements, I used a two-dimensional videography setup to "scan" the flies' activities on the take-off platform (Figure 2-3). I used a low-speed camera (model A602f, 60Hz, CMOS mount, 656pixel × 491 pixels, Basler AG, Ahrensburg, Germany) placed above the region of interest (ROI), pointed directly on the take-off platform position at the centre of the turbulence generator. The flies were stored inside a reservoir placed under the take-off platform, and they voluntarily walked through a tube.

The turbulence generator consists of eight computer fans glued together in an octagonal configuration (Figure 2-4). Each fan size was 8cm×8cm×2.5cm (height×width×thickness) (model KDE1208PTV1, DC12V/1.6W, Sunon Maglev, CA, US) and connected to a duty cycle controller, regulated by a waveform generator (Model WG8100, Tektronix, OR, USA). The region of interest at the centre of the arena was 6cm×6cm×6cm (height×width×thickness).

First, I recorded video images of flies continuously exposed to the different strength of turbulence (u_a of 0.37ms^{-1} - 1.4ms^{-1}) over 30 minutes, regardless the flies remained on the platform or take-off. The following experimental treatment is engaged with a brief investigation of body postures and wing kinematics subjected to narrower-ranging of turbulent strength (u_a of 0.47ms^{-1} - 0.77ms^{-1}) where the probability of flies performing take-off was considered high (cf. Figure 3-1, see Chapter 2-2-1).

Table 2-1: Description of experiment conditions on free-flight flies during turbulent perturbation

Flight condition	Treatment	Turbulent flow speed (ms^{-1})	Number of tested flies
Free-flight (Figure 2-4A-B)	Controls	0	17
	Turbulence environment	0.37ms^{-1} up to 1.4ms^{-1}	89
		0.37 ms^{-1} up to 0.73 ms^{-1}	44

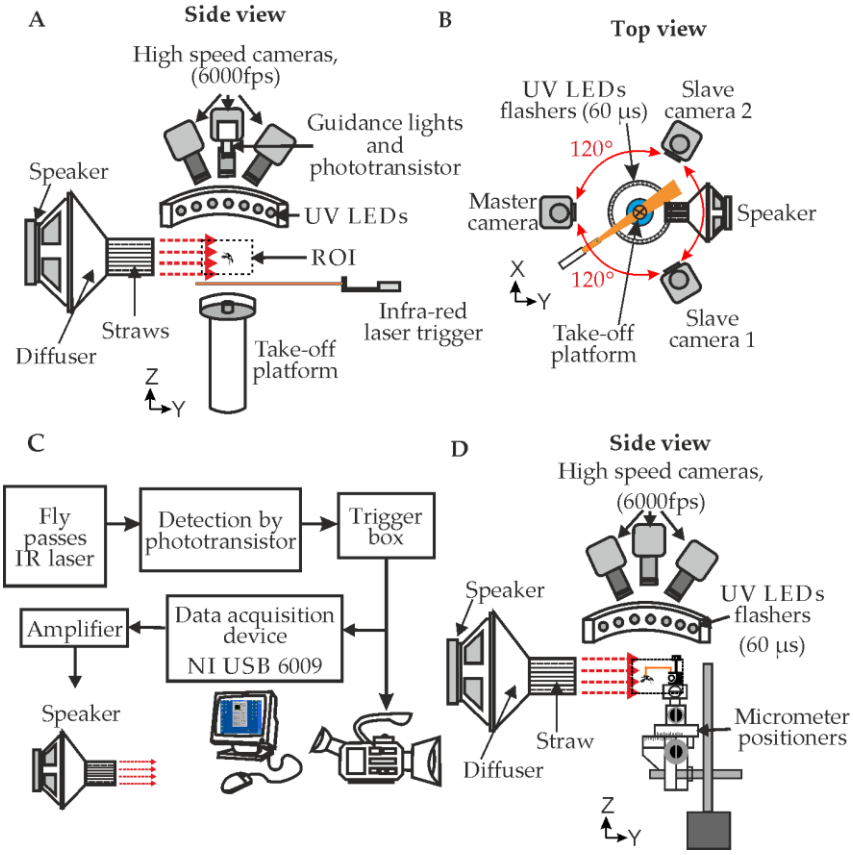

Figure 2-5: Second experimental setup for generation of a wind gust produced by a speaker. (A) High-speed cameras, gust generator and ultraviolet LED flashers on top of the high-speed cameras' ROI. (B) Top view of experimental setup. (C) Process of video recording. (D) Arrangement of high-speed cameras and ultraviolet LED flashers during tethering flight experiments.

2-2-2. Experimental setup for application of impulsive perturbation

The second automated 3D-videography configuration equipped with ultraviolet (UV) light illumination (see Chapter 2-2-3) produce a complete positional data of body and wing motion not only facing impulsive perturbation but also during narrower-ranging of airflow strength and tethered flight experiments. In

tethered flight experiments, however, I only reconstructed wing motion because flies' body was held stationary.

To record the fluorescent markers on body and wings, I constructed modified experimental setup similar to the previously described (Hedrick, 2008; Hubel et al., 2010; Riskin et al., 2010; Shishkin et al., 2012). This 3-D videography setup consists of three high-speed cameras (model Phantom v12, Vision Research Inc., Wayne, NJ, USA; Figure 2-5A-B, C). The cameras were calibrated from a calibration frame using Direct Linear Transformation (DLT) (Abdel-Aziz and Karara, 1971), and synchronized using master-slave configuration with a camera response time in the nanosecond range.

The high-speed cameras were mounted with an inter-camera angle of 120° above the arena that allowed me to track flies inside a volume of 6cm×5cm×5cm (length×width×height) representing the intersecting fields of view of the cameras (Figure 2-5A-B). All cameras were equipped with micro lenses (Nikkor, 60mm, f/2.8D, Nikon, Japan) that fitted with ultraviolet and light red filters (Jos. Schneider Optische Werke GmbH, Bad Kreuznach, Germany) to sieve out the light reflected by the fluorescent markers. Cameras were positioned 18cm above the centre of the ROI. As soon as master camera received a trigger, all cameras then captured images at 6000 frames per second at 1280x800-pixel resolution. At 170Hz average wingbeat frequency, this results in a temporal resolution of 35.3 video frames per wing stroke cycle.

I recorded video images of flies during impulsive perturbation of inner stream of vortex ring from the same direction. Despite stimulus came from the same direction, the azimuthal angle of the stimulus relative to the fly's longitudinal axis might vary. During perturbation onset, freely flying flies implied different body orientation (Figure 2-6). In some trial, extreme manoeuvres and wing-wing contact caused obstruction of markers on the wings, whereby, fewer flight sequences can be quantified for the responses of wing kinematics (Figure 2-6B).

The experiment on tethered flies consisted of two different treatments of flies with antennae and flies with immobilized antennae. Under this condition, flies would be subjected with anterior (0°) and posterior (180°) perturbation.

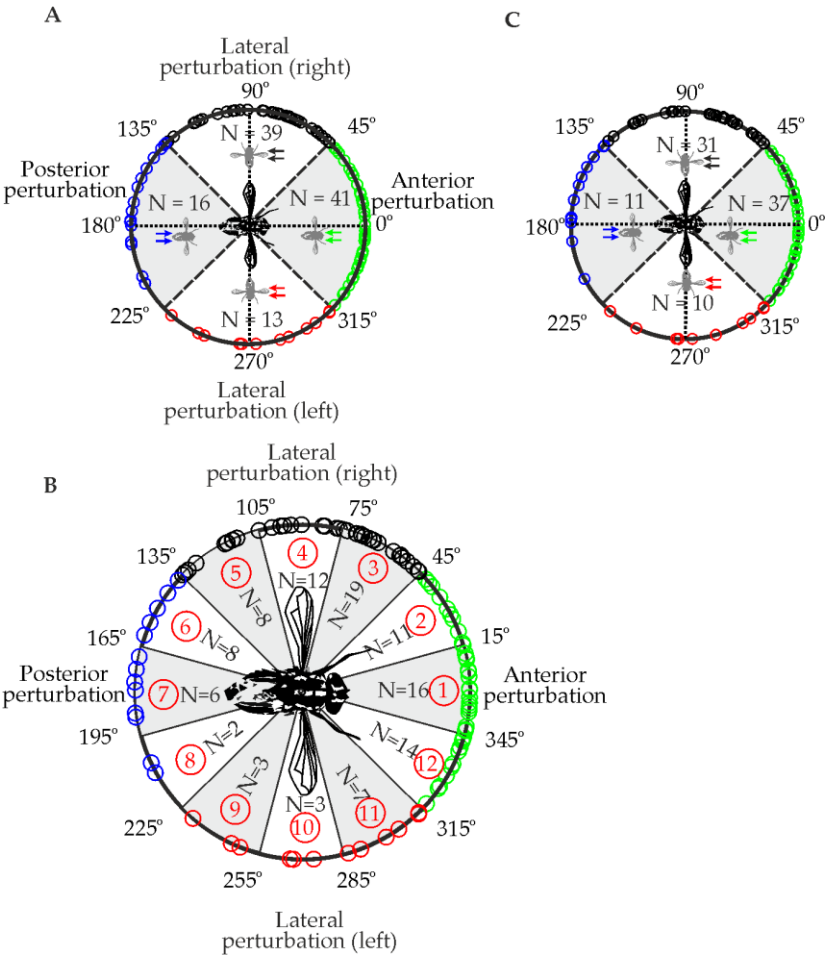

Figure 2-6: Number of tested flies. Direction of impulsive perturbation was determined at the time when the wind gust first reached the body at t=0ms (see Figure 2-5). Data were divided into (A) 4 subgroups for body motion analysis in Chapter 3-3, (B) 12 subgroups for directional sensitivity analysis in chapter 3-4 and (C) 4 subgroups for wing motion analysis in chapter 3-5. Arrows show flow direction at perturbation onset. Control (N=32 flies), perturbated flies for body motion analysis (N=109 flies) and perturbated flies for wings' motions analysis (N=89 flies).

Table 2-2: Description of experiment conditions on freely flight flies encountered impulsive aerial perturbation of wind gust.

Flight condition	Treatment	Direction of perturbation with respect to fly's longitudinal body axis				Number of tested flies	Total number of tested flies
Free-flight	Controls	-				32	32
	Impulsive perturbation by wind gust (see Figure 2-5A-B)	Anterior perturbation	**Body analysis**	Subgroup 12	315°-345°	14	41
				Subgroup 1	345°-15°	16	
				Subgroup 2	15°-45°	11	
			Wing analysis	-		37	37
		Lateral perturbation (right)	**Body analysis**	Subgroup 3	45°-75°	19	39
				Subgroup 4	75°-105°	12	
				Subgroup 5	105°-135°	8	
			Wing analysis	-		31	31
		Lateral perturbation (left)	**Body analysis**	Subgroup 6	225°-255°	3	13
				Subgroup 7	255°-285°	3	
				Subgroup 8	285°-315°	7	
			Wing analysis	-		10	10
		Posterior perturbation	**Body analysis**	Subgroup 9	135°-165°	8	16
				Subgroup 10	165°-195°	6	
				Subgroup 11	195°-225°	2	
			Wing analysis	-		11	11

Table 2-3: Description of experiments on tethered flies

Flight condition	Treatment	Direction of perturbation with respect to fly's longitudinal body axis	Flow speed of impulsive perturbation (ms^{-1})	Number of tested flies	Total number of tested flies
Tethered flies (see Figure 2-5D)	Intact	Anterior (0°)	1.2	15	43
			1.1	13	
			1.0	7	
			0.9	8	
		Posterior (180°)	-	-	27
	Immobilized antennae (see Figure 2-2A)	Anterior (0°)	-	-	17
		Posterior (180°)	-	-	19

2-2-3. Ultraviolet light flasher

To minimise motion blur of fluorescent markers on the captured images, a ring of 40 ultraviolet light emitting diodes, UV LEDs (3mm diameter, 405nm wavelength, 40mWsr^{-1} radiant intensity, 20° viewing angle, Bivar, CA, US) were flashed with 60μs light pulses and synchronized with high-speed cameras (Figure 2-5A-B). The UV LEDs were glued around a black-coated aluminium ring by using heat resistant epoxy. This configuration distributed ultraviolet light to all directions which is beneficial to record the fly's extreme body angle during manoeuvres. Mean brightness of ROI due to the ultraviolet and guidance lights were approximately 9±5%Lux (mean±s.d.). Although ultraviolet light illumination caused degradation in performance during flight, flies were still capable to actively control the visual task given (Shishkin et al., 2012). For data analysis during impulsive perturbation, I only used video images recorded up to 30ms after perturbation onset before any visual responses and that degradation of flight was likely to be engaged (Fuller et al., 2014b).

2-2-4. Optical detection system

To capture images when the fly is in the cameras' ROI, I assembled an optical detection system to automatically trigger the cameras (Shishkin et al., 2012) (Figure 2-5A-B). I constructed a light path employing a horizontally oriented 2mm thickness infrared laser sheet (model QL8516SA, 850nm wavelength, 60° opening angle, 30mW, 5.6mm diameter, driven by EU-37 SMD laser diode driver, Roithner Lasertechnik GmbH, Vienna, Austria). A phototransistor above the arena (model L-53P3C, Kingbright, Taiwan, stored inside a cylindrical custom-made Poly Vinyl Chloride (PVC) housing) detected changes in laser light when the fly crossed the sheet. A Charge-Coupled Device (CCD) zoom lens (model TF15DA-8, 1/3 Inch CCD 15mm, f/2.2 fixed focal length manual Iris C-mount, Fujinon, Tokyo, Japan) fitted with an infrared filter (830nm infrared filter, model R-72, Heliopan Lichtfilter-Technik Summer GmbH & Co KG, Munich, Germany) was attached in front of the phototransistor's housing. Whenever a fly crossed the laser sheet, the phototransistor, which connected to a custom-made switching circuit, transmitted a 5V transistor-transistor logic, TTL signal to a data acquisition system (14-Bits, 48 kS/s, NI USB 6009, National Instruments, TX, USA). The TTL signal was then further transmitted to both computer (Acer EXTENSA E264 E5200, 3.20GHz Inter® Core™) and the master camera.

The fly's photoreceptors could not detect the infrared laser sheet because the visual sensitivity of the photoreceptors ranges from 380 to 600nm with a maximum sensitivity at 340-350nm (Goldsmith and Fernandez, 1968; Stark and Johnson, 1980).

2-3. 3D-reconstruction of marker positions

The quality of all conceivable approaches for automated tracking of insect free-flight critically depends on the measured positional accuracy of wings and markers. The reconstruction of the fly body is less challenging because markers move at relatively low-speed during flight. By contrast, painted markers on the wings move fast and may often disappear on the video images. During clap and fling, markers at the wingtip and trailing edge even fuse during wing-wing contact (Miller and Peskin, 2005), making the automated tracking procedure more demanding.

2-3-1. Calibration and image tracking software

For marker tracking and digitizing, I used a software algorithm MATLAB™ v7 (The MathWorks, Natick, MA, USA) DLTdv3 developed by Tyson Hendrik (Hedrick, 2008).

The focal volume within flies flew was calibrated using "milimeter graph paper" that was visible on all cameras. I digitized 25 positions in eight different layers of 5mm equidistant steps in height, resulting in a total of 200 positions inside the ROI. The first layer of calibration was positioned at the lower base of the ROI. A calibration target (4.5cm×4.5cm graph paper glued on a 1mm thickness glass plate) was mounted horizontally and displaced to specific locations, positioned manually by a micromanipulator positioner. I repeated the calibration procedures several times before and after the experiments to ensure high accuracy of three-dimensional reconstructions.

The digitization software DLTdv3 automatically scored the position of each marker according to the marker's centre of area (Hedrick, 2008). The software has features such as zooming, auto tracking mode, real-time viewing of different cameras at the same window at high accuracy with 95% confidence intervals. The auto-tracking reduces digitization time of a large quantity of videos. The auto-tracker attempts to anticipate the location of specific markers on successive video frames by fitting an equation to previously digitized markers and extrapolating the position. During automated digitization, I used a linear Kalman filter as a fitting equation to predict the location of the subsequent frame. If predicted markers position matched to a specific auto track threshold, the auto tracker proceeded to examine the next frame. The software uses images from at least two cameras and the appropriate DLT coefficients to reconstruct the three-dimensional fly's body and wings' motions.

The tracking algorithm processed one image in 0.15s on a 3.20GHz Inter® Core™ computer.

2-3-2. Image post processing

To enhance image quality and remove noise, I used the software VirtualDub v1.9.9 (Lee, 2009); Figure 2-7). The image processing tool stretched the brightness level according to image histogram ([0.00-0.023]>2.01>[0.00-1.00] (Y)), increased the contrast (400%), and applied box blur (radius 2, power 2). These procedures improved the automated position tracking and kept the adjusted search window at the centre of markers.

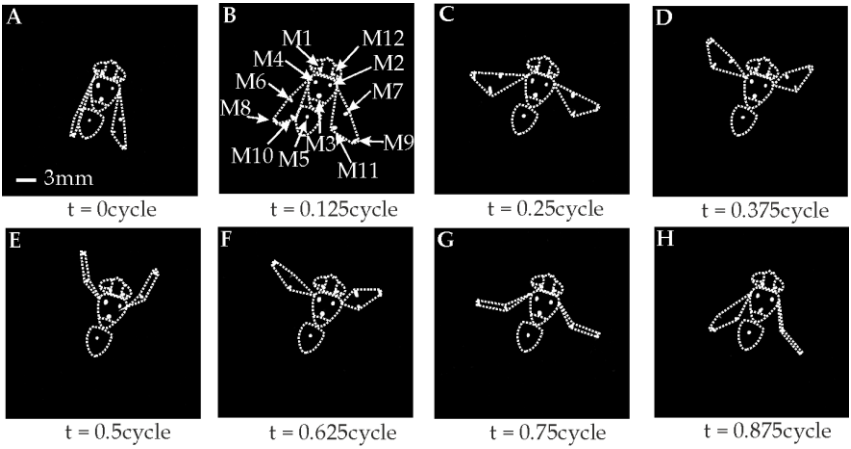

Figure 2-7: Series of raw images recorded from a single high-speed camera (master camera). Images show an individual fly during voluntary take-off at (A) 0% stroke cycle, (B) 12.5%, (C) 25%, (D) 37.5%, (E) 50%, (F) 62.5%, (G) 75% and (H) 87.5% stroke cycle (Stroke period 6ms, cf. the dashed lines at Figure 2-13E, F, G). Dotted lines approximate fly body and wings.

2-3-3. Quantifying tracking performance and accuracy

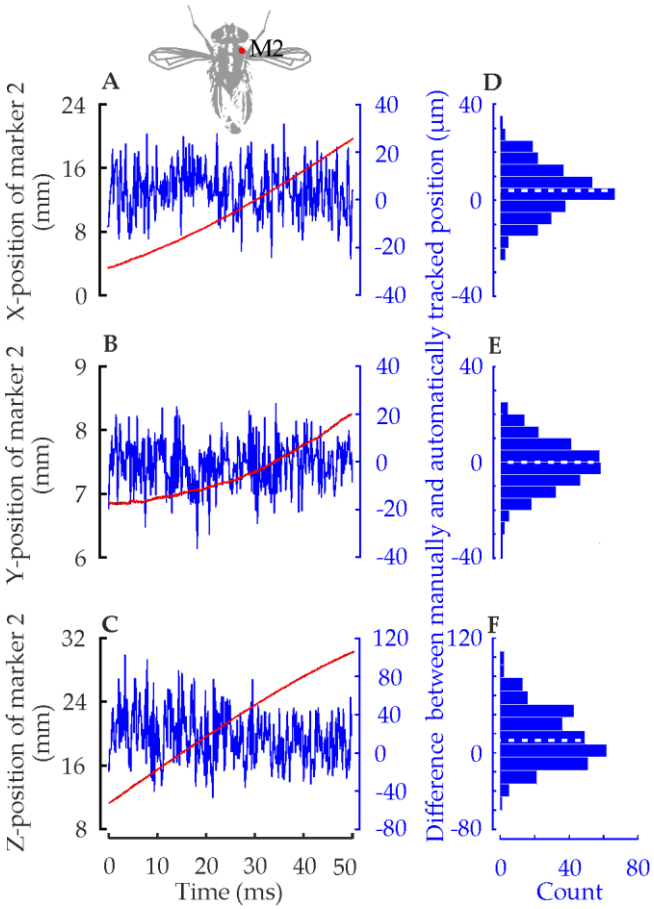

Figure 2-8: Comparison between automatic and manual tracking precision of fluorescent markers. Time traces of marker 2 on the fly thorax, at X-axis (A), Y-axis (B) and Z-axis (C). Red line represents positional data of automatic tracker using a Kalman-filter, while the black dashed lines are positions of manually tracked data (left scale). Blue line represents the difference between automatic and manual position tracking (right scale). (D-F) Histogram of residuals and medians (dotted white lines).

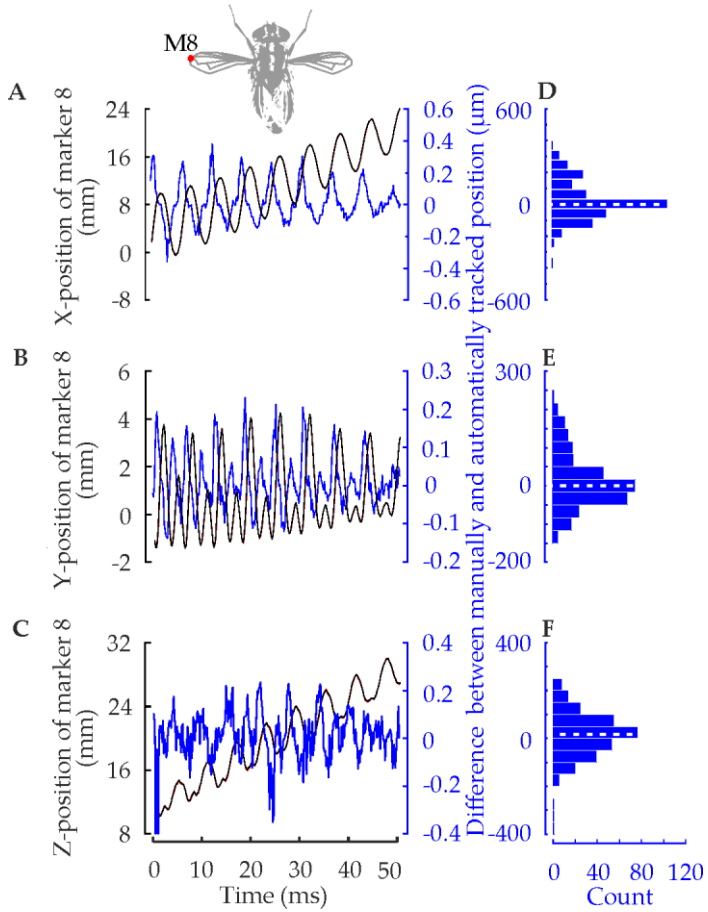

Figure 2-9: Comparison between automatic and manual tracking precision of fluorescent markers. Time traces of marker 8 on the fly wing, on X-axis (A), Y-axis (B) and Z-axis (C). Red line represents positional data of automatic tracker using Kalman-filter while the black dashed lines are positions of manually tracked data (left scale). Blue line represents the difference between automatic and manual position tracking (right scale). (D-F) Histogram of residuals and medians (dotted white lines).

To investigate position tracking performance and accuracy, I compared manual digitization with automated tracking procedures of marker 2 positioned on fly's

thorax (Figure 2-8A) and marker 8 positioned on fly's left wingtip (Figure 2-9A) for 300 frames of a flight sequence. Digitization error affects both the accuracy and reliability of position measurements (Haggard and Wing, 1990; Scholz, 1989; Scholz and Millford, 1993). I assessed the changes in accuracy between the coordinates extracted by each method using histograms of residuals (Fry et al., 2003; Liu and Sun, 2008; Ristroph et al., 2009).

The positional differences of marker 2 between automated and manual tracking ($X/Y/Z_{\text{human digitization}}$-$X/Y/Z_{\text{automated tracking}}$) are plotted in Figure 2-8A-F including histograms of residuals. The differences present in mean±s.d. are: 4.16±10.35μm (median = 4μm, X-axis), -1.13±10.23μm (median = -0.59μm, Y-axis), 16±28.19μm (median = 13.15μm, Z-axis). The differences are the smallest in the x-y plane because both axes are in the same plane of focus. By contrast, Z-axis yields higher differences because it orthogonally points to the cameras, which may lead to inaccuracies of calibration coefficients due to the limited depth of focus. These inaccuracies in position measurements caused by calibration error occur both in automated and human tracking. However, predictive tracking algorithm provided in automated tracking software improves tracking accuracy.

Positional differences of marker 8 between both tracking approaches are shown in Figure 2-9A-F. The mean±s.d. differences are: 16.46±116.98μm (median =0.73μm, at X-axis), -11.42±70.01μm (median =-0.4μm, at Y-axis) and 13±99.19μm (median =17.07μm, at Z-axis), respectively. The differences increase at mid-stroke of the wing flapping cycle because wing translates at maximum speed. Moreover, elevated wing translational velocities cause motion blur, which turns round markers into an oval and stretched markers. In this case, crosshairs provided by the software to assist in locating the moving markers of interest often failed. In both approaches, angular errors of wing motion caused by the measured positional differences were less than ~0.14°, which is acceptable. In addition, there may be additional errors in the method used due to structural deformation, ancestral inaccuracy and inaccuracy in morphological measurement. Hence, the similarity of results obtained by automated tracking software and manual tracking program confirmed that both methods are capturing the wing and body motion within an acceptable level of accuracy.

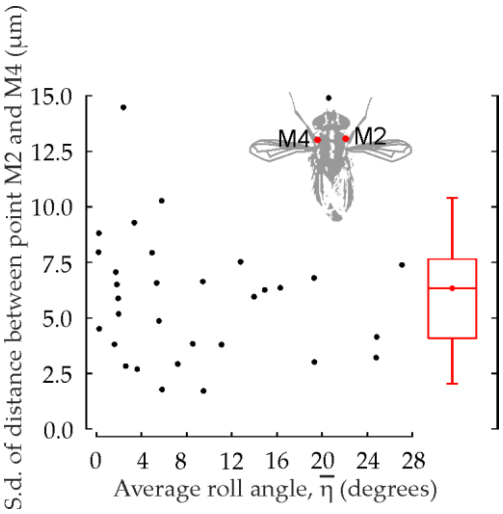

Figure 2-10: Assessment of tracking imprecision owing to steep inclination of body angle (e.g. extreme thorax roll). Data represent the standard deviation of ground distance between marker 2 and 4 on the thorax of 32 flies with different average roll angle within a flight sequence. Boxplot represents mean, median and distribution of standard deviation of all measured flight sequences.

To further assess the significance of positional errors on a high degree of body orientation and postures (e.g. extreme body roll), I estimated distance between markers 2 and 4 on the thorax of 32 flies with different average roll angle (Figure 2-10). Measurement errors owing to excessive roll occur because cameras that are orthogonally mounted with respect to ROI capture round fluorescence markers as oval blobs. The associated imprecision are displayed concisely as the standard deviation of measured distance of a flight sequence. In all examined body orientations, there is no apparent relationship between the standard deviation of the measured distance when body roll increases (Pearson's coefficient, r=-0.02). Mean standard deviation of the distances for 32 flight sequences is 6.09±3.15μm (mean±s.d.), which is relatively small, even at a high inclination of the thoracic structure. Tracking precision can be enhanced by slightly tilting and mounting the cameras with 120° inter-camera angle as shown in Figure 2-4 and Figure 2-5.

2-3-4. Data processing

The three-dimensional positions of the painted markers were estimated in each trajectory in a global coordinate system. However, obstruction of fluorescent markers on the wings by the body and wing-wing contact caused contiguous gaps of missing data points. To recover the missing data points, I separately interpolated raw data of markers positions (X, Y, and Z) by cubic-spline functions to each coordinate value. MATLAB fit function, `interp1` was used for a 10-fold upsampling (linear interpolation) procedure of the position data. The consecutive procedure helped to smooth wing rotational velocity especially during the stroke reversals. The current study found that filtering the wing position data using low pass filters produced artifacts in the data set. By contrast, I removed digitization noises from body positional data using MATLAB's zero-phase one-dimensional digital filter. It was applied separately for each X/Y/Z coordinate as unweighted running average with a temporal window size of 10% mean wingbeat period for wings and one mean wingbeat period for the body.

2-3-5. Three-dimensional reconstruction of wing motion

The MATLAB algorithms for kinematic reconstructions were adopted from existing scripts (Schützner, 2016; Shishkin et al., 2012) with several amendments on fly size, morphology and assumptions.

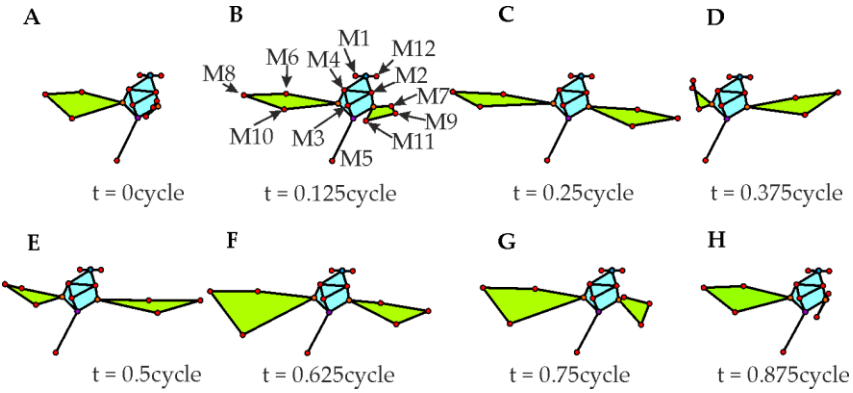

Figure 2-11: Three-dimensional reconstruction of wings and body motion during (A) 0%, (B) 12.5%, (C) 25%, (D) 37.5%, (E) 50%, (F) 62.5%, (G) 75% and (H) 87.5% stroke cycle (Stroke period 6ms, cf. the dashed lines at Figure 2-13E, F, G). Red dots indicate the location of fluorescent markers M1-M12. Virtual markers are shown for the centre of

head rotation (cyan dot), and wing hinges (orange dots). The virtual markers were derived from the fly's body shape.

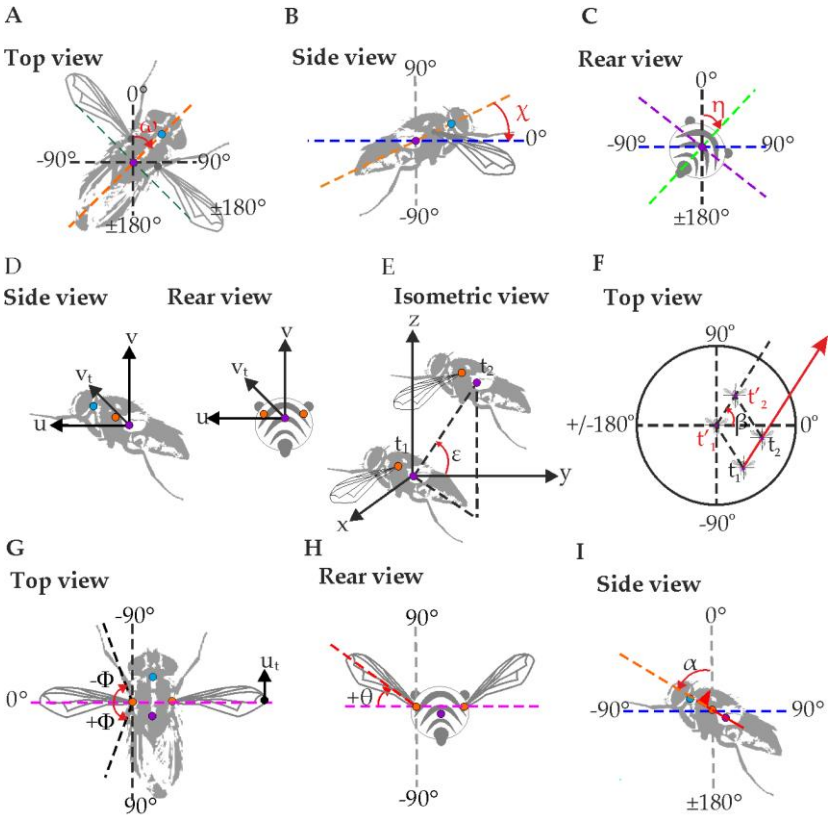

Figure 2-12: Angles and vectors. (A) Yaw angle of the body, ω; (B) pitch angle of the body, χ; (C) roll angle of the body, η; (D) translational velocity of the body, v_b, which depends on vertical translational velocity, $v_{b,v}$, and horizontal translational velocity, $v_{b,h}$. (E) Body inclination reconstructed from two consecutive video images, ε. (F) Flight direction reconstructed from two consecutive video images, β. (G) Stroke angle, Φ and wingtip velocity, $v_{w,t}$. (H) Wing elevation angle, θ. (I) Wing angle of attack, α. Centre of gravity (purple), centre of head rotation (cyan) and wing hinges (orange) were derived from the fly's morphology. Thorax transversal axis (purple dashed line), thorax longitudinal axis (orange dashed

lines), thorax vertical axis (green dashed line), wing transversal axis (magenta dashed line), wing longitudinal axis (red dashed line), lab vertical (grey dashed line) and lab horizon (blue dashed line).

I expanded the set of measured markers by a set of virtual body markers that were reconstructed from the housefly's morphology. I approximated the position of wing hinges, the centre of gravity, and centre of head rotation with respect to markers measured on the thorax (Figure 2-11A-H) from anatomical drawings (Chapman and Goulson, 2000). The distances between these virtual points were expressed in relative units, and absolute values scaled according to the size of each fly. The longitudinal body axis (anteroposterior axis) connects the centre of head rotation (near cervix) with the centre of gravity. The transversal body axis (also known as lateral axis) passes through the thorax and connects both wing hinges (Figure 2-12A-C). The two axes define the thorax horizontal plane. The thorax vertical axis (dorsoventral axis) point is normal to the thorax horizontal plane. The wing's longitudinal axis for wing rotation was reconstructed using a method similar to that described previously (Lehmann et al., 2011).

The coordinate transformation from global coordinates to body-centred coordinate systems followed Haslwanter approach (Haslwanter, 1995). Global coordinate systems are typically used to evaluate flight trajectories whereas body-centred coordinate systems are used to score kinematic parameters of the animal (Wang et al., 2003). Position in the body-centred coordinate system calculated from global coordinates by subtracting the position of fly's centre of gravity in each time step from the positions of all markers in that time step.

From this coordinate transformation, I further calculated other flight parameters such as body yaw ω (body rotation about dorsoventral axis), pitch χ (body rotation about transversal axis), and roll η (body rotation about longitudinal axis) angle including its temporal derivatives (Figure 2-12A-C). The wing kinematic parameters are wingbeat frequency n, wing stroke angle Φ (which is defined by the angle between wing rotational axis and transversal body axis), wing elevation angle θ (which is defined by the angle between wing rotational axis and wing stroke plane), and wing angle of attack α (which is defined by angle between the wing chord and the vertical axis (in global coordinate system). See Figure 2-13 for a time trace of exemplary flight sequence.

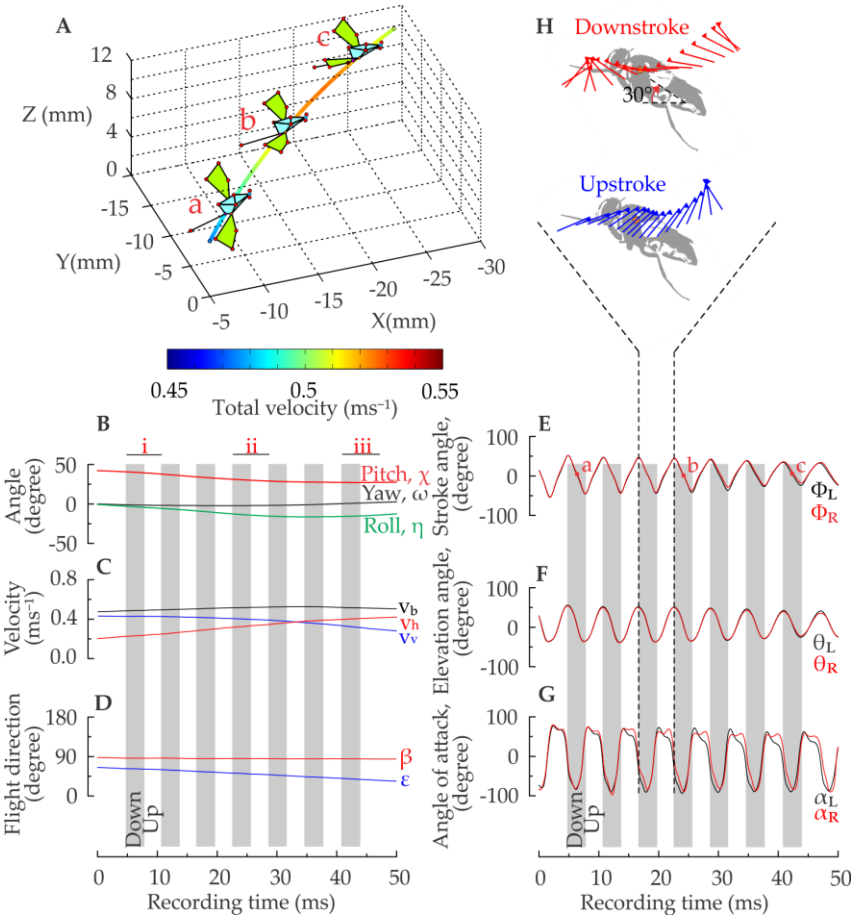

Figure 2-13: Time trace of a 50ms flight sequence. (A) Three-dimensional flight trajectory of a housefly at 6.38ms (a), 24.14ms (b), and 42.12ms (c) after take-off. Velocities of centre of mass are plotted in pseudo-colour. (B) Body rotational angles (yaw, pitch, and roll). (C) Body vertical translational velocity, v_v (blue), body horizontal translational velocity, v_h (red) and total body translational velocity, v_b (black) throughout the flight sequence. (D) Body inclination, ε (blue) and flight direction, β (red); (E) wing stroke angle, Φ; (F) wing elevation angle, θ; (G) wing angle of attack, α; (H) wing motion during downstroke (red) and upstroke (blue). In this example, wingbeat amplitude was 89°, angle of attack at mid-stroke -84° during pronation and 59° during supination and

wingbeat frequency 167Hz. Triangles indicate leading edges of the wing, and the body was pitched by 30° with respect to horizontal. Grey area indicates wing downstroke.

2-4. Validation of flows

2-4-1. Flow structure of the turbulent flow during continuous perturbation

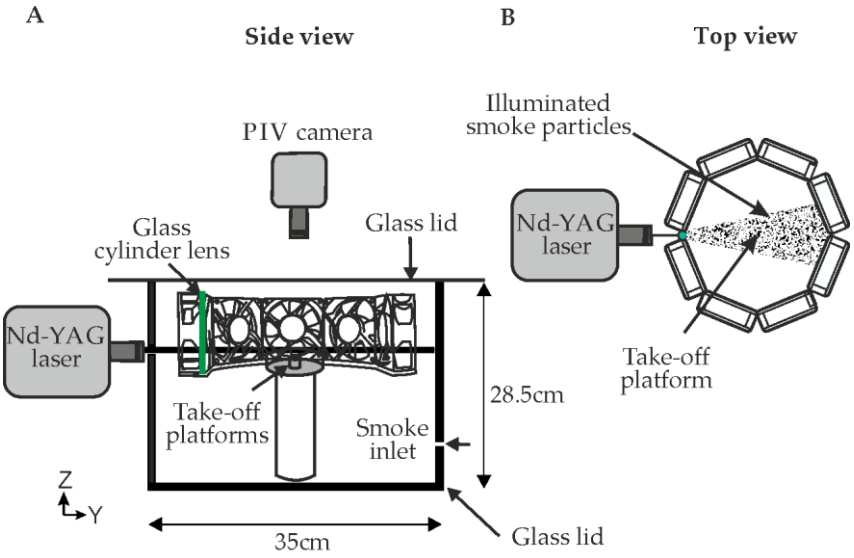

Figure 2-14: Experimental setup to quantify turbulence airflow using Digital Particle Image Velocimetry (DPIV). (A) A Nd-YAG laser (Solo III laser generator, Insight v5.1, TSI, Shoreview, MN, USA) illuminated smoke particles, recorded by a PIV camera (PowerView 2M high-definition, model 630057, TSI, MN, USA) above a black painted wooden box. (B) Top view of experimental setup. See Figure 2-4 for more detail explanation.

To visualize the characteristics of the turbulent flow produced by the eight fans (Figure 2-3 and Figure 2-4), I conducted 2-D Digital Particle Image Velocimetry (DPIV) in the absence of flies (Figure 2-14). For seeding, I used smoke inside a wooden black painted container sized 35.5cm×35.5cm×28.5cm (height×length×width). The container was then covered by a transparent glass lid sized 50cm×50cm×2mm (height×width×thickness). The size of smoke

particles was approximately 90μm diameter and ignited by smoke matches (Splintax, Raketenmobellbau Klima GmbH, Emersacker, Germany). I used a 50mJ per pulse dual mini-Nd:YAG laser (Solo III laser generator, Insight v5.1, TSI, Shoreview, MN, USA) to create two identical light sheets separated in time by 250ms (Δt). A 3mm diameter glass cylinder positioned between two fans converted the laser beams into a 5mm thickness of the horizontal light sheet.

Paired images of a 155-cm^2 flow field were captured using a camera (PowerView 2M high-definition, model 630057, TSI, MN, USA) at a frame rate of 14.5Hz. Each camera was equipped with a lens (AF Nikkor, 50mm, f/1.4D lens, Nikon, Japan) and oriented orthogonally to the laser sheet. To determine the directions and magnitude of particle displacements, the frames were cross-correlated by a Fast Fourier Transform (FFT) correlator with a final interrogation area of 32pixel×32pixel.

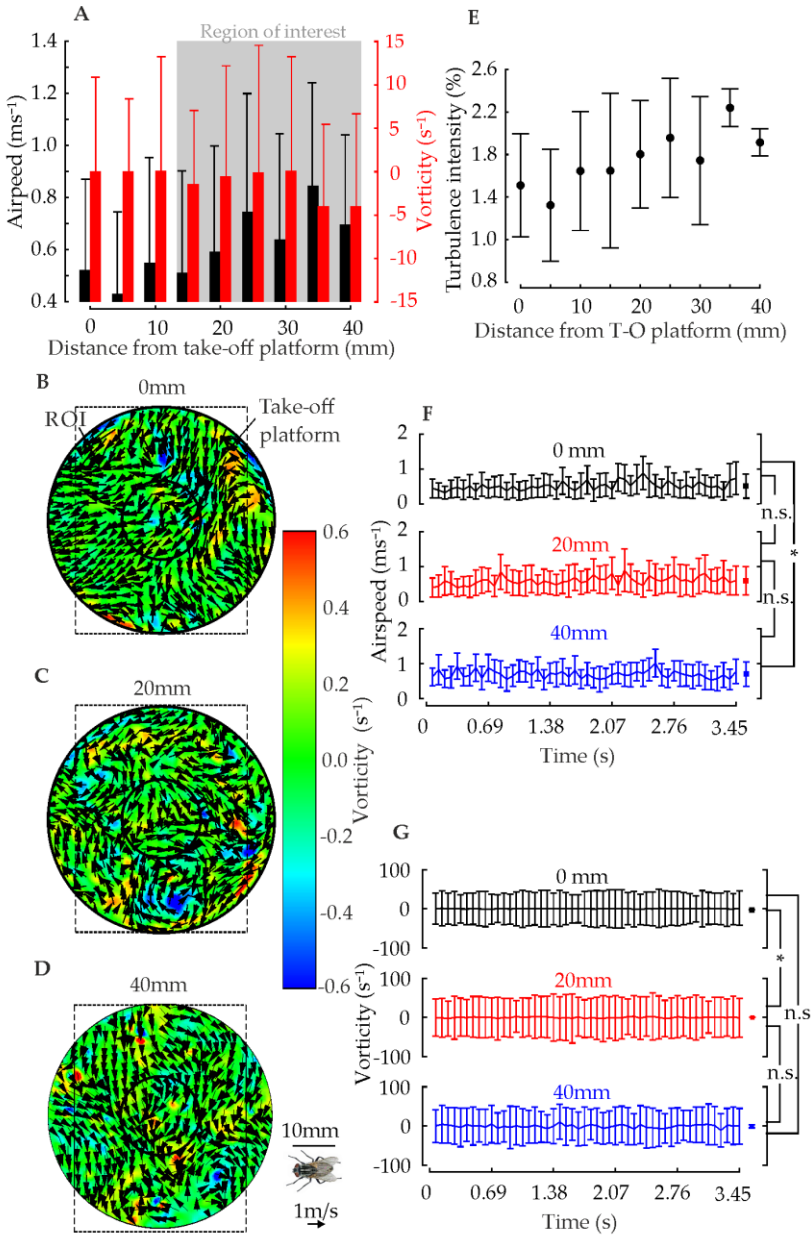
A
Region of interest
Airpeed (ms⁻¹)
Vorticity (s⁻¹)
Distance from take-off platform (mm)
E
Turbulence intensity (%)
Distance from T-O platform (mm)
B
0mm
ROI
Take-off platform
C
20mm
D
40mm
Vorticity (s⁻¹)
10mm
1m/s
F
0 mm
20mm
40mm
Airspeed (ms⁻¹)
n.s.
*
Time (s)
G
0 mm
20mm
40mm
Vorticity (s⁻¹)
n.s.
*
Time (s)

Figure 2-15: Flow characteristics of turbulent flow above take-off platform at 37% duty cycle of voltage supply to the fans (see Figure 2-14). (A) Airspeed (black) and vorticity (red) at various heights above the platform. Grey box indicates the high-speed cameras' region of interest (cf. Figure 2-4). (B-D) Snapshot of mean air velocity and mean vorticity at 0mm, 20mm and 40mm above the platform. Dashed lines indicate region of interest. The fly is shown for size comparison (Hastings A. et al., 2004). (F-G) Time traces of mean airflow velocity in *F* and mean vorticity in *G* at 0 (black), 20 (red), and 40mm (blue) above the take-off platform. ROI, Region of interest. N = 50 measurements.

I recorded 50 paired-images using Insight 3G™ v10.3.0 (TSI Inc., St Paul, MN, USA) at 0, 5, 10, 15, 20, 25, 30, 35 and 40mm above the platform (Figure 2-15). The take-off platform was exposed to turbulent flow produced by fans which rotated at 37% of duty cycle determining the fan speed. The flow was quantified in a region of interest sized 55mm diameter (area, $38\times10^{-3}m^2$), which is equal to the camera field of view. Missing vectors were filled by interpolation of local means derived from 3×3 grid of nearest neighbouring matrix. Finally, the vectors were smoothed by a 3×3 grid and a low-pass filter. From the flow field, I derived local speed, turbulence intensity (total standard deviation of velocity vectors at the vector node location) and vorticity (local rotational motion of airflow) using Tecplot 360 v2013R1 (Bellevue, WA, USA). However, the limited recording speed did not allow me to estimate the change in flow within the fly stroke cycle (5.88ms at 170Hertz of average flapping frequency). The setup is also not able to measure airflows along the Z-axis, towards or away from the camera (refer Figure 2-14A). The average characteristics of airflow cannot thus be aligned in time with the fly's kinematics, owing to the generic randomness of turbulence.

I averaged the data for all 23440 vectors of each flow field. The result shows that airspeed significantly increases with the increasing of vertical distance from the platform (ANOVA, linear regression, $y=7.84\times10^{-3}x+457\times10^{-3}$, r=0.83, p<0.05, N=9 data points, Figure 2-15A). Meanwhile, turbulence intensity linearly increases with the increasing height of measurement plane (linear regression, $y=0.016x+1.43$, r=0.83, p<0.05, N=9 data points, Figure 2-15E). By contrast, flow vorticity was independent of the vertical distance of the take-off platform. (ANOVA, $F_{8,441}=6.39$, p<0.05, Figure 2-15A, right y-axis).

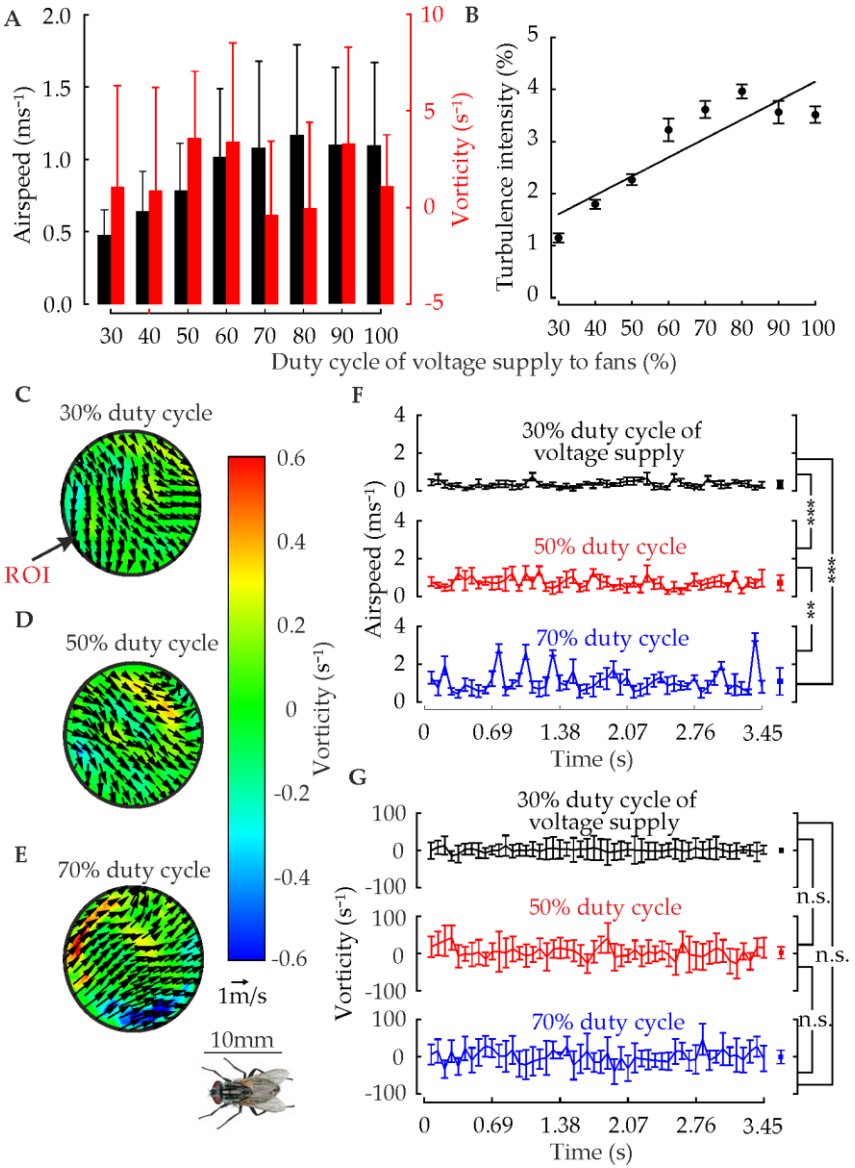

Figure 2-16: Change of flow characteristics with fan speed at 5mm above the take-off platform (cf. Figure 2-14). (A) Mean airspeed (black), mean vorticity (red); (B) mean turbulence intensity. (C-E) Airflow velocity vectors and average vorticity contours at different duty cycles of voltage supply to the fans. The fly is shown for size

comparison (Hastings A. et al., 2004). (F-G) Time traces of mean airflow velocity in *F* and mean vorticity in *G* at 30 (black), 50 (red) and 70% (blue) duty cycle of voltage supply. Isolated error bars indicate mean and standard deviation of uncertainty. Asterisks represent significant difference (*=p<0.05, **=p<0.01, ***=p<0.001) between treatments. N = 50 measurements.

I then recorded images and further analysed airflow characteristics on the take-off platform (5mm above ROI) under five different strength of turbulence (Duty cycle 30, 40, 50, 60 and 70%). Duty cycle is a proportion between the time when voltage supply is active and total period. The fluctuating airflow field characteristics on the take-off platform changes with the increasing fan speed. Means for all 6197 vectors of flow field show that the increase of fans speed led to an increase in airspeed (ANOVA, $F_{7,49747}$=1176.8, p<0.001, linear regression fit, y=0.01x+0.17, r=0.90, p<0.01, N=8; Figure 2-16A, G) and turbulence intensity (Kruskal-Wallis test, Chi-square value =386.43, p<0.001, linear regression fit, y=36.36×10^{-3}x+514.65×10^{-3}, r=0.88, p<0.01, N=8; Figure 2-16B). Superficially, the fluctuations in airspeed increase with increasing duty cycle of voltage supply ($u_{a,DC=30}$=0.36ms^{-1}±0.22ms^{-1}, $u_{a,DC=50}$=0.74±0.40ms^{-1}, $u_{a,DC=70}$=1.09±0.72ms^{-1}; Figure 2-16F) but the relationship of fan speed and vorticity remains unclear (ANOVA of airspeed, $F_{7,400}$=0.4535, p>0.05; Figure 2-16A). Vorticity fluctuates around zero value (Figure 2-16G) and the presence of vortex structures (Figure 2-16E) indicates the high intensity of turbulence airflow filled in the ROI.

2-4-2. Generation of wind gust during impulsive perturbation

In the second experimental setup that used to test flies during impulsive aerodynamic perturbation (Figure 2-5A-B), I produced a single vortex ring by loudspeaker (model W130S, 11cm diameter diaphragm, Visaton, Haan, Germany). The control panel programmed in LabVIEW™ software (National Instruments, Austin, TX, USA) is able to control amplitude, offset, rising time, active time, and falling time of the voltage supply to the amplifier (model KRF-V4550D, 80W, Kenwood). The voltage supply was set to a rising time of 5ms, active time of 100ms, falling time of 1s (sawtooth waveform). Then, the diaphragm pushed the air through a diffuser with an outlet (40mm × 40mm) that consisted of straws with a 3cm diameter. The diffuser straightened the flow, reduced large scales of turbulence and minimized lateral velocity components caused by swirling motion of air, thus produced a uniform effective airflow that perturbated the flies inside the camera's ROI. Besides, there were 23±4.5ms (mean±s.d.) of computer processing delay that needed to consider during data analysis.

2-4-3. Flow quantification by a thermistor

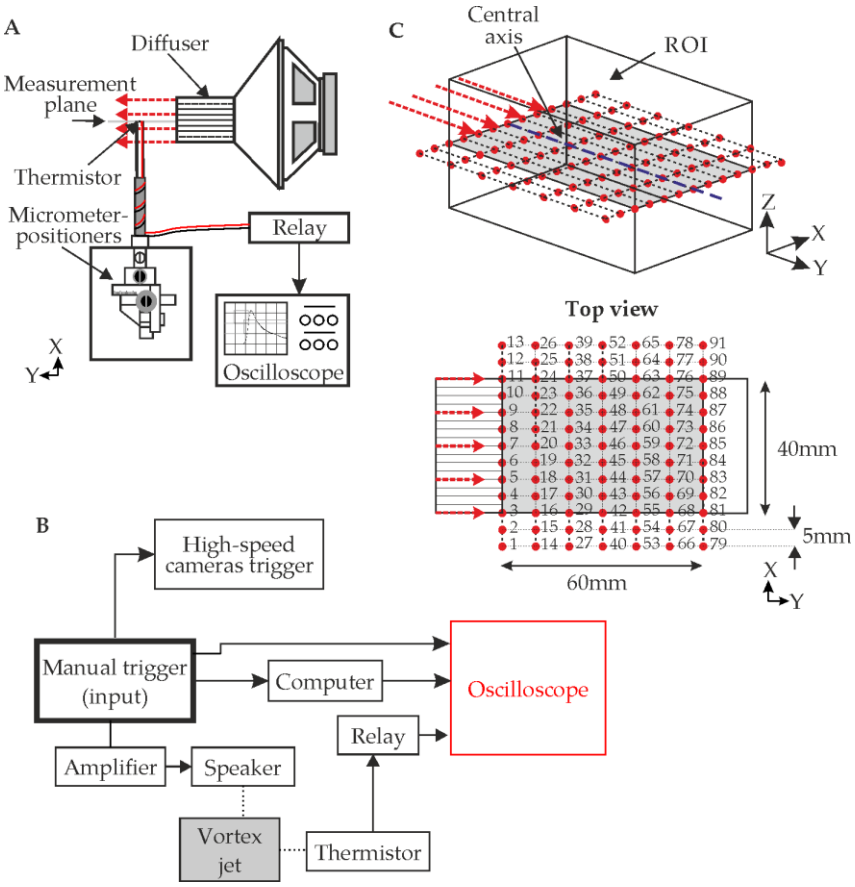

Figure 2-17: Quantification of flow during impulsive speaker-induced perturbation using a thermistor (cf. Figure 2-5). (A) A micrometer manipulator was used to move the thermistor on the measurement plane. (B) Flowchart represents the process for quantification of flow. (C) Thermistors measurement point (red dots; 63 points inside region of interest and 28 points outside region of interest). Red arrows indicate flow direction and grey area is the measurement plane.

To quantify flow generated by the speaker, I used a tiny heated-bead thermistor (model 111-202CAK-H01, 0.36mm diameter, 0.5s time constant in air, 25 kHz sampling rate, Honeywell, NJ, US) whose electrical resistance depends on temperature, thus on fluid velocity (Figure 2-17A). Though this high sampling frequency measurement allowed realignment of kinematic data with the flow speed but it was insensitive to flow direction and, thus, unable to provide a complete characteristic of the flow rather than speed.

The data were recorded by a 4-channel digital oscilloscope (Model TDS3034B 300 MHz Tektronix Inc., OR, USA) synchronized by the trigger from the high-speed cameras (Figure 2-17B). I measured 130 positions in a horizontal measurement plane, which positioned at the centre of cameras' ROI (20mm vertical distance from ROI base, Figure 2-17C). The flow measurement also includes the wake structures 1cm outside ROI. By assuming a symmetrical flow structure, the measured data were then revolved around the central axis of ROI to obtain complete information of airjet speed for the entire volume. The original coarse mesh of measurement volume was 10mm×5mm, but I bilinearly interpolated to finer meshes of 1mm×1mm. Time, velocity and position of the measured airflow structure were placed into an interactive multi-dimensional matrix database and later used during analysis of body and wing kinematic data.

To convert the thermistor voltage to airspeed (ms^{-1}), I used a commercial thermal anemometer (Model TA5, Airflow Lufttechnik GmbH, Rheinbach, Germany). The probe of commercial anemometer and thermistor bead were placed in a row close to each other in front of 2cm diameter outlet of laminar wind tunnel and tested with 7 different random speeds of $0.5ms^{-1}$ intervals. This procedure yielded a relationship between airspeed, u_a and measured voltage, V, which is expressed as the exponential calibration curve, $u_a = 60.52e^{-\left(\frac{V-11.82}{4.03}\right)^2} + 0.61e^{-\left(\frac{V-3}{1.86}\right)^2}$ (Goodness of fit: SSE=880.4×10^{-6}, R^2=0.99, RMSE=0.03).

The ROI is not a closed volume, thereby, might be contaminated by flow from outside the experimental setup. I thus quantified the ambient airspeed at the centre of non-perturbated ROI for 100s. Ambient airspeed was $0.07\pm0.01ms^{-1}$ (mean±s.d.), which is 17-times smaller than the generated wind gust and considered to be negligibly small.

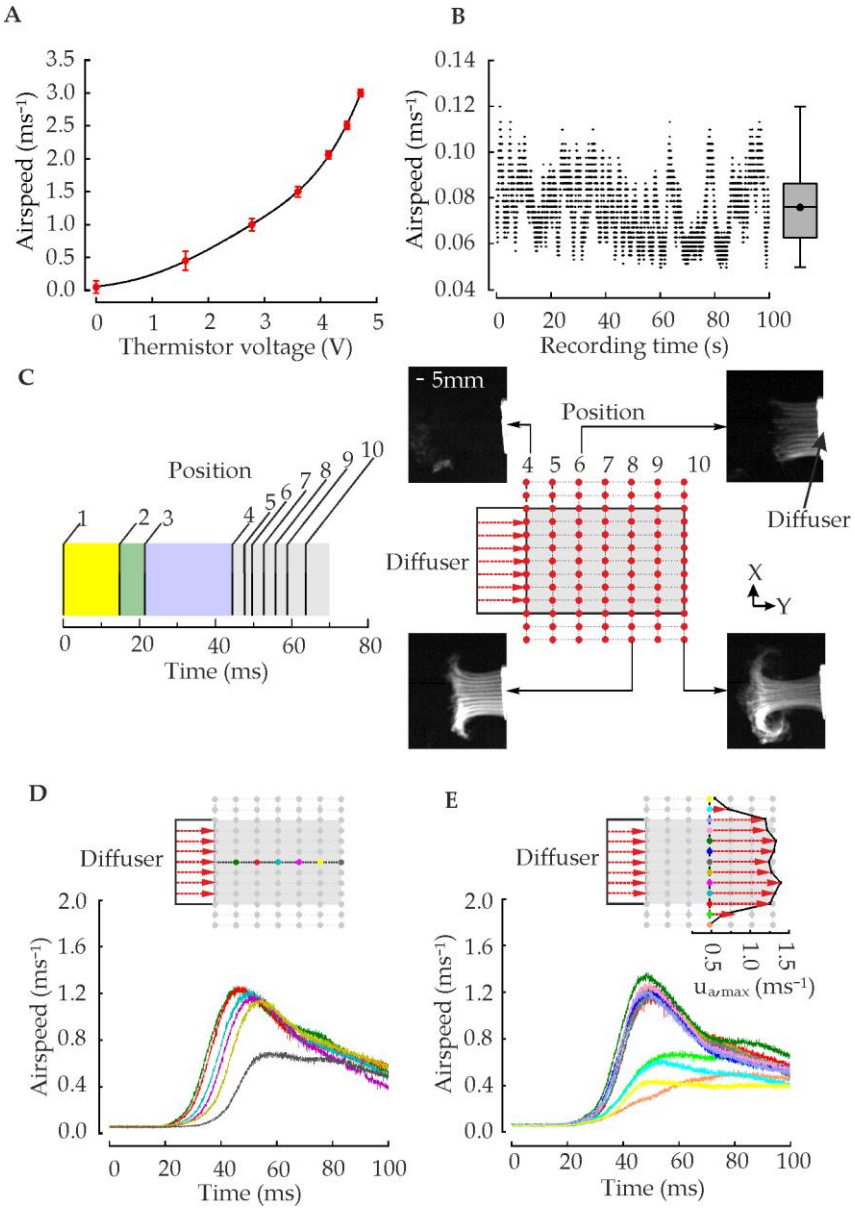

Figure 2-18: Airflow measurements and quantification during impulsive perturbation (cf. Figure 2-5). (A) Thermistor calibration curve obtained from seven airspeeds averaged over 20s (N=10, 000) in

front of a 2cm diameter outlet of a laminar wind tunnel (cf. chapter 2-4-3). (B) Temporal fluctuations of airspeed inside camera ROI and in still air. Boxplot represents mean, median and distribution of standard deviation. (C) Timeline during recording: (1) trigger started, (2) speaker diaphragm is pulled, (3) diaphragm pushes, (4) airflow reaches diffuser outlet, (5) velocity peak of airflow travels to positions 5, 6, 7, 8, 9 and 10 including the respective smoke trails. (D) Airspeed along the central axis and (E) across the centre of ROI including its speed profile. Please refer to Figure 2-17 for more details.

Table 2-4: Onset of flow stimulus (vortex ring, Figure 2-18C)

	Event	Time (ms±s.d.)
1	Trigger system activated (position 1)	0.00±0.00
2	Speaker diaphragm was pulled backward (position 2)	14.45±2.11
3	Speaker diaphragm was pushed forward (position 3)	20.96±2.44
4	Airflow reached position 4	43.67±2.58
5	Airflow reached position 5	46.72±1.51
6	Airflow reached position 6	48.69±0.26
7	Airflow reached position 7	51.70±0.66
8	Airflow reached position 8	54.70±0.54
9	Airflow reached position 9	57.79±0.85
10	Airflow reached position 10	62.53±2.31

The smoke trail showed that the inner stream of vortex ring remains laminar and formed uniform flow of wind gust within the ROI (Figure 2-18C). Peak airspeed of fully developed gust occurred when the wind gust was ejected out of diffuser, and gradually decreased with the increasing distance from the diffuser (ANOVA of maximum speed, $F=45.86$, linear regression fits, $y=-30.30\times10^{-3}x+1.31$, $N=5$, $r=-0.97$, $p<0.01$) where y is the distance from the diffuser outlet (Figure 2-18D). The smoke trail also confirmed uniform airspeed profile across the ROI ($1.28\pm0.06 ms^{-1}$ (mean±s.d.), see Figure 2-18E). The airspeed outside the ROI was $0.60\pm0.11 ms^{-1}$ (mean±s.d.) because the boundary layer separated and rolled up to form a vortex ring at the edge of diffuser outlet (Figure 2-18C).

2-4-4. Statistics

For all statistical tests, I used MATLAB R2013a (The MathWorks, Natick, MA, USA) and Origin v9 (OriginLab Corporation, MA, USA). I considered a p-value of 0.05 to indicate that two populations have significantly different means. If not stated otherwise, data are given as means±standard deviation (mean±s.d.). P-values were indicated by asterisks with 'n.s.' for not significant (Table 2-5).

Table 2-5: Statistical symbols

Symbol	Meaning
n.s.	Not significant
*	$p \leq 0.05$
**	$p \leq 0.01$
***	$p \leq 0.001$

To test variances for repeated measurement of flow speed and vorticity at different vertical distances from platform or fan speed, I used parametric statistics multi-way ANOVA (Zar, 2010). Logistic regression analyses were used to quantify the relationship between flow speed and flight behaviour.

To study the relationship between predictor (independent variable) and the response (dependent variable), I implemented regression analysis in MATLAB's curve fitting tool using the non-linear Least-Squares Difference method LSD (Sachs, 1978). Furthermore, the significance of linear and non-linear regressions was tested using the Pearson's correlation coefficient, r and coefficient of determination, R^2. I compared two or more regression lines to each other using analysis of covariance (ANCOVA) and p-value highlighting the differences in slopes.

To test the changes in animal behavioural during turbulent perturbation compared to controls, I first calculated the means and standards deviation of data pooled from 0ms to 10ms after take-off. In contrast to impulsive perturbation, I calculated the means and standards deviation of data pooled from -60ms (before perturbation onset) to 60ms (after perturbation onset). I then compared the differences between time traces of homogeneous datasets of body and wing kinematics at different directions of stimulus with controls using t-test.

To investigate the relationship between the circular distribution of mean body angular velocity during perturbation (linear dependent variables, e.g. yaw, pitch and roll) and stimulus directions (circular independent variables, 30° bins of stimulus direction, 12 categories, cf. Figure 2-6A). I later performed a circular-linear correlation to compare these measured datasets of mean body

angular velocity with non-perturbated controls (Batchelet, 1981; Fisher, 1993; Zar, 2010). This parametric circular statistical procedure was employed to correlate angular and linear variables (lies between zero and 1) (Mardia, 1976).

3. Results

3-1. Take-off behaviour during continuous perturbation of turbulence

As soon as the tested flies left the reservoir underneath the take-off platform (Figure 2-3), they immediately experienced turbulent airflows (Duty cycle of the voltage supply to the fans, DT=30%-100%, mean airspeed, u_a=0.47-1.2ms^{-1}, average turbulence intensity, I=0.6%-1.87%, N=89 flies).

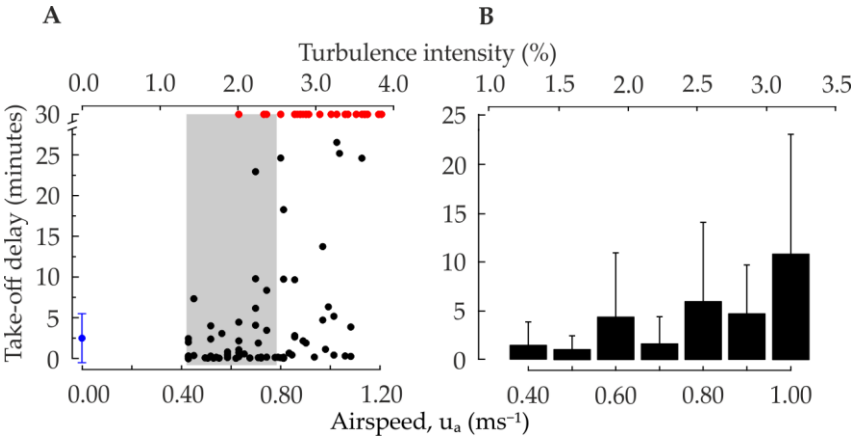

Figure 3-1: (A) Time before take-off from the platform plotted as a function of turbulence strengths of continuous perturbation (black dots, N=89 flies). Flies that refused to take-off within less than 30 minutes are shown in red (N=23 flies). Flies that take-off inside in a non-turbulence environment are shown in blue (controls, N=17 flies). Grey area indicates the characteristics of airflow used in the experimental setup for further analysis of body and wing kinematic alteration during perturbation (N=44 flies). (B) Take-off delay and standard deviation plotted as a function of turbulence strengths (Linear regression fit, y=13.21x-4, R^2=0.69, p=0.02, N=66 flies).

Figure 3-1 shows that non-perturbated flies initiated flight immediately as they entered the platform. In contrast to turbulent perturbation, after 30 minutes exposed to turbulent flow, 23.6% of the tested flies are still refused to initiate take-off, probably due to the relatively high strength of turbulence (red dots, Figure 3-1A). This effect first occurred at a transient airspeed of 0.63ms^{-1} (turbulence intensity of ~2%). Take-off latency significantly increased with

increasing turbulence airspeed (linear regression fit, y=13.21x-4, r=0.83, ANOVA: F=10, p=0.02, N=66 flies, Figure 3-1B). I observed that as the growth of turbulence strength and intensity increased, flies crouched or gripped on the platform for longer periods and limits their on-ground locomotion.

3-2. Arial drift during take-off

Under turbulent condition (u_a= 0.47 - 0.77ms^{-1}, grey region in Figure 3-1A), 40ms after take-off, flies' body positions (X, Y, Z) were -4.9±8.3mm, 5.27±12.3mm, 15.3±7.1mm (N=44 flies, Figure 3-2B, D, F). Though, this body scattering of perturbated flies was not significantly different to non-perturbated controls (-6.42±10.3mm, -1.04±9.1mm and 13.39±5.2mm; t-test, p>0.05; N=17 flies, Figure 3-2A, C, E). During turbulent, the tested flies were scattered in a broader volume directly above the take-off platform (Figure 3-2G). Variance of mean body position (in standard deviation, $\sigma_X \times \sigma_Y \times \sigma_Z$) in all axes significantly increased over time (linear regression fit, y=16.34x+12.6, r=0.99, ANOVA: F=138.2, p<0.001, N=6 data points) with 2.2-fold higher rate of increase compared to controls (linear regression fit, y=7.49x+33.25, r=0.85, ANOVA: F=10.5, p=0.03, N=6 data points). When flies arrived at the centre of the cameras' ROI (after 40ms), the volume of the positional variance of continuously perturbated flies was 723mm^3, which is 1.5-fold larger than in non-perturbated controls (484.5 mm^3).

Positional variance in impulsively perturbated flies also significantly increased over time (linear regression fit, y=19.3x+575, r=0.89, ANOVA: F=12, p=0.04, N=5 data points; Figure 3-3E) with 1.6-fold lower rate of increase compared to non-perturbated controls (linear regression fit, y=30.8x+670.2, r=0.98, ANOVA: F=97.3, p=0.002, N=5 data points). The smaller volume of positional variance after take-off is presumably characterised by predominant vertical flight direction. Therefore, during perturbation onset (t=0ms), flies' body positions (X, Y, Z) were 1.1±8.9mm, -0.5±9.3mm and 14.6±6.6mm (N=109 flies), which is not significantly different compared to controls (2.5±10.3mm, 1.49±9.4mm and 15.74±6.9mm; t-test, all instantaneous p>0.05).

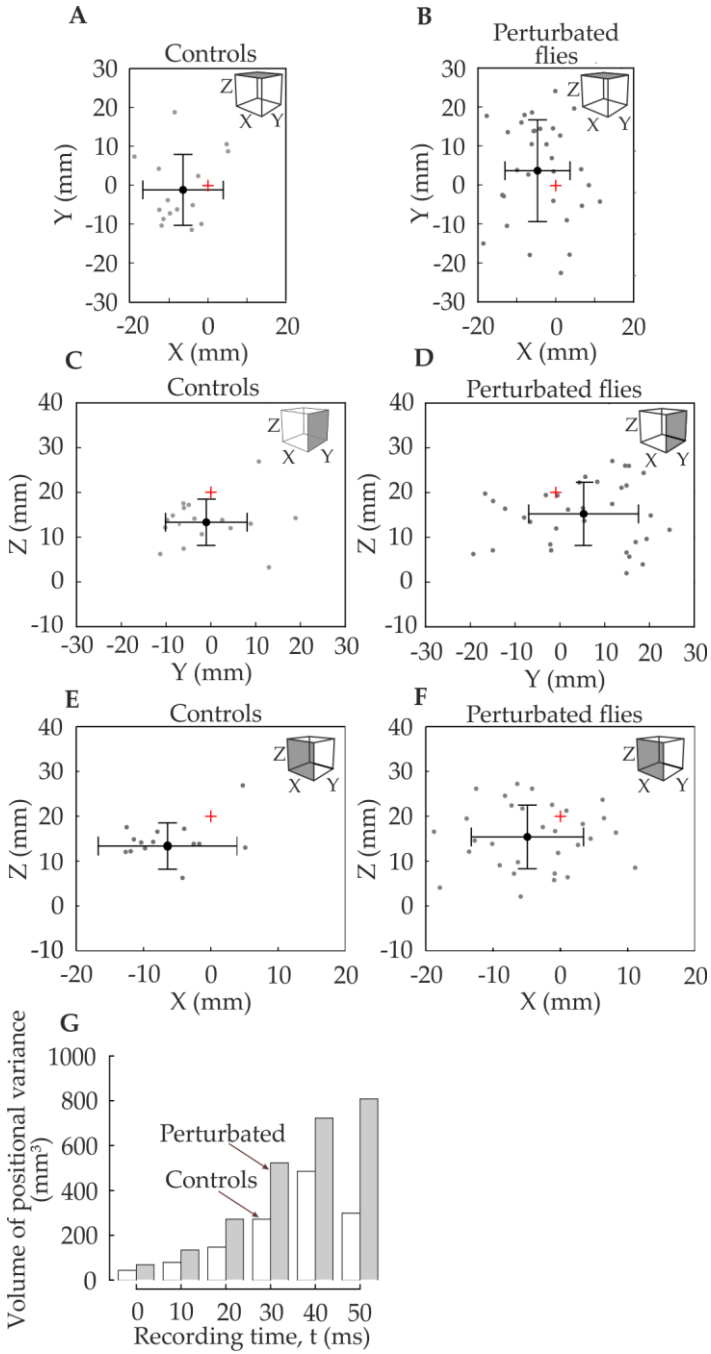
A
Controls
Y (mm)
X (mm)
B
Perturbated flies
Y (mm)
X (mm)
C
Controls
Z (mm)
Y (mm)
D
Perturbated flies
Z (mm)
Y (mm)
E
Controls
Z (mm)
X (mm)
F
Perturbated flies
Z (mm)
X (mm)
G
Volume of positional variance (mm³)
Perturbated
Controls
Recording time, t (ms)

Figure 3-2: Flies positions (grey dots) in turbulent flow (right column, N=44 flies) and non-perturbated flows (left column, N=17 flies) after 40ms of video recording. Mean position and standard deviation of each position (X, Y, Z): -6.42±10.3mm, -1.04±9.1mm, 13.39±5.17mm (controls) and -4.9±8.33mm, 5.27±12.27mm, 15.32±7.07mm (perturbated flies).(A-B) Top view X-Y axis, (C-D) side view Z-Y axis and (E-F) side view Z-X axis. Centre of ROI is (0, 0, 20). (G) Volume of positional variance ($s.d._X \times s.d._Y \times s.d._Z$) of perturbated flies (grey bar) and controls (white bar).

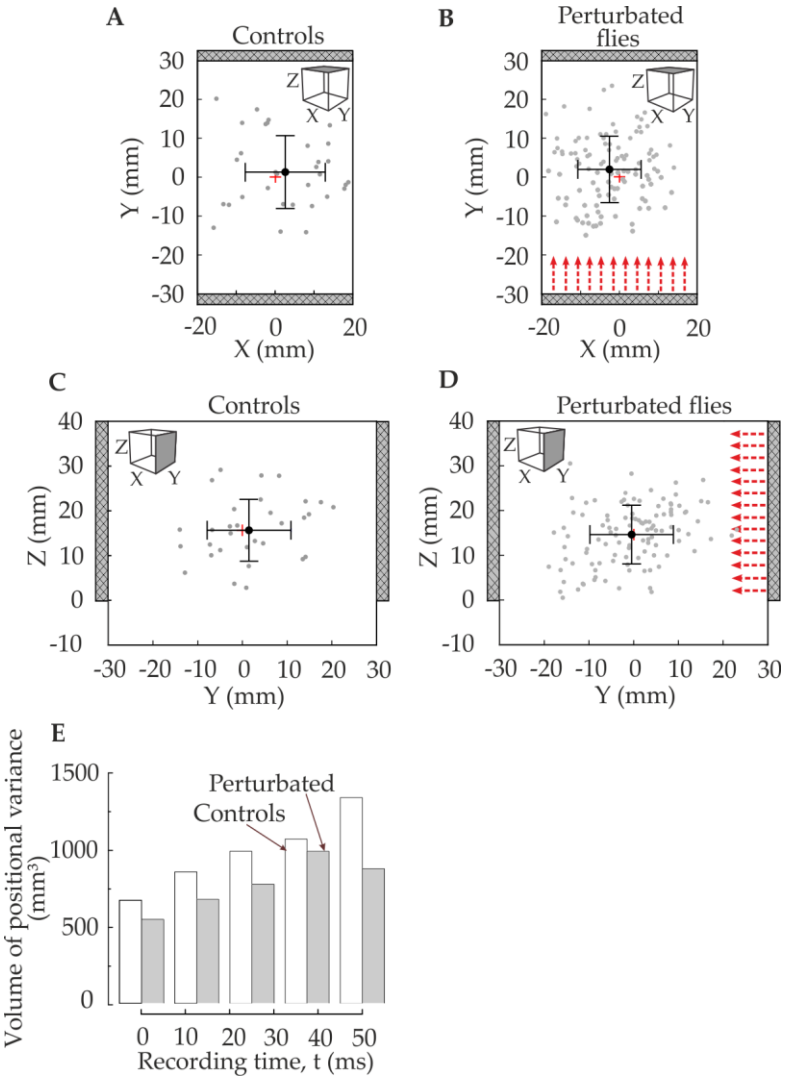

Figure 3-3: Flies position (grey dots) during impulsive perturbation of airjet (right column, N=109 flies) and controls (left column, N=32 flies) at 0ms of video recording, immediately after gust hit the flies. Mean position and standard deviation of each position (X, Y, Z): 2.50±10.29mm, 1.49±9.36mm, 15.74±6.92mm (controls) and -1.09±8.87mm, -0.50±9.31, 14.61±6.58mm (perturbated flies). (A-B) Top view Y-X axis and (C-D) side view Z-Y axis. Red arrows

show flow direction at perturbation onset. (E) Volume of positional variance ($s.d._X \times s.d._Y \times s.d._Z$) of perturbated flies (grey bar) and controls (white bar).

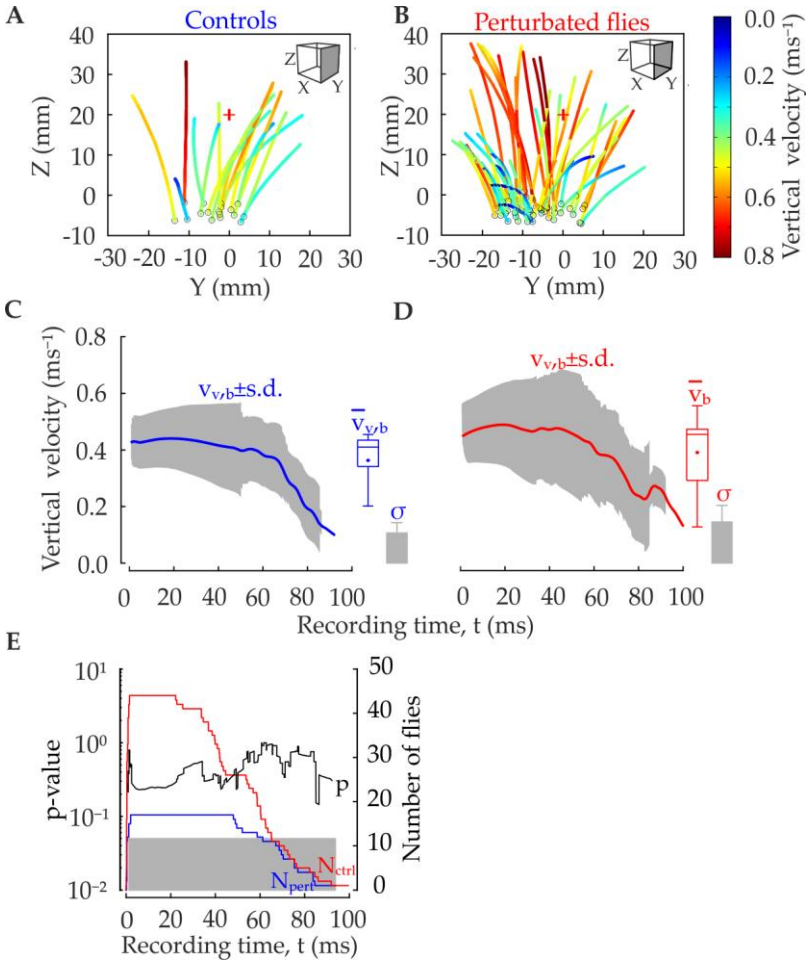

Figure 3-4: Alterations in body vertical translational velocity during continuous perturbation (B and D, red, N=44 flies) compared to controls (A and C, blue, N=17 flies). Velocity in A and B is plotted in pseudo-colour. Black circles show the time when the fly entered the ROI. (Upper row) Flight paths and (middle row) time trace of means and standard deviations (grey area). Inset (boxplots and error bars) shows the temporal means: 0.36±0.10ms^{-1} (controls, C) and

0.39±0.10ms^{-1} (perturbated, D). (E) Statistical comparison (t-test) between perturbated flies and controls. Grey area shows p-value of less than 0.05. Blue (controls) and red lines (perturbated flies) in *E* indicate number of flies used in experiment (right scale).

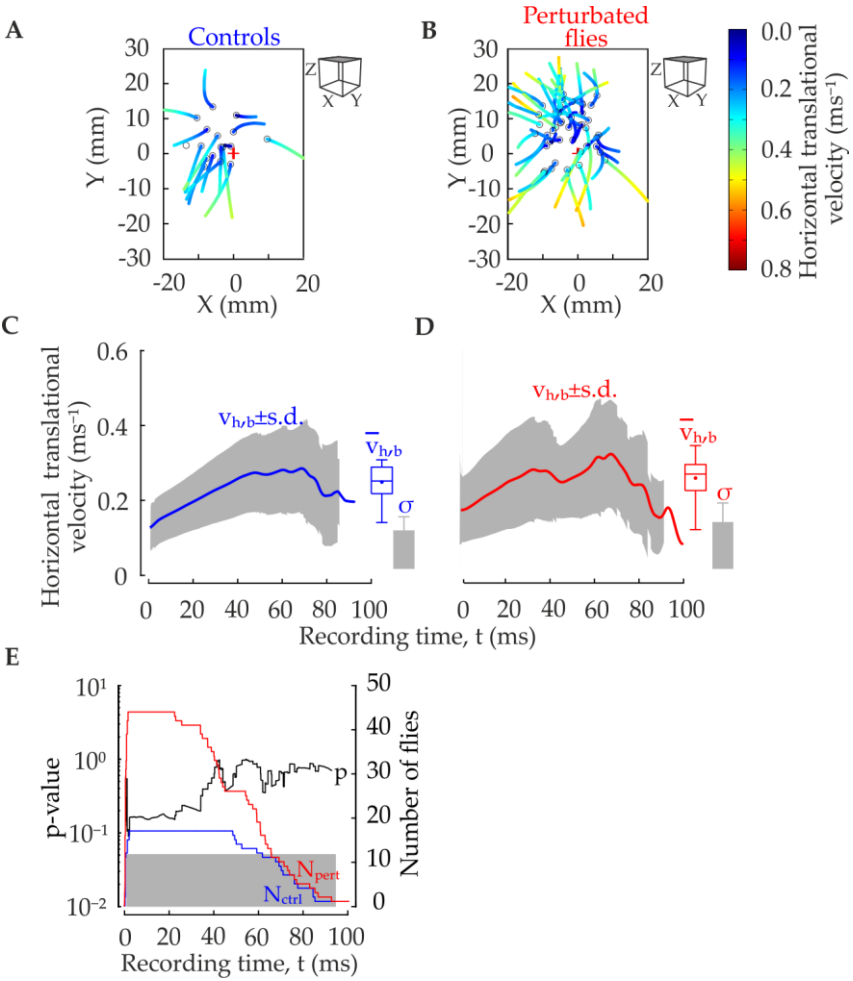

Figure 3-5: Alterations in body horizontal translational velocity during continuous perturbation (B and D, red) compared to controls (A and C, blue). (Upper row) Flight paths and (middle row) time trace of means and standard deviations (grey area). Inset (boxplots and error bars) shows the temporal means: 0.23±0.04ms^{-1} (controls,

C) and 0.24±0.05ms^{-1} (perturbated, D). (E) Statistical comparison (t-test) between perturbated flies and controls. See previous figure legend, Figure 3-4.

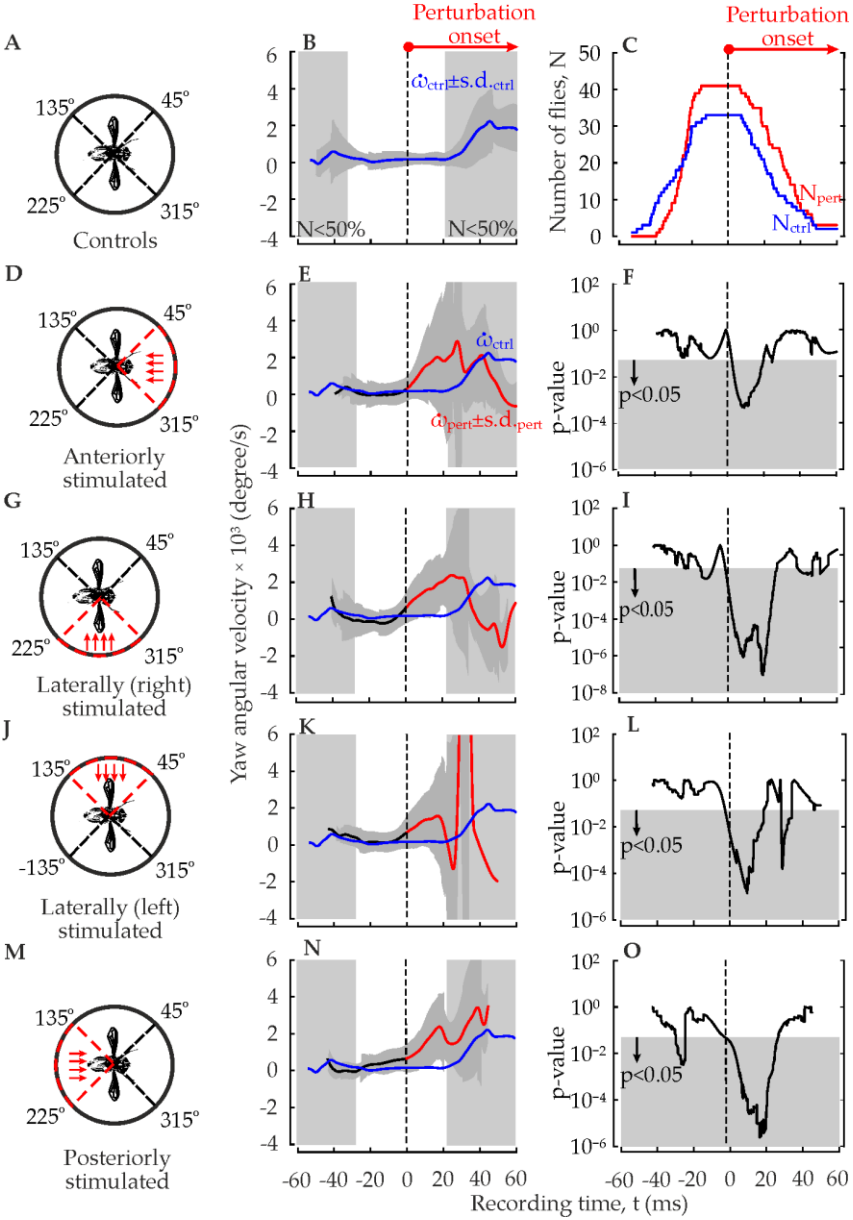

Figure 3-6: Body yaw angular velocities during impulsive perturbation from various directions (perturbated flies, red, N=109 flies; controls, blue, N=32 flies). (A, D, G, J, M) Red arrows in the schematic diagrams show flow direction at perturbation onset. (B, E, H, K, N) Time trace of means and standard deviations (grey area) before ($t<0$ms, black) and during ($t\geq0$ms, red) perturbation. Light grey areas represent time traces with less than 50% total number of animals. (C) Blue (controls) and red lines (perturbated flies) indicate the number of flies used in experiment. (F, I, L, O) Time trace of instantaneous p-values before and during perturbation from anterior (F, N=41 flies), right ventral (I, N=13 flies), left ventral (L) and posterior (O, N=16 flies).Grey areas represent the p-value less than 0.05. Vertical dotted line indicates perturbation onsets.

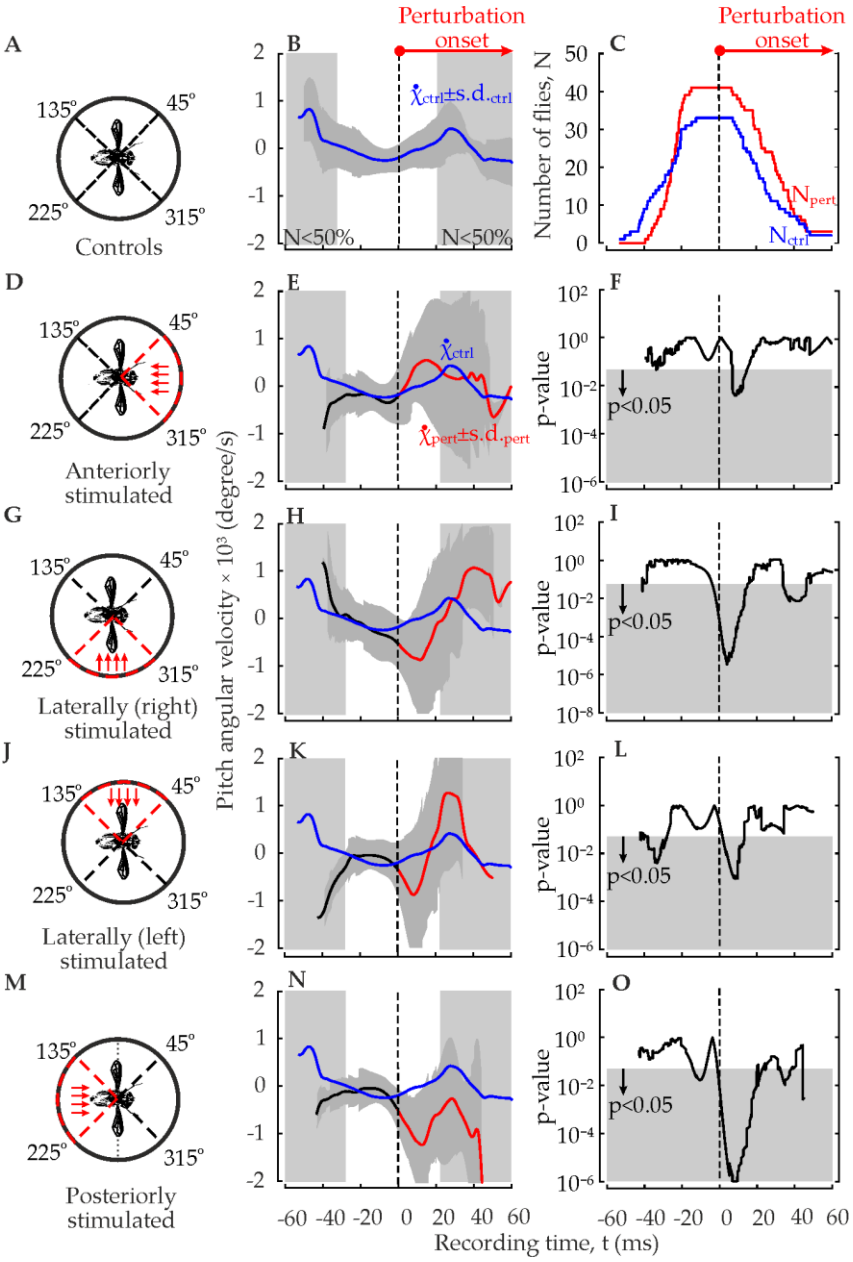

Figure 3-7: Body pitch angular velocities during impulsive perturbation from various directions (perturbated flies, red; controls, blue). (B, E, H, K,

N) Time trace of means and standard deviations (grey area) before (t<0ms, black) and during (t≥0ms, red) perturbation. (C) Blue (controls) and red lines (perturbated flies) indicate the number of flies used in experiment. (F, I, L, O) Time trace of instantaneous p-values before and during perturbation from anterior (F), right ventral (I), left ventral (L) and posterior (O). Positive pitch angular velocities indicate counter clockwise body rotation about its axis. See previous figure legend, Figure 3-19.

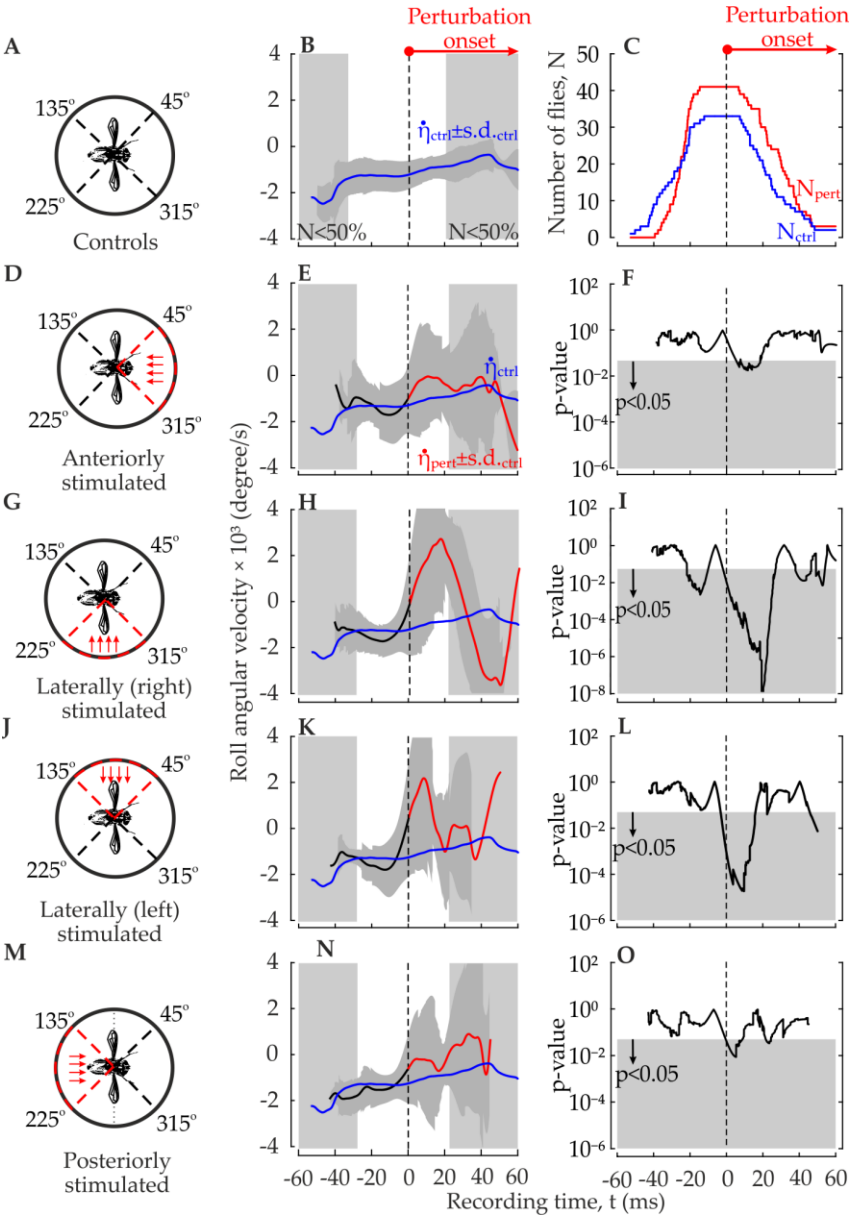

Figure 3-8: Body roll angular velocities during impulsive perturbation from various directions (perturbated flies, red; controls, blue). (B, E, H, K, N) Time trace of means and standard deviations (grey area)

before (t<0ms, black) and during (t≥0ms, red) perturbation. (C) Blue (controls) and red lines (perturbated flies) indicate the number of flies used in experiment. (F, I, L, O) Time trace of instantaneous p-values before and during perturbation from anterior (F), right ventral (I), left ventral (L) and posterior (O). See previous figure legend, Figure 3-19.

3-3. Body posture and motion during take-off

3-3-1. Controls

After take-off from the platform, non-perturbated controls flew on average with 0.36±0.1ms^{-1} vertical translational velocity (Figure 3-4C), which is higher than horizontal translational velocity (0.23±0.1ms^{-1}, Figure 3-5C). At t=0, non-perturbated flies initially flew upward with 0.39±0.12ms^{-1}. Flies then gradually exhibited vertical deceleration when they approached a transition from predominant vertical to horizontal flight manoeuvres. Non-perturbated flies first initiated flight with body angular velocity as listed (43±133°s^{-1}, yaw angular velocity, Figure 3-6B; -37±209°s^{-1}, pitch angular velocity, Figure 3-7B; -15.8±214.5°s^{-1}, roll angular velocity, Figure 3-8B; N=32). Flies take-off with a steep increase of angular pitch velocity (pitch-up acceleration, 18378±89°s^{-2} at t=-7.4ms until 27.4ms). When flies reached a steady flight condition with predominant horizontal translational motion, they gradually decelerated their angular body pitch (nose-down, -41556±140°s^{-2}, t=27.4ms until 45.8ms) presumably due to drag acting on the ventral body surfaces. The change in body roll angle was however relatively minimal (mean, 7.25±1.26°, N=3027 data points). While flying inside camera's ROI, flies' responded to aerodynamic perturbations by systematically altering their body yaw, pitch and roll angular velocity.

3-3-2. Translational velocities

3-3-2-1. Responses to continuous perturbations

Under continuous turbulent conditions, 94% of the tested flies take-off steeply within 4.2±8.2minutes (mean±s.d.) after reached the take-off platform (Figure 3-1). They stabilized their bodies in approximately 43ms, before the fluctuated mean translational velocity continuously decrease (Figure 3-4D). Compared to non-perturbated flies, control flies reached steady flight conditions 12ms later (t=~55ms, Figure 3-4C). This moment is characterised as predominant vertical flight, which gradually reduced because flies' flight manoeuvres change to

horizontal flying trajectories (forward flight, sideslip or even backward manoeuvres). During turbulence, vertical translational velocity exhibited more gradual decrease compared to controls (rate of decrease=-5.89±0.02ms^{-2} started at t=62ms versus controls, rate of decrease =-9.33±0.03ms^{-2} started at t=43ms). Although tested flies altered their vertical translational velocity, the adjustment was relatively small and statistically insignificant (t-test, all instantaneous p>0.05, Figure 3-4E, N=44).

A similar trend holds for mean horizontal translational velocity (0.24±0.05ms^{-1}, Figure 3-5C, N=44), as the tested flies have no significant alterations compared to non-perturbated controls (0.23±0.04ms^{-1}, t-test, all instantaneous p>0.05, N=17, Figure 3-5E). Comparing tested flies and non-perturbated controls, the result indicates that there are no significant differences at any point throughout the statistical comparison of instantaneous velocities within a 100ms flight period (t-test, all instantaneous p>0.05, Figure 3-5E). The transition from a predominant vertical to level flight caused a relatively smoother increase of horizontal velocity of controls than perturbated flies, which demonstrated apparent fluctuations (noticeably at t=40ms). This increasing trend was consistent before horizontal velocity peaked at approximately 68ms and eventually both traces of perturbated flies and controls experienced prompt reductions.

3-3-2-2. Responses to impulsive perturbations

In contrast to experiments with turbulent perturbation, the flight sequences recorded during impulsive perturbation were first aligned to the time at which the airflow reached the body (perturbation onset, t=0). I merged the individual flight traces to a temporal mean value and standard deviation of kinematic data.

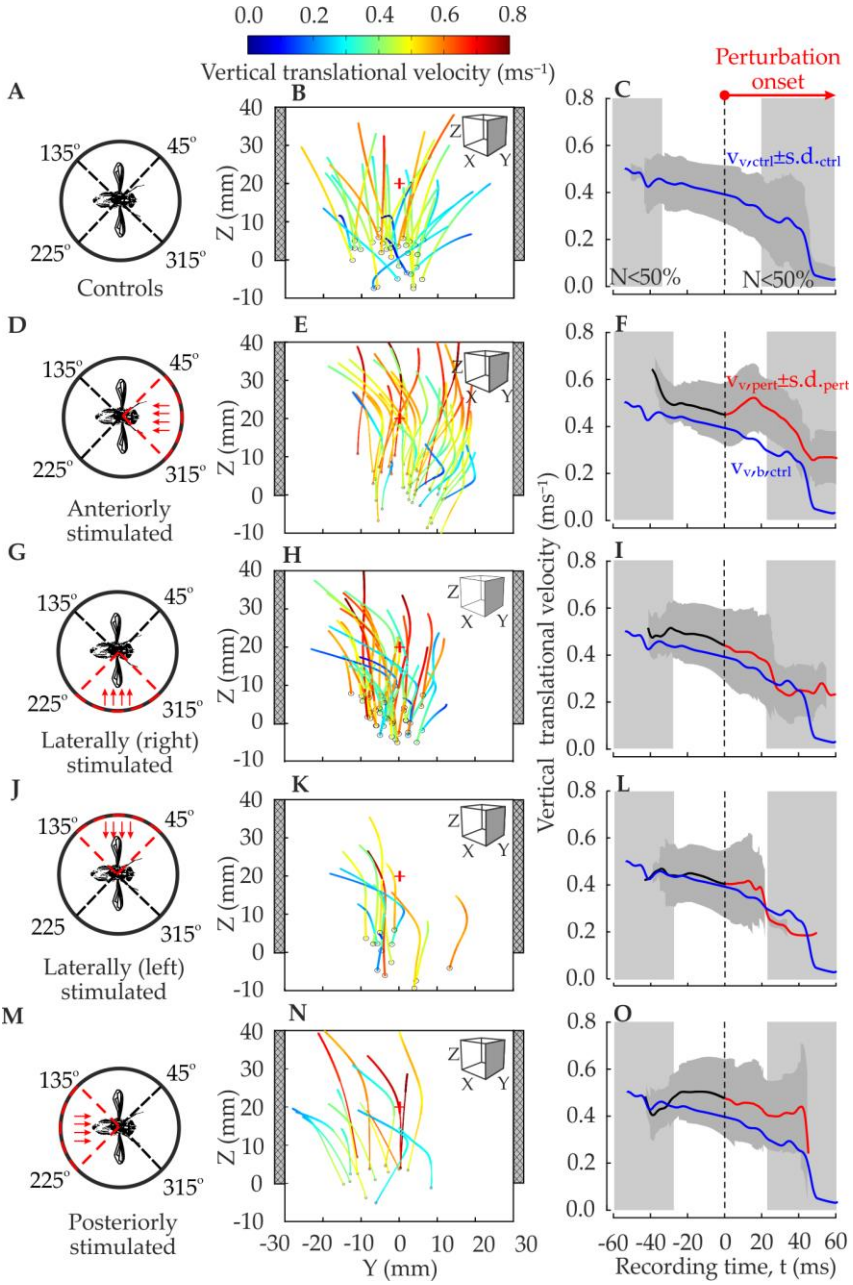
0.0 0.2 0.4 0.6 0.8
Vertical translational velocity (ms⁻¹)
Perturbation onset
A
B
C
135°
45°
225°
315°
Controls
Z (mm)
Y (mm)
Recording time, t (ms)
Vertical translational velocity (ms⁻¹)
v_v,ctrl±s.d.ctrl
N<50%
N<50%
D
E
F
Anteriorly stimulated
v_v,pert±s.d.pert
v_v,b/ctrl
G
H
I
Laterally (right) stimulated
J
K
L
Laterally (left) stimulated
M
N
O
Posteriorly stimulated

Figure 3-9: Body vertical translational velocity during impulsive perturbation from various directions (red) compared to non-perturbated controls (blue). (A, D, G, J, M) Arrows show flow direction at perturbation onset. (B, E, H, K, N) Corresponding flight paths and velocity is plotted in pseudo-colour. Black circles show the time when the fly entered the ROI. Hatch grey rectangles indicate speakers. (C, F, I, L, O) Time trace of means and standard deviations (dark grey area) before ($t<0$ms, black) and during ($t\geq0$ms, red) perturbation. Vertical dotted line indicates perturbation onsets. Controls (N=32 flies), anteriorly perturbated flies (N=41 flies), right laterally perturbated flies (N=39 flies), left laterally perturbated flies (N=13 flies) and posteriorly perturbated flies (N=16 flies). Light grey areas represent time traces with less than 50% total number of animals.

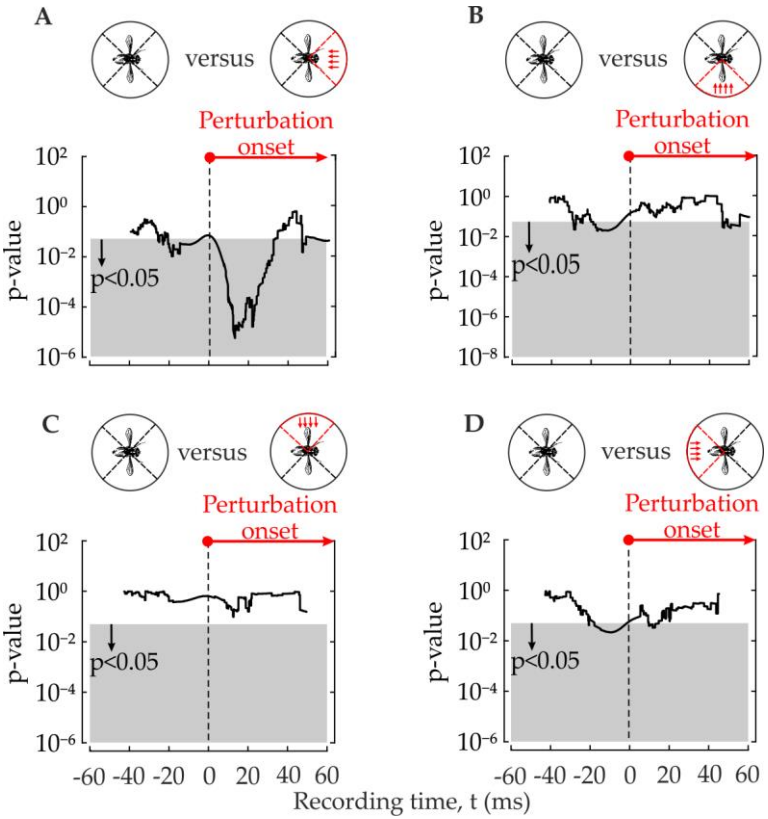

Figure 3-10: Statistical comparison (t-test) of body vertical translational velocity between perturbated flies and non-perturbated controls (N=32 flies). Time trace of instantaneous p-values before and during anterior perturbation (A), left ventral perturbation (B), right ventral perturbation(C) and posterior perturbation (D). Red arrows in the schematic diagrams show flow direction at perturbation onset. Vertical dotted line indicates perturbation onsets. Grey areas represent p-value less than 0.05.

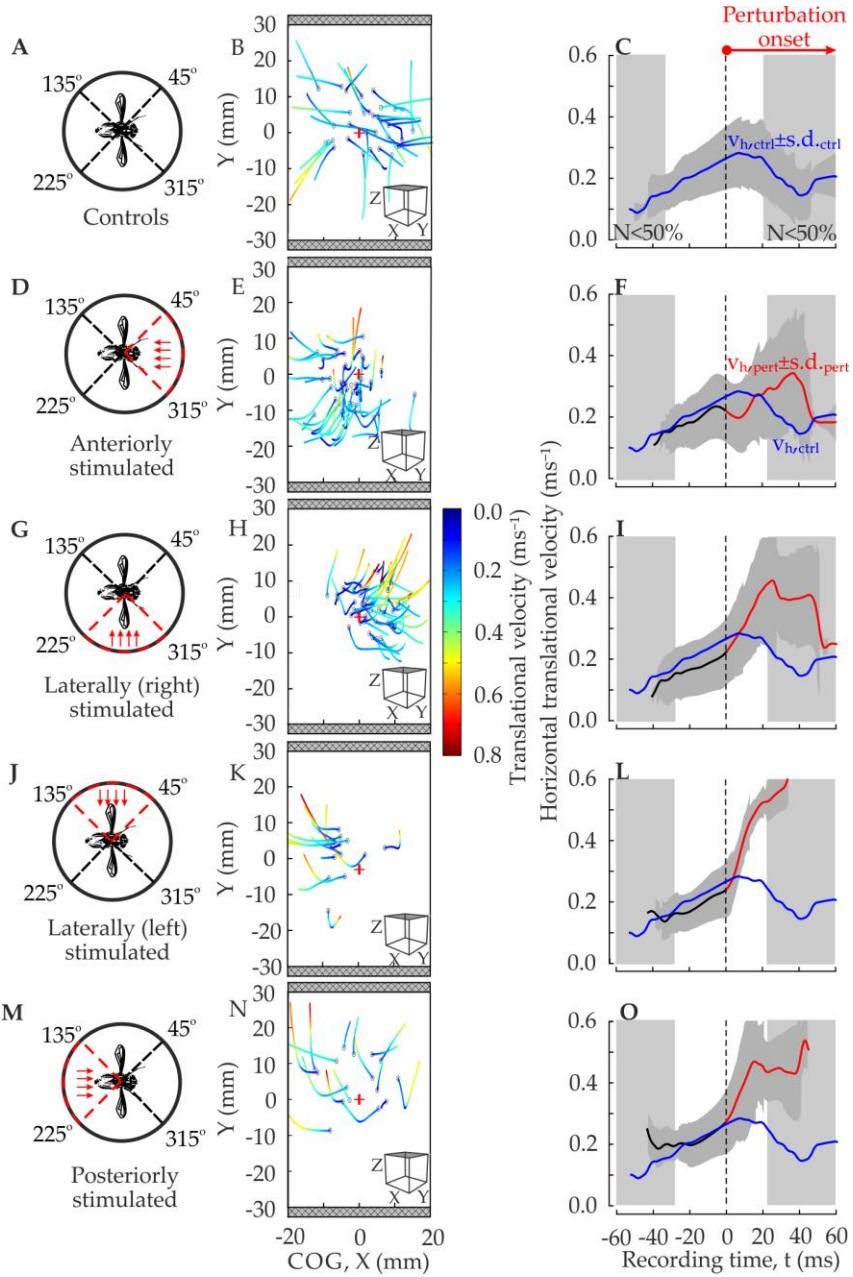
A
135°
45°
225°
315°
Controls
B
Y (mm)
C
Perturbation onset
$v_{h,ctrl}$±s.d.$_{ctrl}$
N<50%
N<50%
D
Anteriorly stimulated
E
F
$v_{h,pert}$±s.d.$_{pert}$
$v_{h,ctrl}$
G
Laterally (right) stimulated
H
I
J
Laterally (left) stimulated
K
L
M
Posteriorly stimulated
N
O
Translational velocity (ms⁻¹)
Horizontal translational velocity (ms⁻¹)
COG, X (mm)
Recording time, t (ms)

Figure 3-11: Body horizontal translational velocity during impulsive perturbation from various directions (red) compared to non-perturbated controls (blue). (C, F, I, L, O) Time trace of means and standard deviations (dark grey area) before (t<0ms, black) and during (t≥0ms, red) perturbation. See previous figure legend, Figure 3-9.

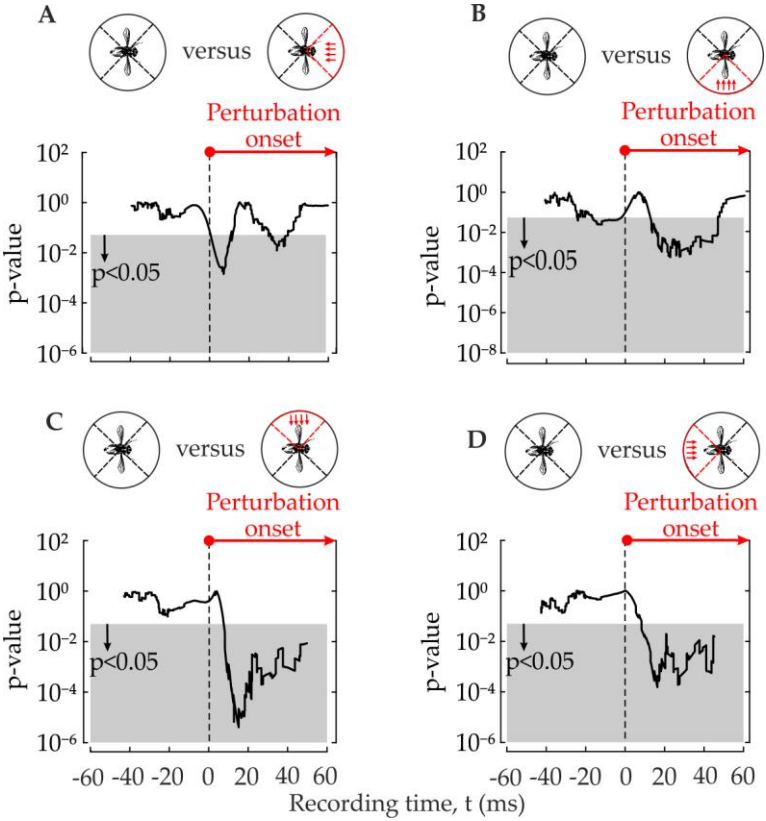

Figure 3-12: Statistical comparison (t-test) of body horizontal translational velocity between perturbated flies and non-perturbated controls. Time trace of instantaneous p-values before (t<0ms) and during (t≥0ms) anterior perturbation (A), left ventral perturbation (B), right ventral perturbation (C) and posterior perturbation (D). See previous figure legend, Figure 3-10.

In all cases, the tested flies initially demonstrated vertical decelerations (controls, -2.47±0.01ms^{-2}; right lateral perturbation, -2.64±0.01ms^{-2}; left lateral perturbation, -1.46±0.02ms^{-2} posterior perturbation, -1.64±0.02ms^{-2}; Figure 3-9C, I, L and O) except in one case of flies facing anterior perturbation. Perturbation from anterior caused an increase in vertical body velocity (rate of increase 5.56±0.02ms^{-2}, correlation analysis between velocity and time, r=0.98 at t=0ms until 16ms, 958 data points, Figure 3-9F) compared to non-perturbated controls. This increase of vertical velocity reached a maximum changes at 16ms after perturbation onset, thus ended upward body motion. The temporal rate of change in body elevation coincidently increased with the growth of perturbation strength. As the strength of perturbation is weakened, the vertical translational velocity declined until the flies achieved steady horizontal flight manoeuvres. Thereby, vertical translational velocity was significantly different between anteriorly perturbated flies and controls at t=2.6ms and last at t=30ms (89% of the time after perturbation onset, t-test, all instantaneous p<0.05, Figure 3-10A).

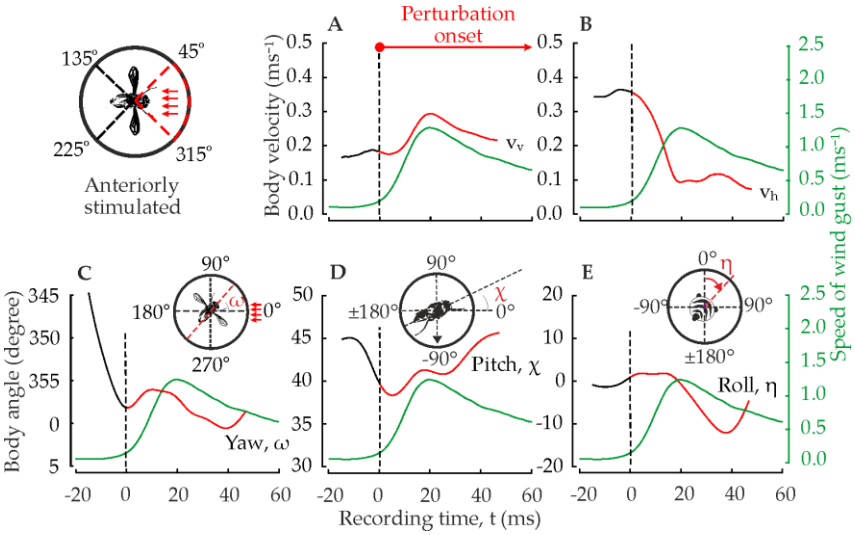

Figure 3-13: Example of flight behaviour of a single fly facing impulsive perturbation from anterior. Arrows show the direction of the oncoming perturbation. Time traces of body (A) vertical translational velocity, (B) horizontal translational velocity, (C) yaw angle, (D) pitch angle and (E) roll angle before (t<0ms, black) and during (t≥0ms, red) perturbations. Vertical dotted line indicates perturbation onsets. Green trace shows mean speed of

the wind gust (right scale). All positive angles (yaw and roll) indicate clockwise rotation about their axes, except pitch.

In addition, impulsive anterior perturbation initially caused horizontal deceleration (-3.75±0.02ms^{-2}, Figure 3-11F), which differs from other cases (right lateral perturbation, 10.5±0.02ms^{-2}; left lateral perturbation, 14.65±0.08ms^{-2}; posterior perturbation, 13.88±0.02ms^{-2}; Figure 3-11C, I, L and O). However, this deceleration reached a minimum value after 12ms and flies regained previous body horizontal velocity or approximately two wing strokes after perturbation onset. An exemplary flight sequence also confirmed that anterior perturbation elicits passive braking, thereby reduced fly's heading velocity (rate of braking 15.95±0.08ms^{-2}, correlation analysis between velocity and time, r=0.97 at t=0ms until 19ms, 1140 data points, Figure 3-13B). It took approximately 19s to reduce horizontal velocity to 73% of its maximum value (0.037±0.02ms^{-1} of peak value versus 0.11±0.01ms^{-1} minimum level). Statistical tests also revealed that only flies facing anterior perturbation regained their previous horizontal velocity after perturbation in 11ms (begin at t=1ms and last at t=12ms, t-test, all instantaneous $p<0.05$, Figure 3-12A).

3-3-3. Angular velocities

3-3-3-1. Responses to continuous perturbations

Under turbulent conditions, the yaw angular velocity of the tested flies decreased to -188±577°s^{-1} (6.4-fold of reduction compared to controls, 43±133°s^{-1}), which was not significantly different compared to non-perturbated flies (t-test, all instantaneous $p>0.05$, Figure 3-14A-C). By contrast, body pitch and roll angular velocity significantly change during continuous perturbations compared to controls. Comparing the perturbated flies with controls, it can be seen that pitch angular velocities of both cases were significantly different (first alteration occurred 40ms after take-off and lasted after 3ms; second alteration then occurred 72ms after take-off and lasted after 5.8ms; t-test, all instantaneous $p<0.05$, Figure 3-14F). A similar trend holds for roll angular velocity, as the first alteration occurred 64ms after take-off and lasted after 6ms. After this initial response, the second adjustment occurred 85ms after take-off and lasted shortly after 1.3ms (t-test, $p<0.05$, Figure 3-14I). In total, after take-off, only 7.3% of instantaneous p-values for pitch angular velocity and 9% of instantaneous p-values for roll angular velocity were below 0.05. Under turbulent conditions, overall pitch angular velocity was -261±301°s^{-1} (7-fold of decrease compared to non-perturbated controls, -37±209°s^{-1}) and roll angular velocity reduced to -293±760°s^{-1} (18.5-fold of decrease compared to non-perturbated

controls, -15.8±214.5°s^{-1}). Thus, flies that facing turbulence experienced higher alterations of body pitch angular velocity than roll angular velocity and yaw angular velocity.

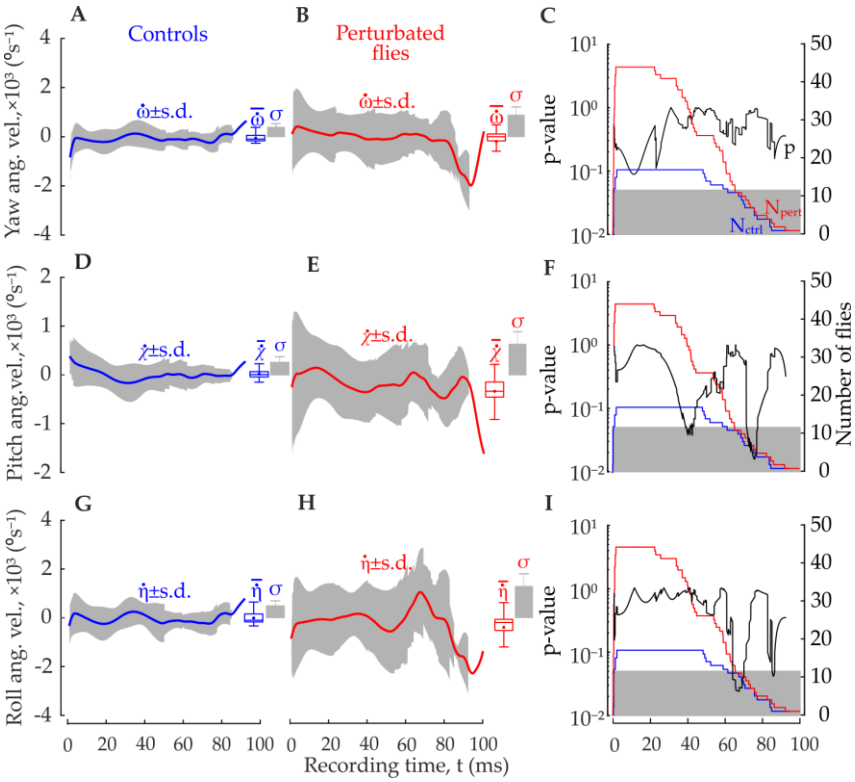

Figure 3-14: Body kinematics responding to continuous perturbation (middle column, red, N=44 flies) and controls (left column, blue, N=17 flies). (A, B, D, E, G, H) Time trace of body (A-B) yaw angular velocity, (D-E) pitch angular velocity and (G-H) roll angular velocity. Inset (boxplots and error bars) show mean values, medians and standard deviation of body angular velocity over all data points. (C, F, I) Time traces of statistical comparison (t-test) between continuously perturbated flies and controls (left scale). Blue (controls) and red lines (perturbated flies) in C, F and I indicate the number of flies used in experiment (right scale). All positive angular velocities (yaw and roll) indicate clockwise body rotation about their axes except pitch.

3-3-3-2. Responses to impulsive perturbations

Similarly, flies facing impulsive perturbations also experienced distinguishable alterations on body angular velocities compared to non-perturbated controls (Figure 3-6-Figure 3-8). Before perturbation onset ($t<0$), body angular velocity was similar in both perturbated and non-perturbated flies (-200.2±94.15°s^{-1} for pitch angular velocity; 44.4±132.4°s^{-1} for yaw angular velocity; -32±207.2°s^{-1} for roll angular velocity; N=1660 dataset). Impulsive perturbation from any direction caused a transient yaw angular acceleration (left lateral perturbation, 57609±284°s^{-2} at t=-3ms until 17ms; right lateral perturbation, 67780±200°s^{-2} at t=-1.5ms until 25ms; anterior perturbation, 68312±659°s^{-2} at t=-2.4ms until 18ms; posterior perturbation, 94628±550°s^{-2} at t=-3ms until 18.5ms; Figure 3-6E, H, K, N). In many cases, flies began the alteration of yaw angular velocity before stimulus onset at $t<0$ (posterior perturbation, t=-3ms until 26.5ms; left lateral perturbation, t=-2.9ms until 18.4ms; right lateral perturbation, t=-1.5ms until 26.8ms) except for anterior perturbation (t=2.4ms until 20ms). The alteration is judged to be statistically significant when the instantaneous p-value of t-test was less than 0.05. According to the statistical comparison (t-test, instantaneous p-value), flies then regained previous yaw angular velocity in 17.5ms for anteriorly perturbated flies, 21.3ms for left laterally perturbated flies, 28.2ms for right laterally perturbated flies, and 29.5ms for posteriorly perturbated flies (Figure 3-6F, I, L, O). During lateral perturbation, 84% of the tested flies turned their body in the direction of the stimulus compared to only 16% towards oncoming perturbation (N=52 flies). By contrast, a single perturbated fly with interchanged body yaw rotation immediately stopped turning after the anterior perturbation reached body's centre of gravity (Figure 3-13C). Wind gust later turned the fly in the direction of perturbation (counter clockwise yaw rotation, 264±1.57°s^{-1}), presumably due to the acting drag on fly's body. After 10ms, it managed to elicit counter rotation (clockwise yaw rotation, 140.3±2°s^{-1}) and streamlined its body with airflow (ω=0°) and moved upwind within 29ms.

In many cases, impulsive perturbation initially caused pitch-down moment (right lateral perturbation, -33226±187°s^{-2} at t=-4ms until 11.25ms; posterior perturbation, -61870±215°s^{-2} at t=0ms until 13.27ms; left lateral perturbation, -69010±160°s^{-2} at t=1ms until 8.2ms; Figure 3-7H, N, K) except in one case of flies facing anterior perturbation (pitch-up, 54115±246°s^{-2} at t=-5.5ms until 15.1ms, Figure 3-7E). During anterior perturbation, the perturbated flies passively delayed the alteration of pitch angular velocity 7.3ms after perturbation onset (t-test, $p<0.05$, Figure 3-7F). The alteration lasted after 8ms, and perturbated flies regained their previous pitch angular velocity. For other cases, the initial responses of pitch-down angular deceleration reached the

minimum value after 8.2ms for left laterally perturbated flies, 11.3ms for right laterally perturbated flies and 13.3ms for posteriorly perturbated flies, respectively (Figure 3-7H, K, N). After these initial responses, flies then noticeably performed a recovery pitch-up acceleration (132667±390°s^{-2} for left laterally perturbated flies at t=8.2 until 26.6ms; 71326±173°s^{-2} for right laterally perturbated flies at t=11.3 until 40ms; 77121±820°s^{-2} for posteriorly perturbated flies at t=13.3 until 29ms) and eventually regained previous non-perturbated body pitch angle. Apparently, anteriorly perturbated flies regained previous body pitch angle in 8ms, relatively quicker than other direction of perturbations (11.6ms during left lateral perturbation, 18.7ms during right lateral perturbation and 24ms during posterior perturbation).

Wind gust from anterior causes only a small change in roll angle (0.46±1.3°) began at 5ms after perturbation onset (t-test, $p<0.05$, Figure 3-8F). Anterior impulsive perturbation increased the roll angular velocity at a rate of increase of 94741±308°s^{-2} (correlation analysis between velocity and time, r=0.99 at t=2.4ms until 18ms, 936 data points, Figure 3-8E), which is lower than flies perturbated from the laterals (left, 171271±888.2°s^{-2} at t=-3.5ms until 16ms, Figure 3-8K; right, 176660.5±665°s^{-2} at t=-2ms until 27ms, both correlation analysis between velocity and time are r=0.9, Figure 3-8H). Anteriorly and posteriorly perturbated flies also performed fast recovery in 9ms and 13ms compared to laterally perturbated flies (29ms for right perturbation and 19ms for left perturbation, t-test, $p<0.05$). According to an exemplary fly (Figure 2-13E), during anterior perturbation, fly rotated its body about the roll axis (roll angular velocity of 670±1.67°s^{-1} for 24.6ms) up to 12° before regained previous non-perturbated flight condition (rate of recovery=847.5±8.8°s^{-1}, correlation analysis between velocity and time, r=0.95 began at t=38ms). By contrast, during lateral perturbation, tested flies altered their roll angular velocity before perturbation onset (left laterally perturbated flies at -3.5ms, Figure 3-8L; right laterally perturbated flies at -2ms, Figure 3-8I; t-test, $p<0.05$), compared to flies perturbated from the anterior (5ms after perturbation onset, Figure 3-8F). This is because lateral impulsive perturbation first reached the wing than any other body part. Thus, wings which are directly connected to the body generate a high amount of drag that promptly alter body angle, even before perturbation onset ($t<0$).

3-4. Numerical modelling for directional sensitivity of posture responses

Until now, I have described the translational and rotational responses of the fly's body facing 4 directions of the impulsive airflow. To further examine the directional sensitivity and the mechanistic link between body posture and the

direction of perturbation, I varied the angle of horizontal perturbation in steps of 30° around the fly's body (12 subgroups, Figure 2-6B).

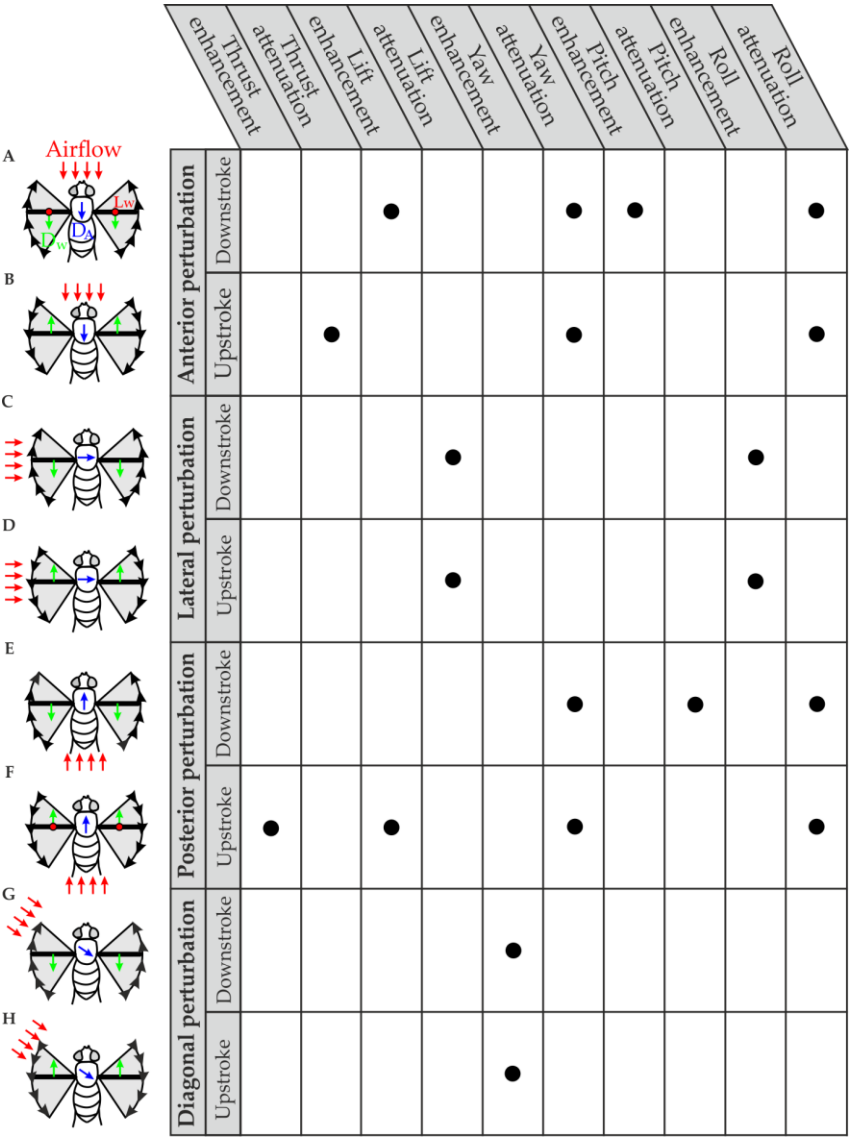

Figure 3-15: Prediction on maximum and the minimum aerodynamics effect from the airflow considered from the beating wings. Schematic

diagrams show body orientation during perturbation onset including the direction of wings' motions (black arrows) and flow direction (red arrows). Grey area indicates wing stroke. Blue arrows on the thoraxes represent the direction of drag due to flow D_A, green arrows show the direction of drag due to wing flapping D_w, and red filled circle on the wings represent lift due to wing flapping L_w.

To understand how the measured changes in body posture depend on the direction of the generated impulsive airflow (body directional sensitivity, cf. chapter 3-3-2 on translational responses and chapter 3-3-3 on rotational responses), I developed a simple numerical model and compared these hypothetical models with the data measured at 0ms, 5ms and 10ms after perturbation onset. The coefficient of determination, R^2 and angular-linear correlation, r_c are the key outputs or statistical indicators determine how well the hypothetical model fit the experimental data (1 indicates that the model perfectly fits the data, while 0 does not fit at all).

Net physical force is a vector quantity acting on the body which moving within a fluid that can be further resolved into 2 orthogonal components, lift and drag (Dudley, 2002). For modelling, I assumed that the laminar impulsive airflow induces aerodynamic forces and moments depending on changes in lift and pressure drag on body and wings. Since body lift is thought to be small (Berthé and Lehmann, 2015) and body drag which depends on body angle is presumably rather independent of flow direction (Cheng et al., 2010; Ellington, 1984a; Sun and Wu, 2003), I only considered the oscillating wings (Figure 3-15). In general, body drag should always align in parallel with the direction of the stimulus and oppose to flight heading. According to conventional aerodynamics analysis of flapping animal flight (quasi-steady approach), I assumed that lift and drag depend on wing orientation, effective surface area and the square of velocity of the oncoming air (Ellington, 1984a; Sane and Dickinson, 2002; Walker, 2002). The impulsive wind gust may enhance or attenuate the relative velocity component normal to wing's longitudinal axis, depending on stimulus direction and wing's angular position within the stroke cycle (cf. Chapter 3-5). The resulting changes of instantaneous lift and drag may eventually alter body orientation, which includes translational and rotational body motion owing to left-right asymmetries in force production (Dudley, 2002).

3-4-1. Modelling translational components

A change in translational body motion in the vertical depends on the body lift, while horizontal motion depends on body drag. Thus, flow from anterior (0°) likely enhances lift during downstroke (Figure 3-15A) and attenuates lift during upstroke (Figure 3-15B). By contrast, posterior wind gust (180°) attenuates lift during downstroke (Figure 3-15E) and enhances lift during upstroke (Figure 3-15F). The same holds for drag production. It is challenging to predict the exact changes in the cycle-averaged aerodynamic lift because of the kinematics differences between up- and downstroke wing motions. I thus assumed that lift enhancement always outscores lift attenuation, and vertical body motion is then only due to a net beneficial increase in flow velocity at the wings.

This assumption can be explained by using a simple consideration of a fly flapping at $4ms^{-1}$ wing velocity and confronting $1ms^{-1}$ airspeed of headwind. Lift depends on velocity squared. Therefore, for non-perturbated control, lift L~16. Under impulsive wind gust, however, subtraction of the airspeed to wing velocity during upstroke results L~9, thus attenuation is 7 compared to control. During downstroke, the additional airspeed of wingtips velocity results L~25, thus enhancement is 9 compared to control. Therefore, the enhancement is more effective (by a value of 2) than attenuation because lift significantly depends on velocity squared.

Meanwhile, posterior wind gust (180°) augment thrust production during upstroke that offsets body drag in forward flight. Besides, wind gusts from lateral (90°, 270°) should have little effect on both mean lift and drag because flows mainly changes the axial flow components on the wings (Figure 3-15C, D).

The predicted relative velocity of between body motion and the stimulus directions were modelled as a simple sine wave:

$$v = A\sin\left[\pi\frac{(\gamma-\varphi)}{P}\right]+\varsigma \qquad (3\text{-}1)$$

Where;

v = body velocity dependent on flow direction (translational, rotational),
A = maximum body velocity and also known as amplitude,
ϕ = phase shift of the responses,
P = rate of change of body velocity in units per time and also known as period,
ζ = offset of the responses, and
γ = direction of stimulus.

Table 3-1: List of the parameters used to compare the numerical modelling with the body kinematic responses of tested flies.

Body velocity	**Time (ms)**	**Amplitude (A)**	**Phase shift (φ°)**	**Period (P°)**	**Offset (ζ)**	**Coefficient of determination (R^2)**	**Angular-linear Correlation (r_c)**
Vertical translational velocity	0	0.02	135	90	0.44	0.12	0.50
	5	0.03	135	90	0.43	0.19	0.42
	10	0.05	135	90	0.44	0.33	0.49
Horizontal translational velocity	0	0.04	90	180	0.24	0.38	0.73
	5	0.08	90	180	0.27	0.60	0.83
	10	0.09	90	180	0.32	0.43	0.78
Yaw angular velocity	0	221.5	90	90	631.1	0.12	0.42
	5	354.9	90	90	962.2	0.10	0.30
	10	230.6	90	90	1560	0.02	0.23
Pitch angular velocity	0	-52.13	90	180	-341.6	0.02	0.36
	5	-354.4	90	180	-473.7	0.21	0.47
	10	-645.1	90	180	-502.6	0.37	0.62
Roll angular velocity	0	586	45	90	1269	0.55	0.14
	5	1049	45	90	2059	0.52	0.14
	10	1333	45	90	2327	0.35	0.25

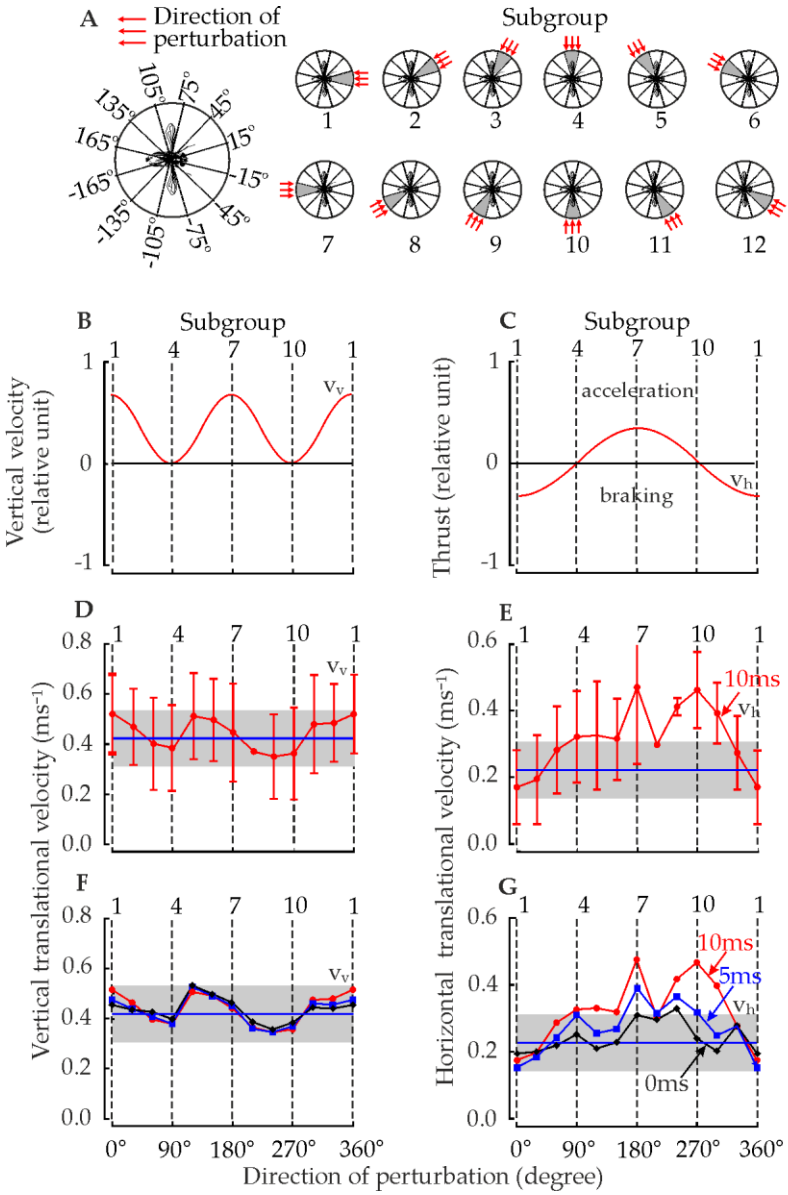

Figure 3-16: Directional tuning curves of body translational velocity (cf. Experimental condition, Figure 2-6B). (A) Body orientation during perturbation. Arrows in the schematic diagrams show flow direction at perturbation onset. (B-C) Modelling of directional

sensitivity. (D, E) Body translational velocity at 10ms after perturbation onset plotted as function of flow direction during perturbation onset. Values are means±s.d.. (F, G) Mean body translational velocity at 0ms (black) at 5ms (blue) and at 10ms (red) after perturbation onset plotted as function of flow direction. Horizontal blue lines in *D-G* are mean body angles of non-perturbated controls and the grey area is the standard deviation. Controls (N=32 flies) and perturbated flies (N=109 flies).

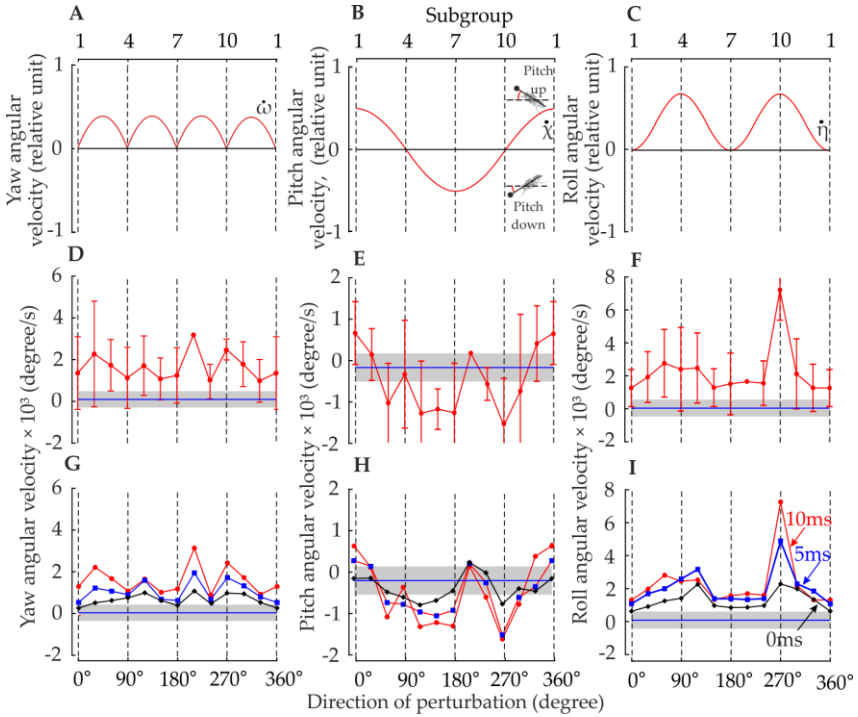

Figure 3-17: Directional tuning curves of body angular velocity (cf. Experimental condition, Figure 2-6C). (A-C) Modelling of directional sensitivity. (D-F) Body angular velocity at 10ms after perturbation onset plotted as function of flow direction during perturbation onset. Values are means±s.d.. (G-I) Mean body angular velocity at 0ms (black) at 5ms (blue) and at 10ms (red) after perturbation onset plotted as function of flow direction. Vertical blue lines in *D-I* are mean body angles of non-perturbated controls and the grey area is the standard deviation. Controls (N=32 flies) and perturbated flies (N=109 flies). All

positive angular velocities (yaw and roll) indicate clockwise rotation about their axes except pitch.

Owing to the consideration explained previously, vertical body motion in response to changing stimulus directions was consequently modelled as a sine wave in which maximum upward force (positive lift) occurs at 0° (flow from anterior) and 180° (flow from posterior) flow direction (Figure 3-16B). Vertical body motion was modelled as below where A and ζ of each measurement time are listed as in Table 3-1:

$$v_{b,v} = A\sin\left\{\pi\frac{(\gamma - 135)}{90}\right\} + \varsigma \tag{3-2}$$

According to Table 3-1, after 10ms of perturbation onset, the maximum vertical translational body velocity, A showed a linear increase over time (y=0.003x+0.018, r=0.98; at t=0ms until 10ms) whereas offsets of the responses, ζ remained constant at 0.43ms^{-1}-0.44ms^{-1}. Meanwhile, within 10ms after perturbation onset, the coefficient of determination of vertical translational velocity, R^2 significantly increased with increasing time (y=0.021x+0.108, r=0.98, r_c=0.47±0.04; at t=0ms until 10ms).

Horizontal body translational motion (Figure 3-16C), depends on drag produced by the flapping wings. Drag maximally attenuates forward thrust (braking) at flow from 0° (flow from anterior) while maximally enhance thrust at 180° flow direction (flow from posterior). Horizontal body motion was modelled as below where A and ζ of each measurement time are listed in Table 3-1:

$$v_{b,h} = A\sin\left\{\pi\frac{(\gamma - 90)}{180}\right\} + \varsigma \tag{3-3}$$

According to Table 3-1, the maximum horizontal translational body velocity, A gradually increased with the increasing time (y=0.005x+0.045, r=0.94; at t=0ms until 10ms). A similar trend held for the offsets of the responses, ζ as its value also continuously increased over time (y=0.008x+0.24, r=0.99; at t=0ms until 10ms). Meanwhile, the coefficient of determination of horizontal body motion, R^2 fluctuated around 0.47±0.12. After 5ms of perturbation onset, the coefficient of determination of horizontal body motion, R^2 reached up to 0.6 (r_c=0.83 also the highest angular-linear correlation of kinematic parameters of body motion), which relatively higher compared to other body motion parameters (where 60% of the variability between the variables that have been accounted).

3-4-2. Modelling rotational components

Similar to body translation, rotational motion (yaw, pitch and roll) depends on both the flow direction and the changing moment arm (distance between the wing hinge and the animal's centre of mass) within each stroke cycle. Yaw moments result from asymmetric drag force generation by left and right wing (Ristroph et al., 2010; Ristroph, 2011). Flow from anterior (0°) and posterior (180°) should thus have no effect on yaw, although moment arm length is maximum throughout the entire stoke cycle. The same trend also holds for lateral flows (90°, 270°) because in this case drag-induced moments owing to the flow stimulus change sign at mid-up and downstroke and are thus balanced in each half stroke (Figure 3-15C, D). Consequently, yaw-induced body rotation was modelled with maximum responses at one-quarter and three-quarters up and downstroke, respectively (Figure 3-17A). Yaw angular velocity can be written by using a rectified sine wave as below where A and ζ of each measurement time are listed in Table 3-1:

$$\dot{\omega} = A\left|\sin\left\{\pi\frac{(\gamma-90)}{90}\right\}\right| + \varsigma \qquad (3\text{-}4)$$

After 5ms of stimulus onset, the maximum yaw angular body velocity, A_ω increased to 60% (355°s^{-1} versus 221.5°s^{-1} at t=0ms), but then decreased by 35% (230.6°s^{-1}) after 10ms of the onset (Table 3-1). By contrast, offsets of the responses, ζ_ω significantly increased with the increasing time (y=92.9x+587, r=0.99). The coefficients of determination of yaw angular velocity, R_ω^2 were relatively low (0.08±0.05) and increased over time (y=-0.01x+0.13, r=-0.94, r_c=0.32±0.01, at t=0ms until 10ms).

Moments for pitching depend on body angle and vary throughout the stroke cycle due to the change of stroke angle (Lehmann and Pick, 2007). Pitch moments predominately depend on changes in the mean vertical force of both wings at the stroke reversals (Balint and Dickinson, 2004). Thus, the moment arm for pitch is minimal at mid-strokes. Dorsal stroke reversal should have a higher impact on body pitch control because of the asymmetries in stroke angle and the moment arm is longer at this time of the stroke cycle compared to the ventral stroke reversal (cf. Figure 2-13). Moreover, owing to the banana-shaped stroke profile of wingtip trajectory (Figure 2-13H, (Ellington, 1984b)), the erected wings at the dorsal stroke reversal are likely more prone to changes in flow velocities than at the ventral reversal. Thus, drag in the direction of the airflow is thought to modulate pitching motion: nose-down pitching moments occurs when wings

experience perturbation from posterior (180°, Figure 3-15E) and nose-up moments owing to flow from anterior (0°, Figure 3-15A). Therefore, the predominant effect mainly occurred when flies experienced wind gust parallel to the longitudinal body axis (Figure 3-17B). I modelled the pitch angular velocity as below where A and ζ of each measurement time are listed in Table 3-1:

$$\dot{\chi} = \mathrm{A}\sin\left\{\pi\frac{(\gamma-90)}{180}\right\}+\varsigma \tag{3-5}$$

The maximum pitch angular body velocity, A_χ and its fitting offsets, ζ_χ continuously decreased after 10ms of perturbation onset (y=-59.2x-54, r=-0.99 for amplitude and y=-16x-38, r=-0.94 for offsets, at t=0ms until 10ms, Table 3-1). By contrast, within 10ms after perturbation onset, the coefficient of determination of pitch angular motion, R_χ^2 significantly increased with the increasing time (y=0.035x+0.025, r=0.98, r_c=0.48±0.13, at t=0ms until 10ms).

The moment arm for roll moments is the longest when wings are positioned normal to the longitudinal body axis approximately at mid wing stroke (Φ=0° stroke angle) (Balint and Dickinson, 2004; Beatus et al., 2015; Combes and Dudley, 2009). This is because wings are bilaterally paired appendages, any asymmetry in force production by wings will result moments about the roll axis (Figure 3-15C, D). Therefore, the roll should be most sensitive to impulsive perturbation from lateral because at midstroke moment arm is longest (90°, 270°, Figure 3-17C, F, I). Also, during body roll, the flight force vector is offset from the vertical and thus flies loose body lift (Beatus et al., 2015; Mronz and Lehmann, 2008). I modelled roll angular velocity as below where A and ζ of each measurement time are listed in Table 3-1:

$$\dot{\eta} = \mathrm{A}\sin\left\{\pi\frac{(\gamma-45)}{90}\right\}+\varsigma \tag{3-6}$$

According to Table 3-1, the maximum roll angular body velocity, A_η gradually increased with the increasing time (y=74.7x+615.8, r=0.99, at t=0ms until 10ms). A similar trend held for the offsets of fitting responses, ζ_η as its value also continuously increased after perturbation onset (y=105.8x+1356, r=0.96). Compared with the response amplitude and its offset, the coefficient of determination of roll angular motion, R_η^2 significantly decreased with the increasing time (y=-0.02x+0.57, r=-0.93, r_c=0.18±0.06 is the lowest angular-linear correlation of kinematic parameters of body motion, at t=0ms until 10ms).

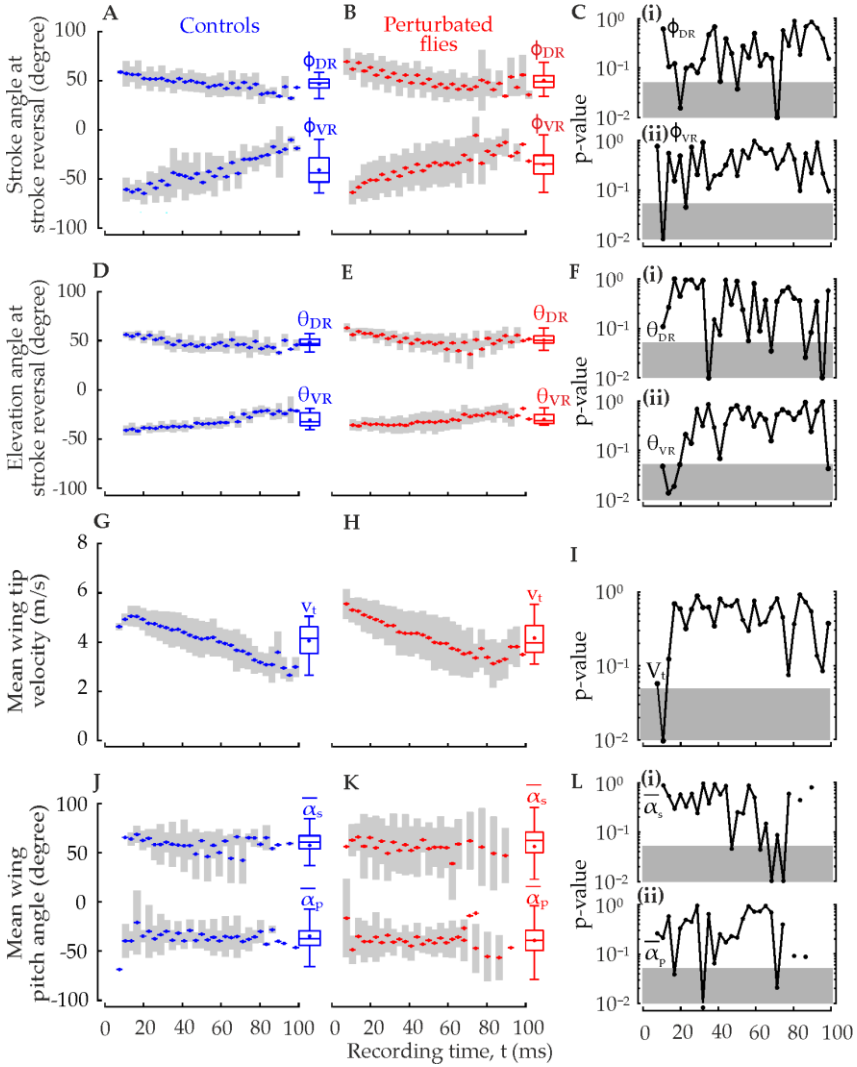

Figure 3-18: Wing kinematics responding to continuous perturbation (middle column, red, N=44 flies) and non-perturbated controls (left column, blue, N=17 flies). (A, B, D, E, G, H, J, K) Time trace of wing (A-B) stroke angle at dorsal stroke reversal and ventral stroke reversal, (D-E) elevation angle at dorsal stroke reversal and ventral stroke reversal, (G-H) strokewise-averaged wingtip velocity and (J-K) strokewise-averaged wing angle of attack. Mean

(dots) and standard deviation (grey bars) were binned to 50% stroke cycle. Inset (boxplots) shows temporal mean, medians and standard deviation. (C, F, I, L) Time traces of statistical comparison (t-test) between perturbated flies and controls. Grey areas represent the p-value less than 0.05.

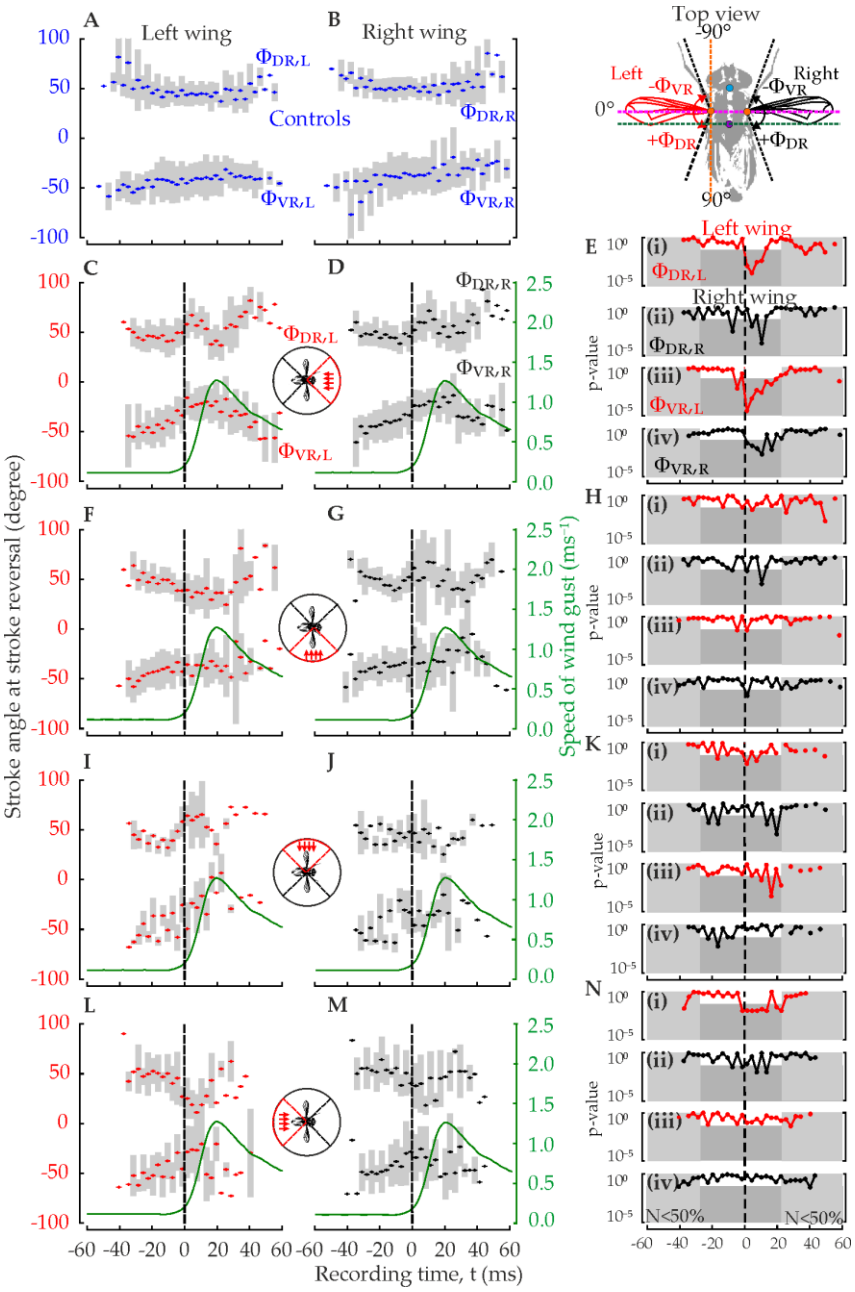
A
Left wing
B
Right wing
Controls
C
D
F
G
I
J
L
M
Top view
-90°
Left
Right
0°
90°
E
Left wing
Right wing
H
K
N
p-value
N<50%
Stroke angle at stroke reversal (degree)
Speed of wind gust (ms⁻¹)
Recording time, t (ms)

Figure 3-19: Wing stroke angles at dorsal and ventral stroke reversal during impulsive perturbation (red for the left wing and black for the right wing, all N=89 flies) and non-perturbated controls (blue, N=32 flies). (Left and middle column) Time trace of means (dots) and standard deviations (grey area) binned to 50% stroke cycle, before ($t<0$ms) and during ($t\geq0$ms) perturbation from anterior (N=37 flies), right lateral (N=31 flies), left lateral (N=10 flies) and posterior (N=11 flies). Red arrows in the schematic diagrams show flow direction at perturbation onset. Green trace shows mean speed of the wind gust (right scale). (E, H, K, N) Statistical comparison (t-test) between perturbated flies and controls. Time trace of instantaneous p-values during dorsal DR (i, ii) and ventral VR (iii, iv) stroke reversal. Dark grey areas represent the p-value less than 0.05. Light grey areas represent time traces with less than 50% total number of animals. Vertical dotted line in C-N indicates perturbation onsets. All positive wing stroke angles are indicated at the dorsal part of the body.

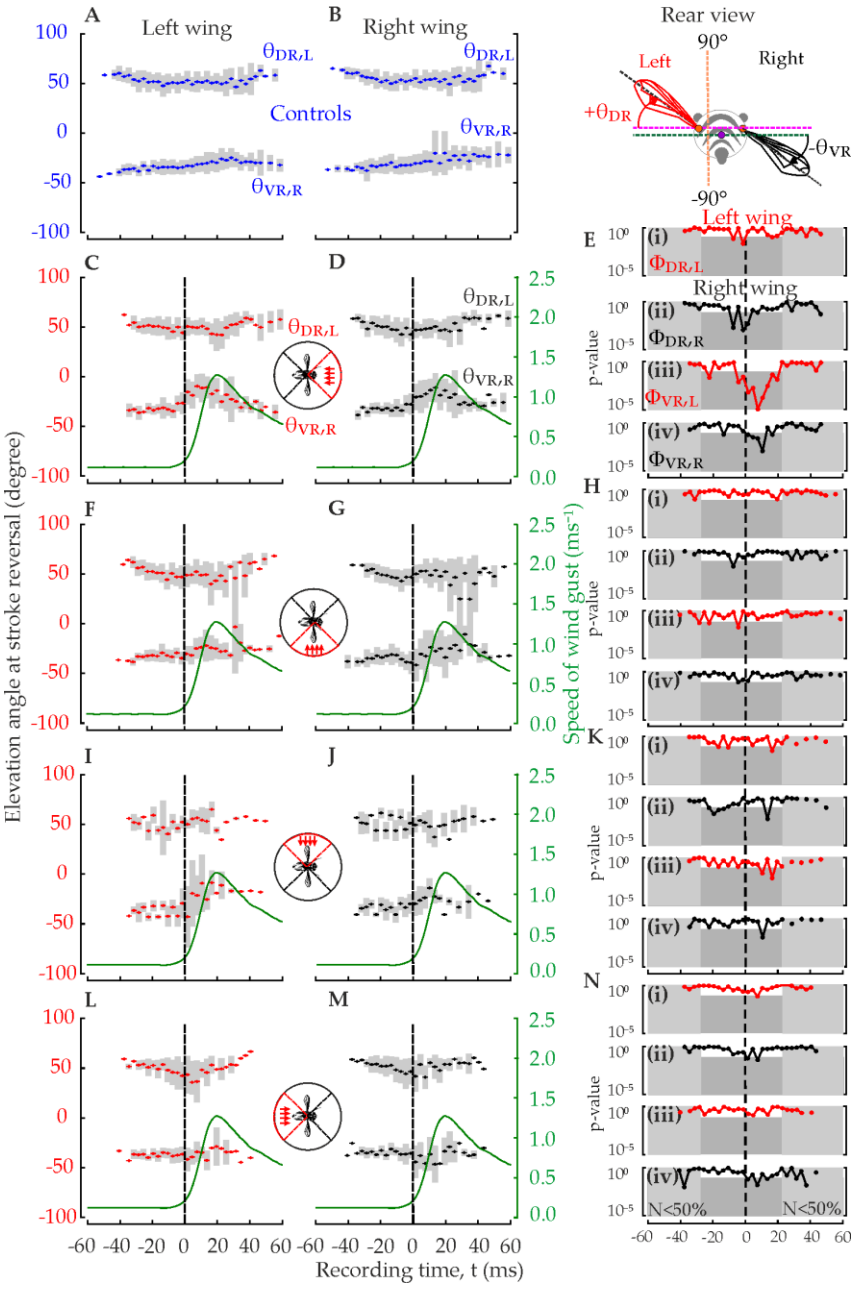
A
Left wing
B
Right wing
Controls
C
D
E
Left wing
Right wing
F
G
H
I
J
K
L
M
N
Rear view
90°
Left
Right
-90°
Elevation angle at stroke reversal (degree)
Speed of wind gust (ms⁻¹)
p-value
N<50%
Recording time, t (ms)

Figure 3-20: Wing elevation angles at dorsal and ventral stroke reversal during impulsive perturbation (red for the left wing and black for the right wing) and non-perturbated controls (blue). (Left and middle column) Time trace of means (dots) and standard deviations (grey area) binned to 50% stroke cycle, before ($t<0$ms) and during ($t\geq0$ms) perturbation from anterior, right lateral, left lateral and posterior. (E, H, K, N) Statistical comparison (t-test) between perturbated flies and controls. Time trace of instantaneous p-values during dorsal DR (i, ii) and ventral VR (iii, iv) stroke reversal. All positive wing elevation angles are indicated at the dorsal part of the body. See previous figure legend, Figure 3-19.

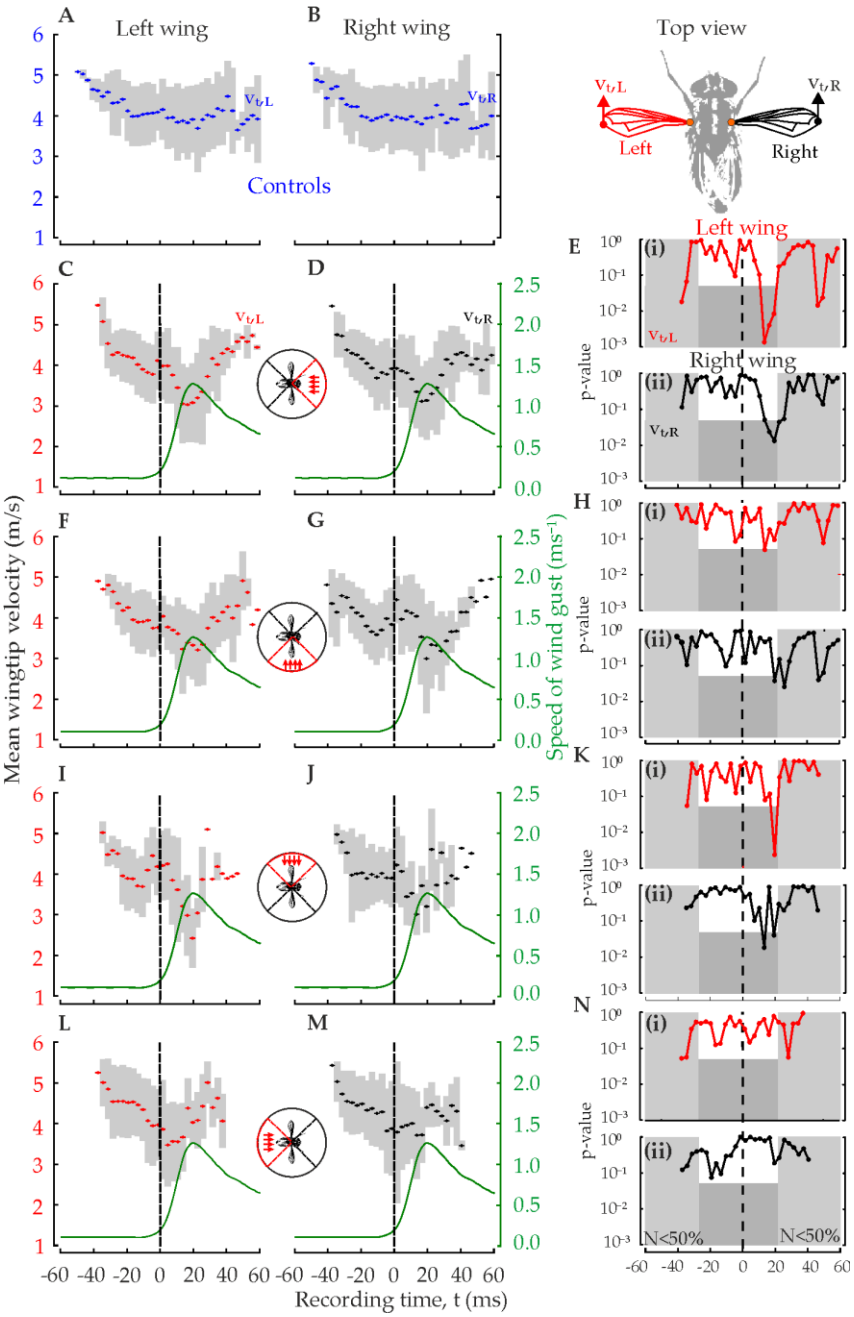
A
Left wing
B
Right wing
Controls
Top view
Left
Right
C
D
E
F
G
H
I
J
K
L
M
N
Left wing
Right wing
(i)
(ii)
p-value
Mean wingtip velocity (m/s)
Speed of wind gust (ms⁻¹)
N<50%
N<50%
Recording time, t (ms)

Figure 3-21: Strokewise-averaged wingtip velocities during impulsive perturbation (red for the left wing and black for the right wing) and non-perturbated controls (blue). (Left and middle column) Time trace of means (dots) and standard deviations (grey area) binned to 50% stroke cycle, before ($t<0$ms) and during ($t\geq0$ms) perturbation from anterior, right lateral, left lateral and posterior. (E, H, K, N) Time trace of instantaneous p-values calculated from statistical comparison (t-test) between perturbated flies and controls. See previous figure legend, Figure 3-19.

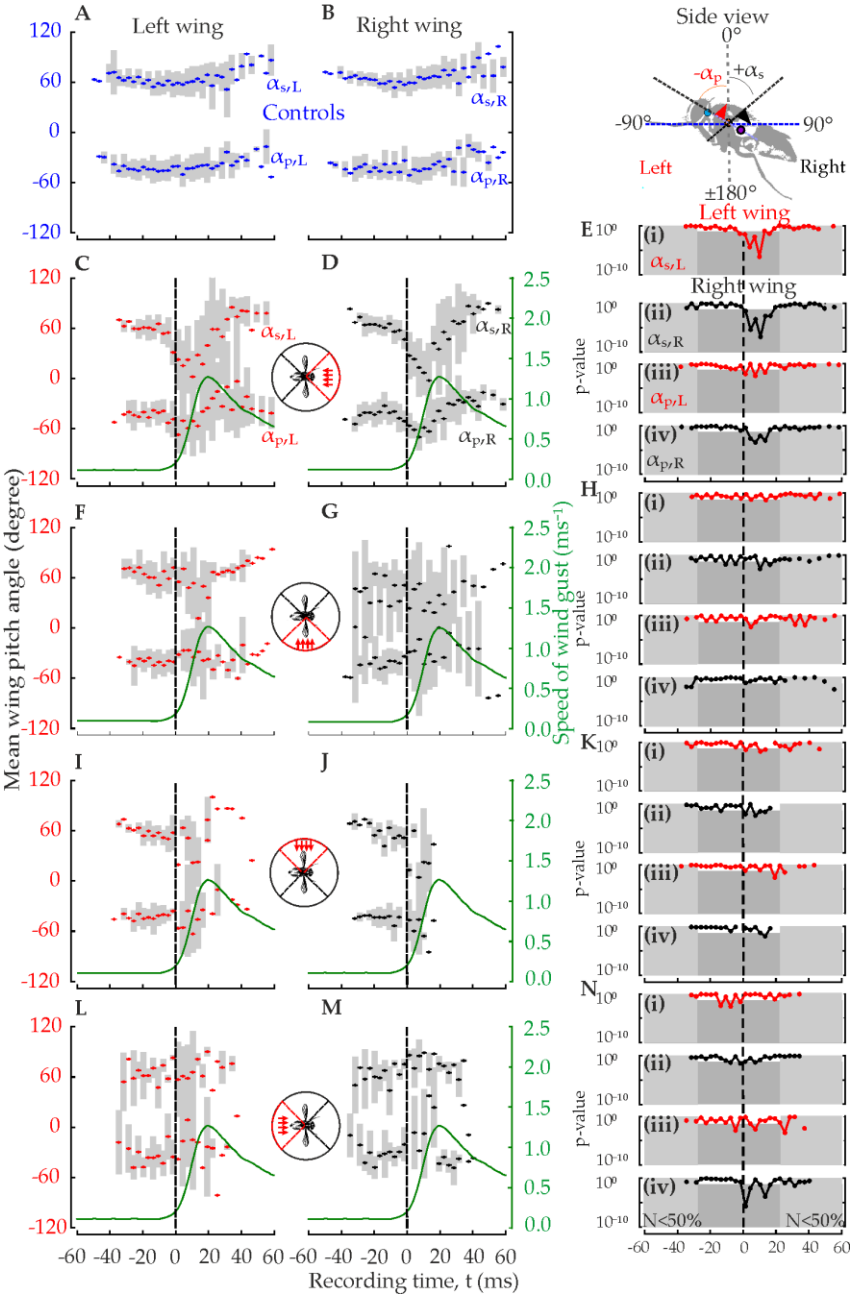
A
Left wing
B
Right wing
Controls
C
D
E
Left wing
Right wing
F
G
H
I
J
K
L
M
N
Side view
Left
Right
±180°
Mean wing pitch angle (degree)
Speed of wind gust (ms⁻¹)
p-value
N<50%
Recording time, t (ms)

Figure 3-22: Strokewise-averaged wing angle of attacks during impulsive perturbation (red for the left wing and black for the right wing) and non-perturbated controls (blue). (Left and middle column) Time trace of means (dots) and standard deviations (grey area) binned to 50% stroke cycle, before ($t<0$ms) and during ($t\geq0$ms) perturbation from anterior, right lateral, left lateral and posterior. Leading wing edge is indicated by a triangle attach on ventral surfaces. (E, H, K, N) Statistical comparison (t-test) between perturbated flies and controls. Time trace of instantaneous p-values during supination (i, ii) and pronation (iii, iv). All positive wing angle of attacks indicate supination. See previous figure legend, Figure 3-19.

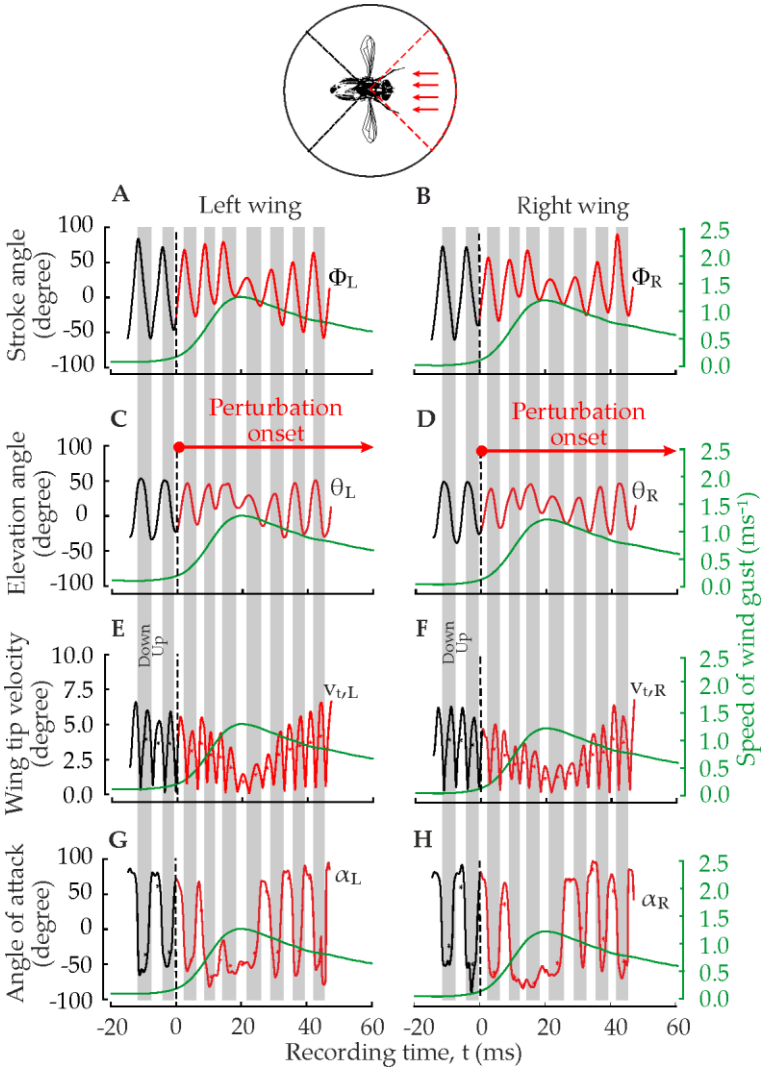

Figure 3-23: Wing kinematics of a single fly responding to an impulsive perturbation from anterior. Time traces of (left column) the left wing and (right column) the right wing (A-B) stroke angle, (C-D) elevation angle, (E-F) tip velocity and (G-H) angle of attack before ($t<0$ms, black) and during ($t\geq0$ms, red) perturbations. Asterisk represents the mean value in each half stroke cycle. Red arrows in the schematic diagrams show flow direction at perturbation onset. Vertical dotted line in indicates perturbation onsets. Green trace

shows mean speed of the wind gust (right scale). Grey areas indicate the downstroke.

3-5. Wing kinematics during take-off

To describe the flies' transient responses of wing motion during perturbation, I determined the wing kinematic parameters for left and right wing as defined in Figure 2-12 which includes amplitude (Φ) and stroke frequency or wingtip velocity ($v_{w,t}$) relative to thoracic structure (Ennos, 1989; Götz, 1987; Lehmann and Dickinson, 1998; Zanker, 1990). I also introduced additional two parameters, which are wing elevation angle (θ) and wing angle of attack (α).

3-5-1. Controls

Non-perturbated flies, mostly performed flight at a wingbeat amplitude of 84.5±3.4° (46±3.4° stroke angle at dorsal reversal and -38.4±3.8° stroke angle at ventral reversal, Figure 3-19A, B) and mean wing elevation amplitude of 80.2±5.1° (51.5±1.8° elevation angle at dorsal reversal, -28.7±4.4° elevation angle at ventral reversal, Figure 3-20A, B). Strokewise-averaged wingtip velocity was 3.9±0.1ms^{-1} (Figure 3-21A, B) and strokewise-averaged wing angle of attack 63±5.4° during upstroke and -41.6±6° during the downstroke (Figure 3-22A, B).

3-5-2. Wingbeat amplitude

3-5-2-1. Alterations during continuous perturbation

Under continuous turbulent conditions (Figure 3-18), flies increased mean stroke angle at dorsal reversal (50.2±8.7° versus controls 46±3.4°), but simultaneously decrease the stroke angle at ventral reversal (-35.4±13.6° versus controls -38.4±3.8°). This alteration of stroke angle indicates that flies shifted their wing stroke backwards while keeping wingbeat amplitude similar to controls (85.6±11.2°, ~1% increase compared to controls).

3-5-2-2. Alterations during impulsive perturbations

During impulsive perturbation with a laminar wind gust, flies exhibited series of fast and well-tuned alterations in wing motions depending on the initial body state posture. According to Figure 3-19, after 20ms perturbation onset, as the speed of airflow from anterior reached maximum level, mean wingbeat amplitude is reduced by 28% in the left wing (60.8±17°) and 22% in the right wing (65.8±17.5°) compared to non-perturbated controls (84.5±3.4°). During

stimulation, wingbeat amplitude monotonously decreased with the increasing time (rate of decrease in the left wing -2068±343°s^{-1} at t=4.5 until 10.5ms, correlation analysis between left WBA and time, r=0.88, 6 data points; rate of decrease in the right wing -2040±239°s^{-1} at t=10.5 until 22.5ms, correlation analysis between right WBA and time, r=0.95, 5 data points). Pressure drag presumably shifted both sides of the flies' wingbeat amplitude posteriorly in parallel with the direction of flow and opposed to flight heading (stroke angle at dorsal reversal, 54.15±10.2° compared to controls 46±3.4°; stroke angle at ventral reversal, -22.1±3.5° compared to controls -38.4±3.8°). A further example, during anterior perturbation, a single exemplary fly shifted its ventral stroke reversal backwards, even beyond the transversal body axis (left wing, Φ=2.3° at t=18ms, Figure 3-23A; right wing, Φ=3.7° at t=12ms, Figure 3-23B). Fly also keeps dorsal stroke reversal closer to transversal body axis (left wing, Φ=28.2° at t=21.7ms, right wing, Φ=28.5° at t=21.5ms), which also implied smaller wingbeat amplitude (left wing, WBA=26°, right wing, WBA=30°) for two stroke cycles during recovery.

A similar trend of wing stroke alterations holds for posteriorly perturbated flies, but the stroke planes were shifted anteriorly (in parallel with the flight heading and flow direction) compared to perturbation from anterior (Figure 3-19L, M). Maximum alteration of wingbeat amplitude occurred 8ms after perturbation onset when posteriorly perturbated flies decreased their wingbeat amplitude to 37.8±24° (decreased by 55% compared to controls) in the left wing and 52.3±20° (decreased by 38% compared to controls) in the right wing. During one-third of the period between stimulus onset and peak of perturbation strength, the wing stroke angle at dorsal stroke reversal shifted forward (10.5±17° in the left wing and 18.5±9° in the right wing) compared to controls (46.1±3.4°). Posteriorly perturbated flies also caused a longer period of alteration of dorsal stroke reversal (24ms in the left wing; 21ms in the right wing; t-test, $p<0.05$) compared to other direction of perturbations (anterior perturbation 10.5ms, lateral perturbation 7.5ms; Figure 3-19N-i-ii). By contrast, during perturbation from posterior, ventral stroke reversal has no significant statistical differences (t-test, $p>0.05$, Figure 3-19N-iii, iv).

Laterally perturbated flies, however, altered their stroke angle even before perturbation onset t<0, presumably owing to the fact that stimulus reached the wings first before body (left laterally perturbated flies, t=-22.5ms prior perturbation, right wing dorsal and ventral stroke reversals, Figure 3-19Kii-iv).

3-5-3. Wing elevation angle

3-5-3-1. Alterations during continuous perturbation

Under turbulent conditions, flies reduced wing elevation angle at both dorsal (50.6±5.8° versus controls, 51.5±1.8°) and ventral stroke reversals (-30±5° versus controls, -28.7±4.4°). However, mean elevation amplitude (79.3±5.8°) is similar to non-perturbated controls (80.2±5.1°, 1.6% increases, Figure 3-18D-E). Within 100ms of recording time, 13% of the wing elevation at stroke reversal in left and right wing during continuous perturbation were significantly different compared with controls (t-test, instantaneous $p<0.05$, Figure 3-18F).

3-5-3-2. Alterations during impulsive perturbations

Under impulsive stimulus condition, anteriorly perturbated flies experienced significant adjustments in wing elevation angle (Figure 3-20C-D) compared to perturbations from lateral and posterior (Figure 3-20F-N). At 20ms after perturbation onset, anteriorly perturbated flies decreased the left and right wing elevation amplitude by 30.5% (56±13.8°) and 27.3% (58.6±11°) respectively, compared to non-perturbated controls (80.2±5.1°). Anteriorly perturbated flies also aligned the wing flapping motions closer to longitudinal body axis (stroke angle at dorsal reversal 41.64±15.6°, decreased by 19.2% in the left wing and 43.08±15.73°, decreased by 16.4% in the right wing versus controls, 51.5±1.8°; stroke angle at ventral reversal, -11.35±10.26°, decreased by 60.5% in the left wing and -9.01±12.41°, decreased by 68.6% in the right wing versus controls, -28.7±4.4°). Furthermore, the alteration of wing elevation during anterior perturbation began before stimulus onset (mean t=-1.5ms for both left wing elevation at ventral reversal and right wing elevation at dorsal reversal, t-test, $p<0.05$, Figure 3-20Eii-iii), presumably due to early detection of antennae or sensillae campaniform during ventral stroke reversal before the airflow reached body center of gravity.

According to a single exemplary fly during perturbation from anterior (Figure 3-23C-D), the smallest wing elevation amplitudes were 18.2° for the left wing (elevation angle at ventral reversal of 11.5° at t=18.5ms; elevation angle at dorsal reversal of 29.8° at t=21.7ms) and 24.5° for the right wing (elevation angle at ventral reversal of 4.7° at t=18.3ms; elevation angle at dorsal reversal of 29.3° at t=21.5ms), respectively.

3-5-4. Wingtip velocity

3-5-4-1. Alterations during continuous perturbation

Under continuous turbulent conditions, strokewise-averaged wingtip velocity increases by 6.6% (4.16±0.7ms^{-1} versus controls, 3.9±0.1ms^{-1}). However, this alteration was statistically insignificant (instantaneous p-values>0.05; t-test, Figure 3-18H) compared to non-perturbated controls. Comparing both tested flies and non-perturbated controls, since take-off at t=0ms (during predominant vertical flight) until t=100ms (during predominant horizontal flight), the decrease of strokewise-averaged wingtip velocities over time were nearly similar (linear regression, $y=-23.12x+5.38$, R^2=0.94 for continuously perturbated flies compared to controls, $y=-24.40x+5.33$, R^2=0.88) and not significantly different (ANCONA and test for homogeneity of regressions, F=0.43, p=0.51).

3-5-4-2. Alterations during impulsive perturbations

In contrast to turbulent perturbation, impulsive perturbated flies employed substantial adjustments in their strokewise-averaged wingtip velocity (Figure 3-21C-D). Comparing wing stroke and elevation angle, the alteration of strokewise-averaged wingtip velocity always occurred after the stimulus onset (t>0, Figure 3-21E, H, K).

I conducted the statistical analysis of strokewise-averaged wingtip velocities of anteriorly perturbated flies with controls, and found that 17.7% of the flight period were significantly different (t=13.5 until 19.5ms in the left wing and t=16.5 until 22.5ms in the right wing, t-test, p<0.05, Figure 3-21E). Immediately after the stimulus onset at t=0ms until 22.5ms, anteriorly perturbated flies gradually decreased their strokewise-averaged wingtip velocities (rate of decrease -50±10.5ms^{-2} in the left wing and -41.2±7.6ms^{-2} in the right wing; correlation analysis between wingtip velocity and time r_{left}=0.75 and r_{right}=0.8, all 8 strokewise-averaged data points). At maximum alteration, the left and right wingtip velocities of anteriorly perturbated flies decreased up to 20.5% (3.1±0.9ms^{-1}) compared to non-perturbated controls (3.9±0.1ms^{-1}). The decrease of strokewise-averaged wingtip velocities then recovered 16.5ms after the stimulus onset and gradually increased (rate of increase 56.4±5ms^{-2} in the left wing at t=16.5ms until 48.5ms; 57±5.2ms^{-2} in the right wing at t=16.5ms until 40.5ms). Thus, both sides of wingtip velocities reverted to the previous flapping condition.

A similar trend again demonstrated by a single exemplary fly during anterior perturbation, the wingtip velocities hit the lowest value of 1.4-1.9ms^{-1} after 20ms perturbation onset (rate of decline -153±34.3ms^{-2} in the left wing and -118.8±17.8ms^{-2} in the right wing, correlation analysis between wingtip velocity and time, r_{left}=0.8 and r_{right}=0.9, 6 strokewise-averaged data points, Figure 3-23E-F). The decrease of strokewise-averaged wingtip velocities were then recovered and gradually increased to earlier condition before perturbation onset (rate of increase 140±9.6ms^{-2} in the left wing and 128.2±12.71ms^{-2} in the right wing, correlation analysis between wingtip velocity and time, r_{left}=0.97 and r_{right}=0.94, 8 strokewise-averaged data points, Figure 3-23E-F).

By contrast, lateral wind gust also caused alteration of strokewise-averaged wingtip velocities, but flies managed to quickly reverted to non-perturbated flapping condition (t=13.5ms for lift wings and t=19.5ms in right wing, t-test, p<0.05, Figure 3-21H, Ki-ii). In another case of posteriorly perturbated flies, strokewise-averaged wingtip velocities had little changes and statistically insignificant (left wing 3.49±1ms^{-1} decreased by 10%; right wing 3.73±1.1ms^{-1} decreased by 5% compared to controls 3.9±0.1ms^{-1}; Figure 3-21N-i, ii).

3-5-5. Wing angle of attack

3-5-5-1. Alterations during continuous perturbation

Under continuous turbulent conditions, tested flies had a strokewise-averaged wing angle of attack of -34.8±15.7° during downstroke (16% decrease compared to controls -41.6±6°) and 57.4±17.5° during upstroke (8.8% decrease compared to controls 63±5.4°, Figure 3-18). Further statistical comparison of instantaneous strokewise-averaged wing angle of attack reveal that 16% of the flight period during upstroke (t=16.67ms, 31.8ms, 71.2ms; t-test, p<0.05, Figure 3-18Li) and 12% during downstroke (t=47ms, 62.1ms, 68.1ms, 74.2ms, Figure 3-18Lii) were significantly different compared to non-perturbated controls, respectively.

3-5-5-2. Alterations during impulsive perturbations

During upstroke, anteriorly perturbated flies altered their strokewise-averaged wing angle of attack up to 18ms (t=-1.5 until 16.5ms, Figure 3-22E-i, ii). Comparing both statistical comparisons of anteriorly perturbated flies and non-perturbated flies, I found 35.3% of the instantaneous p-values of t-test were below 0.05, which indicates significance differences compared to controls. During anterior perturbation, the maximum alteration of wing angle of attack occurred at t=12ms after perturbation onset. At maximum alteration, the mean

wing angle of attacks decreased up to 97% in the left wing (2±30.4°, t=10.5ms) and 104% in the right wing (-2.8±44.8°, t=13.5ms) during upstroke compared to non-perturbated controls (63±5.4°). On the other hand, during the downstroke, the mean wing angle of attacks also decreased up to 37% in the left wing (-57±16.4°, t=13.5ms) and 54% (-64±14°, t=13.5ms) in the right wing compared to non-perturbated controls (-41.6±6°). Referring to an exemplary flight sequence during perturbation from anterior (Figure 3-23G-H), 2 stroke cycles after stimulus onset, the data shown that tested fly sustained relatively small amplitude of wingbeat with pronation configuration (left wing, -50.3±12.4°; right wing, -66.7±12.6°), which presumably minimized pressure drag during perturbation but coincidently produced sufficient amount of elevated lift.

By contrast, during lateral perturbation, tested flies employed faster recovery of strokewise-averaged wing angle of attacks compared to other cases before gradually reverted to previous non-perturbated flapping condition (t-test, $p<0.05$; t=13.5ms, right wing, pronation, Figure 3-22K-iv; t=19.5ms, left wing during downstroke, Figure 3-22K-iii; t=13.5ms, left wing during upstroke, Figure 3-22H-i). Meanwhile, the earliest alteration of strokewise-averaged angle of attacks occurred during posterior perturbation (t=-13.5ms, left wing during the upstroke, Figure 3-22N-ii; t=-4.5ms, left wing during the downstroke, Figure 3-22N-iii; t=1.5ms, right wing during the downstroke, Figure 3-22N-iv).

3-6. Wing kinematics in tethered flies with reduced sensory feedback

To study the significance of highly-sensitive sensory receptors during aerodynamic perturbations, I conducted a series of experiments in which sensory feedback was manipulated (see Chapter 2-1-3 and Chapter 2-1-4). There are two fast mechanosensory receptors which are halteres for measurement of body rotation and antennae for flow detection. In these experiments, I used impulsive perturbation of laminar airflow from anterior (0°) and posterior (180°). I then compared the instantaneous mean wingtip velocity (mean±s.d.) of tethered flies under different conditions of sensory treatments as listed in Table 2-3. In free-flight experiments, I am not able to record longer than 20ms of recording time after perturbation onset. Therefore, experiments with tethered flies that placed inside the cameras' ROI allowed me to study the flies' behavioural responses, especially wing kinematics for a longer period (60ms after perturbation onset, 120ms of complete recording time). Changes of adaptive wing motions presumably are not only initiated by active sensory detections, but it can also be caused by passive wing drag, which remains to be explained.

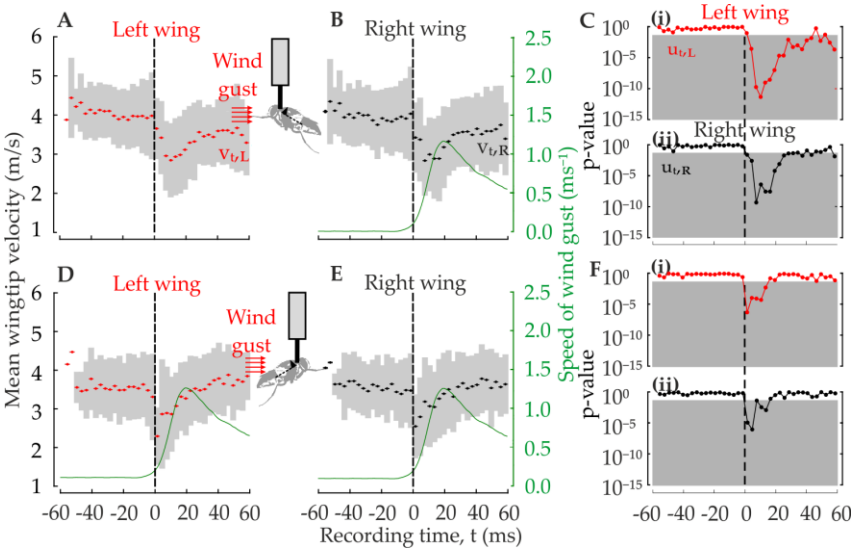

Figure 3-24: Strokewise-averaged wingtip velocities of tethered flies facing impulsive perturbation (red for the left wing and black for the right wing) from anterior (A-C, N=29 flies) and posterior (D-F, N=27 flies). (Left and middle column) Time trace of means (dots) and standard deviations (grey area) binned to 50% stroke cycle, before (t<0ms) and during (t≥0ms) perturbation. Red arrows show the direction of the oncoming perturbation. Green trace (right scale) shows mean speed of the wind gust. (C, F) Time trace of instantaneous p-values calculated from statistical comparison (t-test) between perturbated flies and controls. Grey areas represent p-value less than 0.05. Vertical dotted line indicates perturbation onsets. Light grey areas represent time traces with less than 50% total number of animals.

3-6-1. Wingtip alteration of tethered flies

During anterior perturbation, tethered flies initially decreased strokewise-averaged wingtip velocities faster (rate of decrease -98.9±8.8ms^{-2} in the left wing and -121.9±24.7ms^{-2} in the right wing, correlation analysis between wingtip velocity and time r_{left}=0.97 r_{right}=0.88, Figure 3-24A, B) than intact flies (freely-flying flies during anterior perturbation; left wing, -50±10.5ms^{-2}; right wing, -41.2±7.6ms^{-2}, Figure 3-21C, D). Flies decreased wingtip velocities up to 23% (left wing, 3±0.87ms^{-1}, t=10.5ms) and 26% (right wing, 2.9±0.9ms^{-1}, t=7.5ms), which is similar to intact flies (freely-flying flies during anterior perturbation,

3.1±0.9ms^{-1}, t=20ms, 20.5% of decrease). After this initial response, anteriorly perturbated flies then reverted to the previous non-perturbated flapping condition by steadily increased their wingtip velocities (rate of increase 34.4±3.6ms^{-2} in the left wing and 34.5±4.56ms^{-2} in the right wing, correlation analysis between wingtip velocity and time r_{left}=0.93 r_{right}=0.88, all with 8 strokewise-averaged data points).

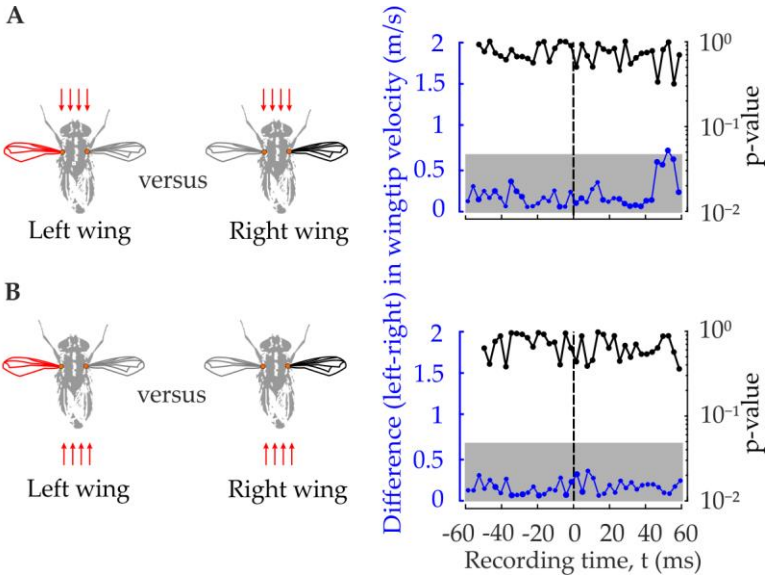

Figure 3-25: Differences in strokewise-averaged wingtip velocities of left (red) and right (black) wings in tethered flies facing impulsive perturbations from anterior (A, N=29 flies) and posterior (B, N=27 flies). (Right column) Time trace of instantaneous p-values calculated from statistical comparison (t-test) between perturbated flies and controls (black, right axes). See previous figure legend, Figure 3-24.

A comparable trend holds for flies facing perturbation from the posterior. However, tested flies decreased their wingtip velocity immediately after perturbation onset. Mean strokewise-averaged wingtip velocities hit the minimum of 2.3±0.72ms^{-1} in the left wing and 2.57±0.81ms^{-1} in the right wing, which is relatively lower compared to anteriorly perturbated flies (left wing, 2.96±0.87ms^{-1}; right wing, 2.86±0.88ms^{-1}, Figure 3-24D, E). After that, posteriorly perturbated flies increased their wingtip velocities and fully reverted to previous non-perturbated wing velocities at t=16.5ms (rate of increase 54.2±13ms^{-2} in the

left wing and 40.1±12.7ms^{-2} in the right wing, correlation analysis between wingtip velocity and time r_{left}=0.90 r_{right}=0.84, all with 6 strokewise-averaged data points). The increases of mean wingtip velocities are faster by 57.5% in the left wing and 16.2% in the right wing than those measured in anteriorly perturbated flies (rate of increase 34.4±3.6ms^{-2} in the left wing and 34.5±4.56ms^{-2} in the right wing).

To score temporal deviation of wings' motions, I estimated left-minus-right differences of velocities between left and right wings (Figure 3-25). Any difference of velocities between left and right wing during perturbation indicates that flies vary their yaw torque for turning manoeuvres. By contrast, zero temporal deviation in wing velocity with symmetry and no subtle differences in stroke kinematics between left and the right wing will elevate flies upward. The difference of wingtip velocity between left and right wing of tethered flies during anterior and posterior perturbation is negligibly small (left wing 0.91±0.21ms^{-1}; right wing 0.13±0.08ms^{-1}, N=20 data points). The statistical comparison also confirmed that left-right wingtip velocity for the entire recording time was not significantly different (t-test, $p>0.05$).

3-6-2. Wingtip alteration of flies with immobilised antennae

In this experiment, I glued all three segments of the left and right antennae including the arista of tethered flies (as previously mentioned in Chapter 2-1-4), in order to study the importance of antennae as a wind sensor. Immobilised antennae may cause severe disruption or deficiency of flies' ability to regulate flight during aerial perturbation (Fuller et al., 2014b; Sane et al., 2007; Yorozu et al., 2009). Therefore, the only remaining sensory input left used to sense air current is through flexion of campaniform sensillae or bristles, which are spatially distributed across body surfaces and along the leading edge of wings.

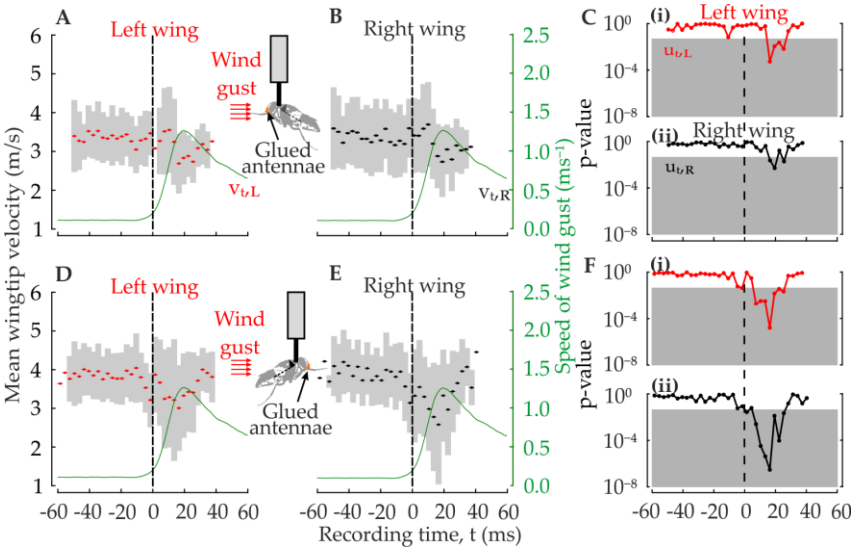

Figure 3-26: Strokewise-averaged wingtip velocities of tethered flies with immobilised antennae facing impulsive perturbation (red for the left wing, black for the right wing) from anterior (A-C, N=17 flies) and posterior (D-F, N=19 flies). (Left and middle column) Time trace of means (dots) and standard deviations (grey area) binned to 50% stroke cycle, before (t<0ms) and during (t≥0ms) perturbation. Red arrows show the direction of the oncoming perturbation. Green trace shows mean speed of the wind gust (right scale). (C, F) Time trace of instantaneous p-values calculated from statistical comparison (t-test) between perturbated flies and controls. Grey areas represent p-value less than 0.05. Vertical dotted line indicates perturbation onsets. Light grey areas represent time traces with less than 50% total number of animals.

In tethered flies with reduced antennal feedback signal, the alteration of strokewise-averaged wingtip velocities during anterior perturbation were delayed with respect to the stimulus onset by 16.5ms for both wings compared to intact flies (t-test, $p<0.05$, Figure 3-26C). The minimum strokewise-averaged wingtip velocity of anteriorly perturbated flies were 2.55±0.75ms^{-1} in the left wing at t=16.5ms (rate of decrease=-20ms^{-2}, Figure 3-26A) and 2.69±0.9ms^{-1} in the right wing at t=19.5ms (rate of decrease=-78ms^{-2}, Figure 3-26B). After the initial response, anteriorly perturbated flies regained their non-perturbated flapping condition within 9ms (rate of increase 35.38±14.1ms^{-2} in the left wing and

16.71±8.5ms^{-2} in the right wing) before reverting back to non-perturbated strokewise-averaged wingtip velocity.

Flies facing posterior airflow perturbation altered both strokewise-averaged wingtip velocities slightly faster compared to anteriorly perturbated flies (t=7.5ms after the stimulus onset t-test, $p<0.05$, Figure 3-26F). At t=16.5ms, posteriorly perturbated flies hit the minimum strokewise-averaged wingtip velocity 3±11ms^{-1} in the left wing (rate of decrease=-45.15±13ms^{-2}) and 2.57±1.5ms^{-1} in the right wing (rate of decrease=-82.14±4.3ms^{-2}). Comparable to the anteriorly perturbated flies, flies facing perturbation from posterior shown longer alteration period of 18.5ms (9ms during anterior perturbation, t-test, $p<0.05$, Figure 3-26F).

3-6-3. Wing kinematics of tethered flies responding to changes in wind gust average airspeed

To explore the link between wing kinematic alterations and changes in impulsive perturbation strength, I measured the wingtip velocities of tethered flies at different airspeed.

Alteration in strokewise-averaged wingtip velocity occurred when flies facing impulsive perturbation strength of 1.1ms^{-1} or higher (Figure 3-27). For example, 1.2ms^{-1} of impulsive wind gust average airspeed decreased the strokewise-averaged wingtip velocity by 28% for both side of the wings (left wing, rate of decrease=-89.23ms^{-2}, correlation analysis between left wingtip velocity and time r=0.81, $v_{t,min}$=2.78±0.78ms^{-1} at t=10.5ms; right wing, rate of decrease=-83.72ms^{-2}, correlation analysis between right wingtip velocity and time r=0.74, $v_{t,min}$=2.81ms^{-1} at t=13.5ms) compared with controls (non-perturbated free flight sequences, strokewise-averaged wingtip velocity 3.9±0.13ms^{-1}, Figure 3-20A, B). After reached the minimum value of strokewise-averaged wingtip velocity, flies facing 1.2ms^{-1} of impulsive wind gust then increased their wingtip velocity and regained previous non-perturbated flapping condition with higher rate of recovery (rate of increase 40±6.67ms^{-2} in the left wing and 55.83±13.23ms^{-2} in the right wing, correlation analysis between wingtip velocity and time r_{left}=0.81and r_{right}=0.74, all with 8 strokewise-averaged data points) compared to other cases (1.1ms^{-1} of impulsive wind gust; rate of increase 28.13±2.9ms^{-2} in the left wing and 22.7±4.4ms^{-2} in the right wing, correlation analysis between wingtip velocity and time r_{left}=0.79 and r_{right}=0.72, all with 10 strokewise-averaged data points).

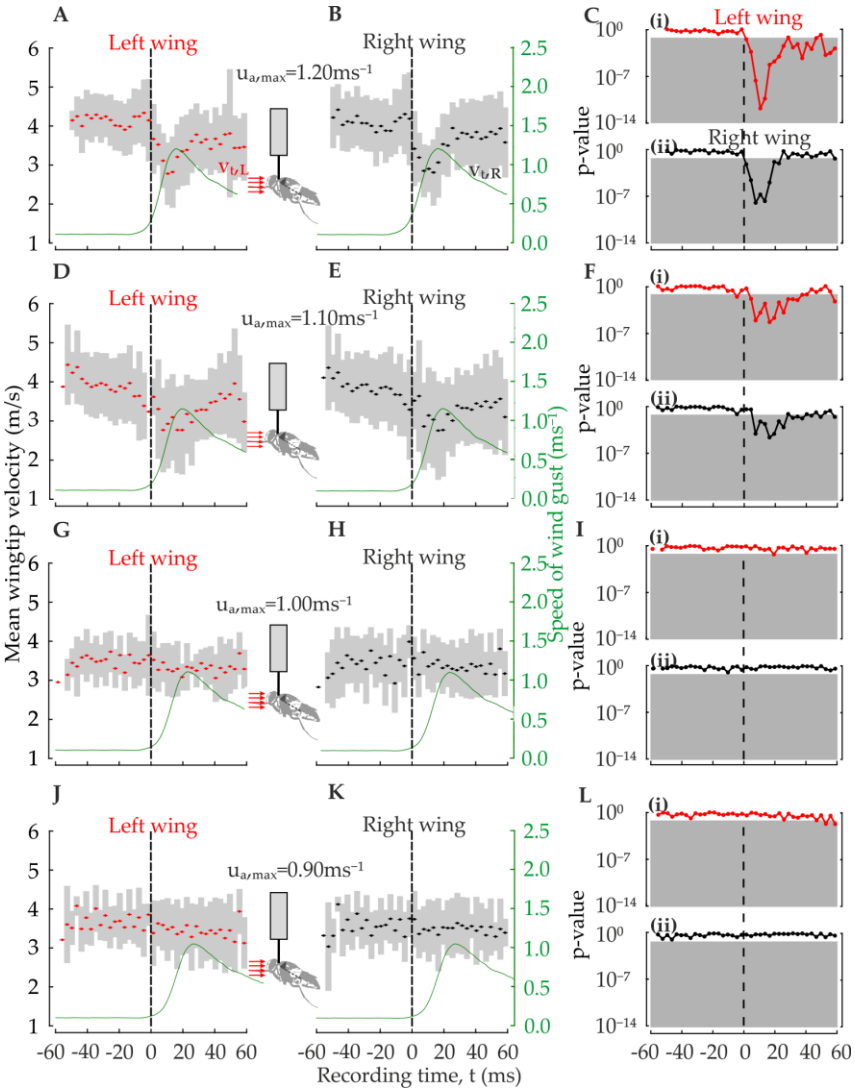

Figure 3-27: Strokewise-averaged wingtip velocities of tethered flies facing to changes in maximum impulsive perturbation strength 1.20ms^{-1} (A-B, N=15 flies), 1.10ms^{-1} (D-E, N=13 flies), 1.00ms^{-1} (G-H, N=7 flies) and 0.90ms^{-1} (J-K, N=8 flies) from anterior (red for the left wing and black for the right wing). (Left and middle column) Time trace of means (dots) and standard deviations (grey area) binned to 50% stroke cycle, before (t<0ms) and during (t≥0ms)

perturbation. (Right column) Time trace of instantaneous p-values calculated from statistical comparison (t-test) between perturbated flies and controls. See previous figure legend, Figure 3-26.

Flies facing 1.1ms^{-1} of impulsive wind gust average airspeed hit the minimum strokewise-averaged wingtip velocities of 2.78±1.08ms^{-1}at t=16.5ms. The rate of decrease was 2.7-fold lower than flies tested in wind gust with perturbation strength of 1.2ms^{-1} (rate of decrease -33.47±5.18ms^{-2} in the left wing and 31.15±6ms^{-2} in the right wing, correlation analysis between wingtip velocity and time r_{left}=0.79 and r_{right}=0.72, all with 10 strokewise-averaged data points, Figure 3-27D, E). The alterations of strokewise-averaged wingtip velocity of flies facing 1.1ms^{-1} of impulsive wind gust average airspeed were delayed with respect to the stimulus onset by 4.5ms in the left wing and 7.5ms in the right wing, compared to flies tested in 1.1ms^{-1} of impulsive wind gust (alteration immediately occurred after stimulus onset, t=0).

By contrast, flies facing impulsive perturbation strengths lower than 1.1ms^{-1} were not affected throughout entire recording time (Figure 3-27G-L). The instantaneous p-value was always above 0.05, which statistically indicates no significant difference compared to non-perturbated controls (t-test, p>0.05).

4. Discussion

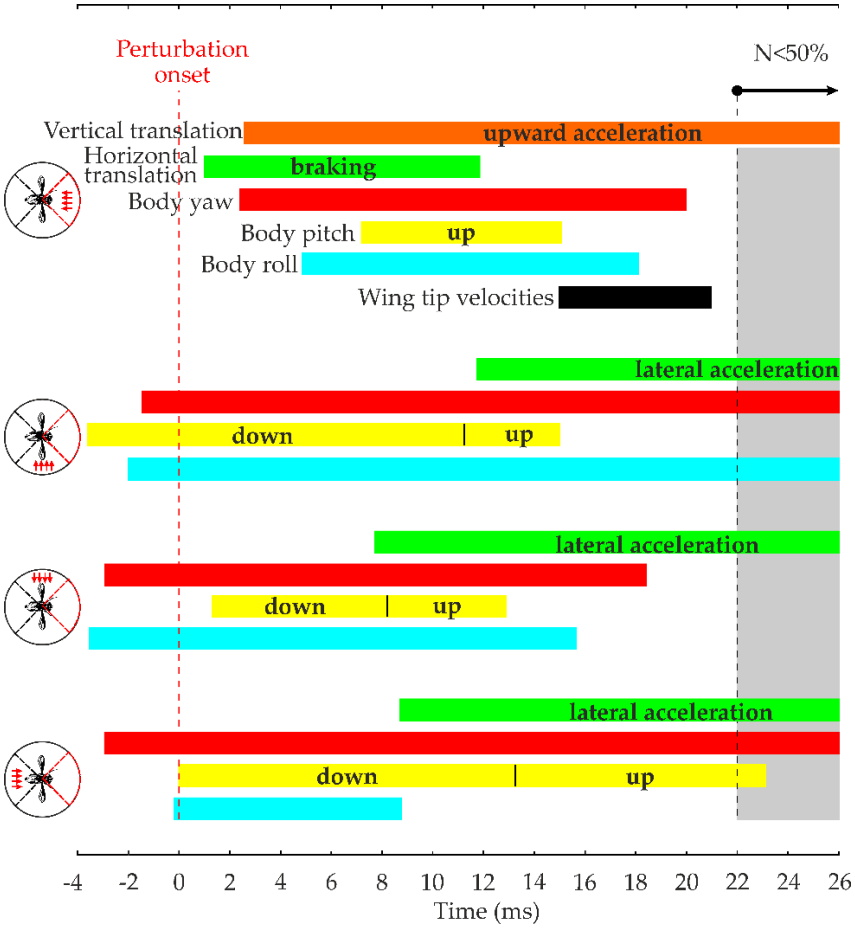

Figure 4-1: Time series of body and wing alterations for houseflies during impulsive perturbation. The alterations of translational and angular body motions are characterized by body vertical translational velocity (orange), horizontal translational velocity (green), yaw (red), pitch (yellow) and roll (cyan). The alterations of wing kinematics are characterized by wing velocities (black). Red arrows in the schematic diagrams show flow direction at perturbation onset. Grey areas represent time traces with less than 50% total number of animals and vertical dotted line indicates perturbation onsets.

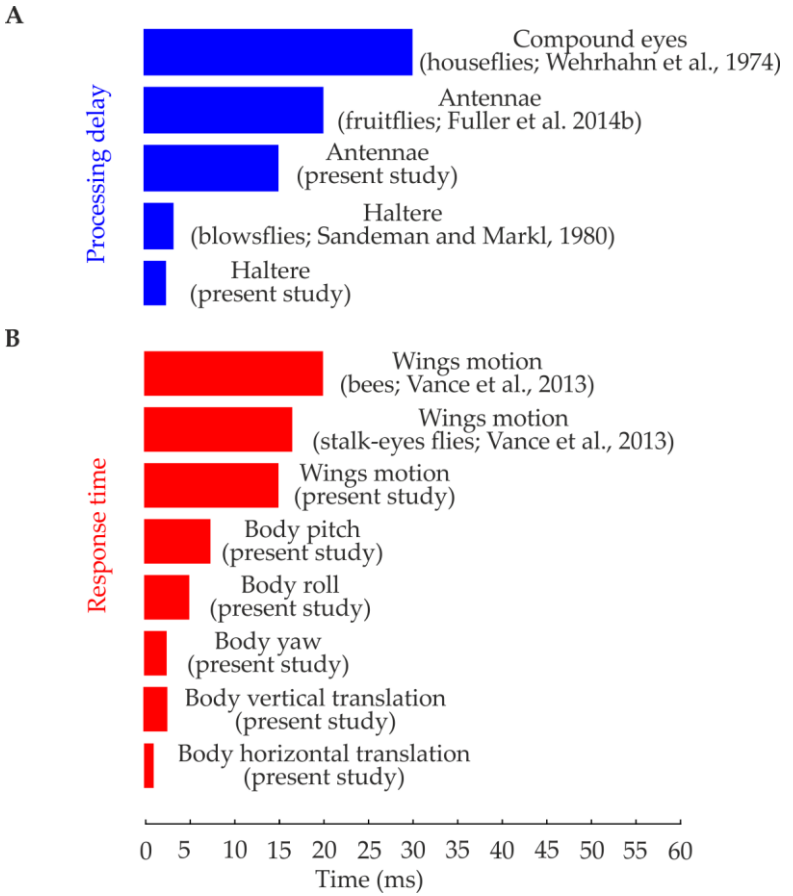

Figure 4-2: (A) Processing delay of housefly's sensory receptors. (B) Response time of body and wing motion during impulsive perturbation from anterior.

The aim of this study is to quantitatively investigate the behavioural responses of houseflies *Musca domestica* during continuous and impulsive aerodynamic perturbation compared to non-perturbated controls. To assess the behavioural effects, I scored the alterations in body and wing kinematics of freely flying and tethered flies (cf. Figure 4-1 for a complete summary of alterations). As described in previous studies, response time is a key indicator used to measure body control during perturbation (cf. Figure 4-2B). As expected from models (Chapter 3-4), data suggest that these alterations are mainly driven by body orientation and flight attitude prior to perturbation and the characteristics of aerodynamics

stimuli. The modulations of wing kinematics have a strong effect on the force production during flight, corroborating earlier studies which indicate that aerodynamic and inertial forces are proportional to cube and square of wing velocity (Ellington, 1984a; Sane and Dickinson, 2002; Walker, 2002). In the following sections, I will discuss these findings in detail including the importance of biological receptors used for flight control (cf. Figure 4-2A for a complete summary).

4-1. On-ground wind sensation and take-off behaviour

Previous studies suggested that the decision to take-off depends on various behavioural and physiological factors [aphids (Dixon and Mercer, 1983); scale insect (Washburn and Washburn, 1984)]. Researchers reported that flies can sense changes of airflow before flies decide to elicit take-off or not, in order to avoid crash during environmental disturbances (Davies, 1936; Digby, 1958; Haine, 1955). For example, at wind speed of 0.54ms^{-1} - 0.67ms^{-1}, small insects such as aphids may lose body control and blown away. At wind speed larger than 1.67ms^{-1}, aphids even do not take-off at all (Haine, 1955). Further studies showed that houseflies refuse to perform take-off under extreme windy conditions and inhibit flight activity to avoid mechanical failure (Digby, 1958; Johnston and Heed, 1976). By contrast, light wind gust is part of the 'catalyst' or an activating effect for locusts to initiate their first aerial activity in the early morning (Kennedy, 1939). Flies first adapt and gradually exploit the changes of the ambient wind. This learning behaviour ensures their upcoming flight routine may minimally be affected (Klassen and Hocking, 1964). Another example, flight activity of *Calliphora* increases with the increasing wind speed up to 0.7ms^{-1} (Digby, 1958). However, during more gusty condition, these flying insect again begin to reduce locomotion activity with longer resting periods preceding take-off (>20minutes of latency).

There are consistencies between the current study and previous works in the field that can be highlighted. The foremost, Figure 3-1 shows that mean take-off latency linearly increase with increasing turbulence strength (linear regression fit, y=13.21x-4, R^2=0.69, p=0.02, N=66 flies). I found that at 0.7ms^{-1} wind speed after flies left the reservoir, they require 4.2±8.2 minutes resting time prior take-off. By contrast, at the average airspeed of turbulent flow lower than 0.7ms^{-1}, the probability for flies to perform take-off is relatively high (grey area, Figure 3-1). To discover the consequences of take-off latency, I then investigate the change of body and wing motions of flies (Chapter 3-3 and Chapter 3-5), which successfully take-off inside this moderate turbulence strength. Indeed, these experiments confirmed that short resting and temporary on-ground adaptation

diminish significant body alteration during moderate continuous turbulent flow (vertical and horizontal velocity, yaw angular velocity; t-test, all instantaneous $p>0.05$). The alterations in pitch and roll angular velocities are however relatively short in time due to only 7.3% of instantaneous p-values for pitch angular velocity and 9% for roll angular velocity were below 0.05 within 100ms flight period (statistical comparison of instantaneous angular velocities, t-test).

In order to sustain a stable flight, flies actively altered their wing kinematics variables compared to non-perturbated controls (stroke plane shifted 3-4° backward, 6.6% increase of wingtip velocity, 13%-16% of instantaneous p-values for wing elevation at stroke reversal and pitch angle lies below 0.05). These moderate wing kinematics adjustments during external perturbation presumably contribute to the inhibition of body alterations.

There is a limitation of aerial locomotor capacities under turbulent condition. As turbulence strength increased, flies unequivocally refused to take-off and demonstrated locomotion suppression on the platform (>30minutes of latency), which is similar to what had been found in previous experiments (Yorozu et al., 2009).

4-2. Body motion

Previous data have already shown that ambient flows are used for dispersion of animals (Chapman et al., 2011; Dudley, 2002; Koehl and Reidenbach, 2007). However, this activity still involves a considerable amount of energy expenditures owing to inertia and aerodynamic force production. Although with small camera's ROI, my data confirmed the earlier findings that turbulent environments induced 1.5-fold broader volume of positional variance compared to non-perturbated controls (Figure 3-2). Despite the average flight trajectories of continuously perturbated flies are not statistically different from controls, the variance of mean body position increased in time (2.2-fold higher rate of increase compared to controls after 50ms take-off; Figure 3-2G). Impulsive perturbation also changes the distribution of flies inside the ROI compared to controls, mainly on the horizontal positional variance (Δ_x=1.4mm, Δ_y=2mm versus Δ_z=1.1mm).

Previous data showed that changes in body position are mediate by passive drifting or wind displacement (Dudley, 2002). Other researchers offer contradictory findings and arguments. After take-off, flies actively regulate and control their body motion, which subjected to various behavioural and physiological influences (Dixon and Mercer, 1983; Washburn and Washburn, 1984). "Response time" is an important indicator used to measure how quick flies

regain their body posture after being perturbated (Beatus et al., 2015). Previous work found that mechanically perturbated flies from lateral direction require not more than 60ms to recover from "aerial stumble" (Ristroph et al., 2010). In the present study, flies facing the same direction of impulsive aerodynamic perturbation encountered shorter alteration period (19ms from left direction, 29ms from right direction; Figure 3-6 until Figure 3-8) compared to the earlier findings, specifying that characteristics of perturbation might affect flies' agility during flight. Overall, my data also showed that flies perturbated from anterior had the shortest alteration period of body angular velocities compared to other direction of wind gust (8ms for pitch, 13ms for roll and 17.5ms for yaw). The slowest reaction of body yaw occurred at 17.5ms after perturbation onset (3 wing stroke cycles) compared to flies' visual response time of 30ms (Wehrhahn et al., 1974), indicating that flies do not use their compound eyes.

In insect flight, body rotational maneuverability during flight depends on the centre of body mass (Dudley, 2002). These alterations of body angle during aerial perturbation also change the inclination angle of the stroke plane and thus alter the direction of mean forces (Dudley, 2002; Vogel, 1966). To regain previous flight condition, flies reorient this mean aerodynamic force vector and actively generate corrective torque. Therefore, during turbulence, flies will experience continuous body rotational fluctuations compared to non-perturbated controls (Beatus et al., 2015). For example, bees laterally incline their vertical net force, which inherits higher temporal alteration of body roll during upwind turbulence stream (Combes and Dudley, 2009). Under turbulent conditions, my data corroborate the earlier studies that body roll angle was the most unstable and largely affected (18.5-fold increase) compared to pitch (7-fold increase) and yaw (6.4-fold increase). Changes in the standard deviation of body angular velocities as a measure of flight instabilities also indicate that roll is higher than those of pitch and yaw ($760°s^{-1}$ versus $577°s^{-1}$ for yaw and $301°s^{-1}$ for pitch). A similar trend holds during lateral impulsive perturbation whereby my findings reveal that, after perturbation onset, the highest rate of alteration occurred about the roll axis ($176660.5°s^{-2}$) compared to pitch ($71326°s^{-2}$) and yaw ($67780°s^{-2}$). In another study, a massive increase in lateral perturbations strength resulted in bees to crash because they fail to recover from excessive body roll (Combes and Dudley, 2009).

Several studies had shown a strong correlation between flight speed and body angle (David, 1978; Götz, 1968; Vogel, 1966). During forward flight, body drag increase with the increasing body pitch angle (Dudley, 2002; Sun and Xiong, 2005). At lower Reynolds number (varying from $10\text{-}10^3$, see figure 5.3 in (Vogel, 1981), flow is highly viscous, thus skin friction is relatively high compared to

pressure drag (Cheng et al., 2010; Fry et al., 2003; Vogel, 1966). However, previous literature also showed that frictional damping on the body was 100-times smaller than the values estimated on both body and wings (Hesselberg and Lehmann, 2007). As such, these high body and wing drag provide strong frictional damping during perturbation, which passively assists flies in achieving stable, well-controlled flight particularly in body pitch (Ristroph et al., 2013). This study confirms that flies first pitch upward during anterior perturbation (rate of increase 54115°s^{-2} compared to non-perturbated controls, 18377.9°s^{-2}), presumably also due to the body and predominant wing drag. After 15ms of perturbation onset, pitch-up angular velocity reached the maximum value (12ms earlier compared to control), later employed corrective counter pitch-down and finally regained previous flight condition. Accordingly, change in body angle (pitch-down) results in 27.3-30.5% decrease of wing stroke elevation angle during upwind. Apart from wings as a sail-structure, there are other possible high-drag structures like abdomen, limbs, and microstructures that may augment body drag (Berthé and Lehmann, 2015; Camhi, 1970; Nachtigall and Hanauer-Thieser, 1992; Vogel, 1981; Zanker, 1988).

Other than active reorientation of independently moving body parts (e.g. wing kinematics), passive translational and rotational damping also assists the flies to keep upright against flight instabilities (Cheng et al., 2010; Hedrick et al., 2009; Lin et al., 2012). This flapping counter-torque (FCT) which acts in the opposite direction of turning reduces neuromuscular-neurosensory requirements and the need for active braking especially during saccade or unintended body motion induced by perturbation. FCT-induced damping which exists about all the rotation axes is linearly depended on body translational and rotational velocity as well as the flapping frequency of wing motion regardless of the kinematic patterns (Cheng et al., 2010). Flying insects are highly unstable and very sensitive about roll axis compared to pitch and yaw [fruit fly (Beatus et al., 2015; Zhang and Sun, 2010), bees (Combes and Dudley, 2009; Ravi et al., 2013; Vance et al., 2013)]. This means that flying insects are less resistant to fluctuations in roll and translational motion along transversal body axis (Dudley, 2002). Previous computational fluid dynamics simulation showed that roll is unstable because it is induced by the asymmetry of the leading edge vortex during wings' flapping (Sun and Xiong, 2005; Zhang and Sun, 2010). The previous study showed that anterior perturbation causes an alteration of body roll in bees (44.1ms after perturbation onset), followed by pitch (nose-down motion) and yaw (Ravi et al., 2013; Vance et al., 2013). By contrast, other flying insect deployed a dissimilar strategy to mitigate unsteady wind gust by prioritising yaw over roll and pitch [stalk-eyes fly (Vance et al., 2013), hawkmoth (Ortega-Jimenez et al., 2013)]. Any response to body motion prior to the alteration of symmetric wing strokes will

be characterized as passive response whereas the following active phase begins immediately after that (Vance et al., 2013). In this thesis, the response of anteriorly perturbated flies began with yaw (2.4ms) and follows with roll (5ms) and pitch (7.3ms, nose-up motion), which similar to what had been found earlier in stalk-eyes fly (Vance et al., 2013). The reason why yaw is more damped than roll and pitch is because the moment arm is maximum throughout the entire stoke cycle especially if flies imply horizontal stroke plane during predominant take-off manoeuvre. The passive body yaw alteration is 12.5 times faster than the time required for photo transduction and following visual motion computation in flies. In the meantime, all the body angular alterations are also lasted before they can elicit any visual responses. The 2.4ms response time puts this reflex among the fastest behavioural responses reported in volant insect kingdom [compared to 5ms in fruit flies (Beatus et al., 2015), 5-7.5ms in blowfly (Sandeman and Markl, 1980) and 11ms in cockroach (Jindrich and Full, 2002)]. The following alteration of wing strokes only began at 13.5-16.5ms after perturbation onset, which marked the beginning of an active phase of recovery, according to (Vance et al., 2013). Regardless of the direction of perturbation, I found flies first exhibit passive alteration in body angles prior to any adjustment of wing motions.

4-3. Wing kinematics

Houseflies modulate their wing kinematics to stay aloft, execute manoeuvres, and recover from aerial perturbation (Dickinson et al., 1993). Like other flying animals, flies alter wing stroke kinematics by changing angle of attack, wing trajectory and wing rotation angle at stroke reversal, thus alter aerodynamic forces (Fry et al., 2003; Sane, 2003) and body rotational moment (Götz, 1983; Götz, 1987; Zanker, 1990). However, it is unclear how do aerial perturbations affect wing kinematics and which variables will be altered. For instance, wingbeat amplitude and stroke frequency in fruit fly are the most crucial determinants of flight force (Zanker, 1990). My data support the earlier finding that flies typically decrease their wingbeat amplitude by 28% (left wing) and 22% (right wing), in response to impulsive perturbation from anterior. Simultaneously, flies also reduce the stroke frequency at t=13.5 (left wing) and t=16.5 (right wing) after perturbation onset, which is similar to wing kinematic trend to what had been found in another experiment (Vance et al., 2013). Also, flies shift their stroke plane in the direction of air stream (anterior perturbation shifted stroke plane backwards while posterior perturbation moved stroke plane forward). Despite of continuously perturbated flies altered their wingbeat amplitude, the alteration was relatively small and statistically insignificant.

During unintended body rotation, flies which previously engaged in symmetrical wing motion, exhibit a left-right asymmetry in wing velocity that acts to attenuate the animal's rotation (Vance et al., 2013). Asymmetrical wing beats then generate yaw corrective torque from the unbalanced drag on the wings (Ristroph et al., 2010). During lateral perturbation, wing stroke amplitude asymmetry shown in present analysis reaches 46° (right perturbation, Figure 3-19F, G) and 39° (left perturbation, Figure 3-19I, J), respectively. This asymmetry is significantly larger than the maximum asymmetry of 15° measured in tethered fruit flies (Dickinson, 1999) but relatively lower than flies facing mechanical stimuli (Beatus et al., 2015). The difference presumably occurred due to the different magnitude of perturbation, the effect of tethering and the nature of perturbation (mechanical or aerodynamic perturbations). The wingtip velocity asymmetry measured in this analysis ranges between $0.4ms^{-1}$ (left perturbation; Figure 3-21I, J) and $0.78ms^{-1}$ (right perturbation; Figure 3-21F, G). The change of wing motion, occurred 13.5ms and 19.5ms after perturbation onset, slightly before flies can generate antennae-meditated feedback (Fuller et al., 2014b). Therefore, only halteres-mediated feedbacks can regulate wing motion during aerial perturbation because it requires only 2.5-3ms of processing delays (Sandeman and Markl, 1980) or the changes are purely passive responses (Fritz-Olaf Lehmann, personal communication, 2016).

Besides wing beat angle, adjustments of wing angle of attack may also contribute to steering control and corrective manoeuvre in insect (Bergou et al., 2007; Dudley, 2002; Ristroph et al., 2010). Dipterans modulate their wing angle of attack to control aerodynamic force production [fruit fly (Ristroph et al., 2010); stalk-eye fly and bees (Vance et al., 2013)]. During downstroke, high wing angle of attack generates elevated lift whereas, during the upstroke, relatively low wing angle of attack pushes off the air in order to propel flies forward (Ristroph, 2011). Changes in wing angle of attack determine different projected area and further control the amount of drag force that can be produced. Larger area presented to the flow induces greater drag force. During impulsive perturbation from anterior, I found that a single exemplary fly decreased wing angle of attack (Figure 3-23G, H), which coincidely reduce wing frontal areas for two wing strokes (using pronation configurations), thus compromise the increasingly relative of airspeed and aerodynamic force production. In contrast to earlier findings, anteriorly perturbated flies increase wing projected areas during the upstroke, likely to generate more thrust that counter headwind (Jensen, 1956). Another idea is that, during upward stroke, headwind push on the highly flexible trailing edge of the wing, which leads to a reduction of wing angle of attack, thus wing chord rotation angle is more vertical (Ristroph, 2011). My data confirm this finding because anteriorly perturbated flies decreased wing angle

of attack by 96% (left wing, t=10.5ms) and 104% (right wing, t=13.5ms) compared to non-perturbated controls. It is consistent with those under turbulent conditions because flies keep high wing chord rotation angle (wing angle of attack, -34.8±15.7° during downstroke and 57.4±17.5° during upstroke) presumably to generate higher elevated force thus compensating sideways perturbation. The active responses of wing kinematics could not be determined in this thesis because of lack of information on complex spatial and temporal variation in continuous turbulent airflows. Even with this information, it is still challenging to determine the significances of active responses due to tight coupling between external flows and alteration of wing kinematics. Earlier findings also showed that insects do not respond to rapid fluctuations of interchanging flow behaviour (Ravi et al., 2013).

4-4. Directional sensitivity

Previous studies showed that bees have limited directional sensitivity to horizontal perturbations. Aerodynamics forces and thrust are actively generated only along vertical axis and body longitudinal axis, thus no active mechanism for roll stabilisation against lateral perturbation (Ravi et al., 2013). Therefore, bees need to manipulate the existing lift vector through turning manoeuvre or banking using subtle modulation of wing kinematic, in order to correct sideway perturbation (Combes and Dudley, 2009; Ravi et al., 2013). During perturbation from anterior, I found that flies are able to regain previous body orientation in a shorter period compared to lateral perturbation. Flies have a better opportunity to attenuate and further encountered the impact of the symmetrical perturbation since thrust is generated along the similar axis of oncoming airflow. By contrast, during lateral asymmetrical perturbation, flies demonstrated greater fluctuations in horizontal translational velocity and mostly failed to recover previous body angles within recording time (22ms after perturbation onset). This is consistent with data from mechanically perturbated fruit fly that able to regain previous body orientation only after 60ms (Ristroph et al., 2009).

In nature, dipterans have a tendency to fly upwind against the direction of the wind (Fuller et al., 2014b; Kennedy, 1940; Lutz, 1927). During forward flight, flies able to regulate thrust production to match the translational speed of airflow and overcome drag by inclining the stroke plane or pitch the body downward, thus, orientate lift vector more horizontally (Dudley, 2002). My data showed that, during anterior perturbation, flies also gain altitude at relatively low wing flapping frequency (decreased by 20.5%), presumably by exploiting the oncoming airflow (Figure 3-9F, Figure 3-21C, D). During level flight, it is suggested that flies have the opportunity to enhance additional lift by reducing

the wingbeat frequency, dynamically soar within the air stream and thus maintain consistent ground speed in the wind. This argument is only valid for downstroke (using pronation), thus, would be a good explanation on why the single exemplary fly sustained this wing stroke configuration for alonger period (approximately 11.7ms; Figure 3-23E, F). Wind gust from anterior adds velocity vector to one-half stroke (downstrokes) and subtract to another half stroke (upstrokes) of stroke cycle, yet, slightly tilt the net force vector backwards (Figure 4-3A). Flies take advantage of generated momentum from the horizontally blowing airflow that can reduce the elevated mechanical power expenditure required to move or flap the wings up and down (Dickinson and Tu, 1997; Stuart, 1958).

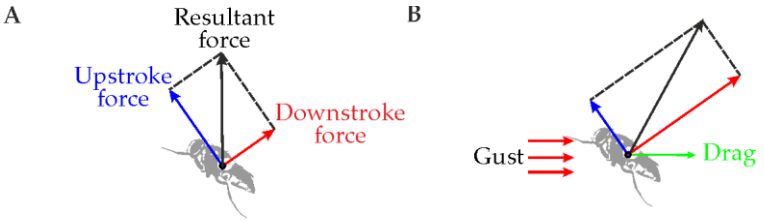

Figure 4-3: Force balance of a fly facing (A) an impulsive wind gust from anterior compared to (B) non-perturbated controls. Drag should increase during up and downstroke but it always act in the direction of flow.

At 0°of perturbation direction (body-oriented directly into the flow), the amount of drag is similar on both sides of the body. By comparing the left-right wingtip velocity of tethered flies during anterior perturbation, my data showed that flies actuated symmetry wing flapping and no subtle difference in stroke kinematics between left and right wings (Figure 3-25). Each wing equally contributes to corrective yaw and roll torque during anterior perturbation but in the opposite direction where resultant moments are zero throughout stroke cycle. It is known as bilaterally symmetric of wings' motions (Fry et al., 2005; Ristroph et al., 2010). Flies impose a minimal change in yaw and roll as well as fast recovery after being perturbated. During anterior perturbation, the alteration of body yaw lasts earlier compared to flies facing perturbation from lateral (17.5ms versus 21ms during left perturbation and 30ms during right perturbation). This similar trend also holds for roll because the alteration lasts after 13ms compared to flies facing perturbation from lateral (19ms during left perturbation and 29ms during right perturbation).

The orientation of inclined stroke plane with respect to the direction of oncoming as the main moment arm of net aerodynamic forces is among the key factors which attribute to this change in body angle (Wootton et al., 2003b). Alteration of inclined stroke plane during flight will elicit change in flies' body angles especially pitching moments (Dudley, 2002). My data corroborates with the earlier study because both flies' body pitching moment and inclined stroke plane were simultaneously affected during anterior perturbation (Figure 3-7F and Figure 3-20Eiii-iv). In addition, Ristroph et al., 2013 conducted a pioneering study of flies under lateral perturbation deployed asymmetries in rowing motion to corrective counter-torque immediately after perturbation onset. Intriguingly, my data vary substantially from previous experiments because active responses of wing motion during lateral perturbation were less noticeable compared to perturbation from anterior (please refer to time trace of instantaneous p-values calculated from statistical comparison). It is possible that the differences in observation are due to the type of perturbation; flies in my experiment facing aerodynamic perturbation whereas the parallel experiment used mechanical perturbation.

4-5. Energetic expenditure

The power output of flight muscles determines the limit of locomotion and flight performance during turbulence (Combes and Dudley, 2009). However, the findings are inconsistent weather unsteady flow increase or decrease the locomotion cost. Wakes or unidirectional wind may diminish the cost of locomotion [trout swimming against Von Kalman vortices, (Liao et al., 2003), birds flying inside vortices shed during formation flight, (Higdon and Corrsin, 1978; Lissaman and Shollenberger, 1970; Weimerskirch et al., 2001) and web-footed sea-birds facing unidirectional wind gust (Weimerskirch et al., 2002)]. However, other data showed contradictory findings of higher energy expenditure demand especially during unstructured and chaotically moving flow [bees, (Combes and Dudley, 2009), flocking birds (Usherwood et al., 2011), juvenile salmon (Enders et al., 2003)]. However, these views have been questioned by a numerical approach that flight power of bumblebees is independent of heavy turbulence flight condition (Engels et al., 2016). In freely flying insects, the measurement of energetic expenditure by carbon dioxide release rate is challenging compared to tethered flight (Gilmour and Ellington, 1993; Lehmann and Dickinson, 1998; Lehmann et al., 2000). Besides, none of them considered the effect of turbulence flows in their analysis.

According to previous studies, a possible way of reducing energy expenditures is to decrease wing flapping frequency (Butler and Woakes, 1980; Lehmann,

2001). Although flapping frequency is only one parameter of wing kinematic, it is a useful rough indicator of energy expenditure in flying insects in response to the change in flow conditions. Also, measurement of oxygen uptake is a well-established approach that has been used to assess energy expenditure (Davis and Fraenkel, 1940). I did not implement any measurement of oxygen uptake during aerial perturbation, however, by correlating this oxygen consumption and flapping velocity, the energy expenditure can be approximated. For example, my data shown that anteriorly perturbated flies decrease their flapping frequency by 20.5% (cf. Chapter 3-5-4-2), will coincidely decrease the same percentage of oxygen consumption compared to non-perturbated controls as listed in Table 4-1. Although the decrease of flapping frequency will lead to loss of flight altitude, the simultaneous increasing strength of wind gust will keep flight force and body weight in balance.

Table 4-1: Total oxygen consumption in housefly undergoing two different level of physical activity.

Temperature	**Group**	**Oxygen consumption (μ1/hr/mg) of non-perturbated controls** (Sohal, 1982)	**Oxygen consumption (μ1/hr/mg) of anteriorly perturbated flies**
18°C	Low activity	4.0±0.5	3.2±0.5
	High activity	4.6±0.5	3.7±0.5
25°C	Low activity	7.1±0.4	5.6±0.4
	High activity	9.45±0.8	7.5±0.8

Wing venation provides structural rigidity and membranes allow wings to deform or dynamically change its profile (Chapman, 2012). High compliance of wings diminish the implication of predominant inertia forces (Lehmann et al., 2011) or collision with solid objects during flapping (Wootton, 1992), which may cause structural damages. In flapping insect flight, previous studies have also shown that elastic energy recycling by wing flexing within stroke cycle may also limit the energetic expenditure (Casey and Ellington, 1989; Dickinson and Lighton, 1995; Ellington, 1984d). Fruit fly, for example, requires at least 10% of elastic storage to minimize flight cost during hovering (Dickinson and Lighton, 1995). By contrast to earlier findings, Lehmann and his co-workers shown that the elastic wing of blowflies do not recycle much energy from the previous half

stroke because acting forces were partly cancelled out each other (Lehmann et al., 2011). However, the implications of elastic wing deformation towards energetic expenditure during unsteady flow received little study compared to steady-state. Superficially, I observed and found that the dynamic change of wing profile during three-dimensional reconstruction (cf. Figure 2-11), but still requires detail quantifications and analysis. Therefore, further analysis on the implication of structural deformation on flies' wings needs to be undertaken before any validation of the earlier findings can be carried out.

4-6. Sensing change of airflow by sensory receptors

Houseflies are widely known for their aerial agility even when flying under unsteady condition (Wagner, 1986). Abrupt change in body motion and wing kinematics during aerial perturbations is sensory-dependent (Engels et al., 2016). Flow can be sensed by a distinct receptor or by an integrated multimodal of the mechanosensory system (Christensen, 2004). However, the multisensory with enhancement of synergistic integration has better performance compared to unimodal sensory (Guo and Guo, 2005; Meredith and Stein, 1986). During rapids aerial disturbances, flying insects require an efficient receptor with fast reaction time for stabilisation. Delay in close loop sensory architecture is thus a key factor that determines flight stability and performance (Elzinga et al., 2012).

There are four types of sensory receptors such as visual sensors, deformation sensors, flow sensors and body velocity sensors. Visual sensors, for instance, compound eyes and ocelli, may offer ground speed compensation against change of ambient airspeed (Dudley, 2002). However, lengthy processing delays will definitely limits the ability of the entire sensory feedback circuit to counter abrupt change of body motion, particularly during wind gust. It is also reported that beyond $50°s^{-1}$ change of body angular velocity, the role of visually mediated flight control gradually weakens (Guo and Guo, 2005). Previous findings clearly indicate that visual sensor alone is not able to encode rapid corrective responses against rapid perturbations without integration with faster mechanoreceptors (Beatus et al., 2015; Fuller et al., 2014b). Meanwhile, deformation sensor such as micro sensillae campaniform and vibratory bristles along the wings is multidirectional turbulence sensor that has a directional sensitivity to sense the changes in airflow via chordwise deformation (Dickinson, 1992; Sterbing-D'Angelo et al., 2011). There are not many studies about how efficient these tiny receptors sense aerodynamic perturbations or possibly integrated with other modalities because the experimental tasks are challenging to be implemented. Therefore, by taking into account the limit of housefly's sensory processing time for flight control during impulsive wind gust and data available, the remaining

sensory receptors that can be considered are flow sensors and body velocity sensors. Body velocity sensors like halteres which directly connected with motor neurons are able to react even faster within 2.5-3ms against rapid changes of angular body rotation (Sandeman and Markl, 1980). However, studies also showed that Johnston's organ, a chordotonal organ in the antennae is able to sense a change of airspeed even with shorter processing delay [~20ms for fruit fly (Fuller et al., 2014b), 20.3ms for the bee (Vance et al., 2013)] at higher gain. This is consistent with the previous study shown that, beyond 1000°s^{-1} of body angular velocity, halteres-mediated responses will take over to encode angular body motion (Sherman and Dickinson, 2003).

In my present study the alteration of free flight body motion during lateral impulsive perturbation are relatively high (up to 3229°s^{-1} about the roll axis and 2300°s^{-1} about a yaw axis; see Figure 3-8H and Figure 3-6H). This fast-growing alteration of body motion indicates that it is likely halteres are the responsible sensory receptors which regulate impulsive perturbations compared to antennae. The changes of free moving appendages of wing strokes are one of the criteria to determine the onset active corrective responses (Vance et al., 2013). The decrease of strokewise-averaged wingtip velocity during impulsive anterior perturbation began at 13.5ms to 16.5ms after the onset (rate of decrease -50ms^{-2}±11 in the left wing and -41.2ms^{-2}±8 in the right wing; Figure 3-21E). While this alteration of wing motion occurred at approximately ~2.5 stroke cycles (~15ms) after perturbation onset, flies' body angle encountered maximum alteration of body angle (18ms about the yaw axis, 15ms about the pitch axis and 11ms about roll axis). The succeeding experiment on tethered flies with disable gyroscopic feedback offers better insight about the engagement of this mechanosensor to the entire sensory architecture. The decrease of wingtip velocities indicates that flies with disabled-halteres still react against impulsive perturbations, even with earlier reaction onset than intact flies (~3ms versus ~15ms) with a higher rate of decrease (-98.8ms^{-2}±9 in the left wing and -122ms^{-2}±25 in the right wing versus -50.11 in the left wing and -41.8ms in the right wings). Houseflies react to wind gust 7ms faster than fruit flies which have a longer processing delay of 10ms as previously recorded by Fuller and his co-workers (Fuller et al., 2014b). The impairment of halteres functionality presumably urged antennae to respond earlier as an alternate receptor. In my experiment, during anterior perturbation, antennae have the opportunity to sense the oncoming gust earlier compared to lateral and posterior wind gust. Flies then gradually regulate corrective responses before air stream reached the center of the body and wings. Therefore, my data showed that posteriorly perturbated flies unequivocally demonstrated transient reduction of wingtip velocity during perturbation onset compared to anteriorly perturbated flies

(Figure 3-24D-F and Figure 3-26D-F). The following experiment using tethered flies with immobilized antennae further validated the importance of this flow sensory receptor. My result has thus showed that flies with disabled antennae again delayed their responses 16.5ms after perturbation onset but the rate of recovery is 2-fold lower compared to intact flies (rate of wingtip velocity recovery: $26ms^{-2}$ versus $57ms^{-2}$). Taken together, the empirical data provide a new understanding of sensory feedback suppression not only impair multimodal sensory architecture and further affect flies' response time but also undermine rate of recovery.

5. Concluding remarks

Flight animal requires energy to overcome friction, drag, inertia and gravity but also energy to contend unpredictable aerodynamic perturbations. Multidirectional turbulence and sudden wing gusts may harm natural fliers, causing fast-diverging flight instabilities. However, several limitations to this experimental study need to be acknowledged. The outcomes of the presented experiments cannot be easily applied to other species and only hold for certain range of flight condition. Essentially, comparative studies should be conducted in the future using various taxa to determine the general rules of body and wings' kinematics during perturbation.

The current state advancement of experimental apparatus using automated 3D high-speed videography, which also associated with optical detection system and perturbation generators and potent flow quantification techniques, eliminates the previous time-consuming, complicated and unreliable approaches. The current findings also add substantially to our understanding of resulting changes of wing kinematics and flies' body postures including their response time during aerodynamic perturbations are the basis of active flight stabilization and control. Eventually, the effect of body posture and wing motion must manifest themselves through the production of aerodynamics forces, but the associated mechanisms are remarkably complex, comprising unsteady and separated flows. Flies demand mechanism that is not only able to attenuate disturbances and keeping upright against instability but also further exploiting the oncoming flow to elevate lifting forces during aerial mobility. The present findings provide additional evidence that insect flight stabilization and control is made possible only by integrated multimodal of the sensory system, which prevents a complete dependency on a specific input. The empirical findings also highlight the importance of fast processing mechanosensory feedback for stabilisation especially during interchanging short-term flight disruptions which previously received less qualitative, functional and descriptive attention.

It would be interesting to investigate the extracted data on subtle head, abdomen and legs coordination during aerial perturbations. This is consistent with data from freely non-perturbated fruit flies which highlights motion of these appendages might be part of trimming reflexes, which encounter imbalances during flight (Berthé and Lehmann, 2015). In addition, further estimations of the fluid forces, perhaps by using the semi-empirical unsteady blade element (USBE) model (Lehmann et al., 2011), computational fluid dynamics (CFD) analysis (Engels et al., 2016; Shyy et al., 2008), and a physical robotic wing experiment can calculate all the aerodynamics forces, added mass reaction force and Magnus

force including inertia. My current study, however, does not quantify wing deformation, even though the extracted painted and virtual markers are sufficient to estimate structural deformation including wing camber (Walker et al., 2008), torsional compliance (Ennos, 1995) and spanwise deformation (Lehmann et al., 2011). By having a complete package of body and wing motion, elaborate structural deformation and forces may lead to a new field of study on dynamics fluid-structure interaction and aeroelasticity. Additional experimental works should be done to incorporate the existing experimental setups including the turbulence generator with respirometry apparatus to directly measure the metabolic output.

This research accommodates a basis for future research on control and stability during the flight of natural fliers including biomimetic flying machines. Within the last decade, there was a considerable progress in the development of bio-inspired Micro Aerial Vehicles MAV designed by engineers and physicist (de Croon et al., 2015; Richter and Lipson, 2011; van Breugel et al., 2010; van Breugel et al., 2008; Zdunich et al., 2007). I hope that the ideas and findings of this inter-disciplinary thesis will help engineers and biologists to enhance their understanding of insect flight further especially in term of control and stability during aerial aerodynamic perturbations. My empirical findings also highlight the importance of each highly specialized biological sensor and provide insight into ongoing multimodal sensory technologies.

6. References

[1]**Abdel-Aziz, Y. I. and Karara, H. M.** (1971). Direct linear transformation into object space coordinates in close-range photogrammetry. *Proceedings of the Symposium on Close-Range Photogrammetry,* pp.1-18.

[2]**Abzug, M. J. and Larrabee, E. E.** (2005). *Airplane Stability and Control A History of the Technologies that Made Aviation Possible.* Cambridge University Press.

[3]**Alexander, D. E.** (1986). Wind tunnel studies of turns by flying dragonflies. *Journal of Experimental Biology,* **122,** pp. 81-98.

[4]**Anderson, D. W. and Eberhardt, S.** (2009). *Understanding Flight.* McGraw-Hill Professional.

[5]**Aström, K. J. and Murray, R. M.** (2008). *Feedback Systems: An Introduction for Scientists and Engineers.* Princeton University Press.

[6]**Bacon, J. and Möhl, B.** (1979). Activity of an identified wind interneurons in a flying locust. *Nature,* **278,** pp. 638-640.

[7]**Balint, C. N. and Dickinson, M. H.** (2004). Neuromuscular control of aerodynamic forces and moments in the blowfly, *Calliphora vicina*. *Journal of Experimental Biology,* **207,** pp. 3813-3838.

[8]**Batchelet, A.** (1981). *Circular Statistics in Biology (Mathematics in biology).* Academic Press Inc.

[9]**Beatus, T., Guckenheimer, J. M. and Cohen, I.** (2015). Controlling roll perturbations in fruit flies. *Journal of The Royal Society Interface,* **12,**.

[10]**Beenakkers, A. M. T.** (1969). Carbohydrate and fat as a fuel for insect flight. A comparative study. *Journal of Insect Physiology,* pp. 353.

[11]**Bender, J. A. and Dickinson, M. H.** (2006). A comparison of visual and haltere-mediated feedback in the control of body saccades in *Drosophila melanogaster*. *Journal of Experimental Biology,* **209,** pp. 4597-4606.

[12]**Berger, S. and Kutsch, W.** (2003). Turning manoeuvres in free-flying locusts: High-speed video-monitoring. *Journal of Experimental Zoology. Part A: Comparative Experimental Biology,* **299A,** pp. 127-138.

[13]**Bergou, A. J., Xu, S. and Wang, Z. J.** (2007). Passive wing pitch reversal in insect flight. *Journal of Fluid Mechanics,* **591,** pp. 321-337.

[14]**Berthé, R. and Lehmann, F.** (2015). Body appendages fine-tune posture and moments in freely manoeuvring fruit flies. *Journal of Experimental Biology,* **218,** pp. 3295-3307.

[15]**Bomphrey, R. J., Walker, S. M. and Taylor, G. K.** (2009). The typical flight performance of blowflies: measuring the normal performance envelope of *Calliphora vicina* using a novel corner-cube arena. *PLoS ONE,* **4,** pp. e7852.

[16]**Briscoe, A. D. and Chittka, L.** (2001). The evolution of colour vision in insects. *Annual Review of Entomology,* pp. 471-510.

[17]**Butler, P. J. and Woakes, A. J.** (1980). Heart rate, respiratory frequency and wingbeat frequency of free-flying barnacle geese *Branta Leucopsis*. *Journal of Experimental Biology,* **85,** pp. 213-226.

[18]**Camhi, J. M.** (1970). Sensory control of abdomen posture in flying locusts. *Journal of Experimental Biology,* **52,** pp. 533-537.

[19]**Card, G. and Dickinson, M. H.** (2008b). Visually mediated motor planning in the escape response of *Drosophila*. *Current Biology,* **18,** pp. 1300-1307.

[20]**Casas, J. and Simpson, S.** (2008). *Insect Mechanics and Control: Advances in Insect Physiology.* Academic Press.

[21]**Casey, T. M. and Ellington, C. P.** (1989). *Energetics of insect flight. In Energy Transformations in Cells and Organisms (ed. W. Wieser and E. Gnaiger).*, pp. 200- 210 Stuttgart: Thieme.

[22]**Chai, P. and Dudley, R.** (1995). Limits to vertebrate locomotor energetics suggested by hummingbirds hovering in heliox. *Nature,* **377,** pp. 722-725.

[23]**Chapman, R. F.** (2012). *The Insects: Structure and Function.* Cambridge University Press.

[24]**Chapman, J. W. and Goulson, D.** (2000). Environmental versus genetic influences on fluctuating asymmetry in the house fly, *Musca domestica*. *Biological Journal of the Linnean Society,* **70,** pp. 403-413.

[25]**Chapman, J., Klaassen, R. G., Drake, V., Fossette, S., Hays, G., Metcalfe, J., Reynolds, A., Reynolds, D. and Alerstam, T.** (2011). Animal orientation strategies for movement in flows. *Current Biology,* **21,** pp. R861-R870.

[26]**Cheng, B., Fry, S. N., Huang, Q. and Deng, X.** (2010). Aerodynamic damping during rapid flight maneuvers in the fruit fly *Drosophila*. *Journal of Experimental Biology,* **213,** pp. 602-612.

[27]**Christensen, T. A.** (2004). *Methods in Insect Sensory Neuroscience.* CRC Press.

[28]**Combes, S. A. and Dudley, R.** (2009). Turbulence-driven instabilities limit insect flight performance. *Proceedings of the National Academy of Sciences of the United States of America,* **106,** pp. 9105-9108.

[29]**Cornwell, P. B.** (1955). The functions of the ocelli of *Calliphora* (Diptera) and *Locusta* (Orthoptera). *Journal of Experimental Biology,* **32,** pp. 217-237.

[30]**Crall, J. and Combes, S.** (2013). Blown in the wind: bumblebee temporal foraging patterns in naturally varying wind conditions. *Integrative and Comparative Biology,* **53,** pp. E270-E270.

[31]**Crespo, J. G., Goller, F. and Vickers, N. J.** (2012). Pheromone mediated modulation of pre-flight warm-up behavior in male moths. *Journal of Experimental Biology,* **215,** pp. 2203-2209.

[32]**Dalton, S.** (1975). *Borne on the wind: Extraordinary world of insects in flight.* Reader's Digest Press.

[33]**David, C. T.** (1978). The relationship between body angle and flight speed in free-flying *Drosophila*. *Physiological Entomology,* **3,** pp. 191-195.

[34]**Davies, W. M.** (1936). Studies on the Aphides infesting the potato crop: Laboratory experiments on the effect of the wind velocity on the flight of *Myzus Persicae Sulz*. *Annals of Applied Biology,* **23,** pp. 401-408.

[35]**Davis, R. A. and Fraenkel, G.** (1940). The oxygen consumption of flies during flight. *Journal of Experimental Biology,* **17,** pp. 402-407.

[36]**de Croon, G. C. H. E., Perçin, M., Remes, B. D. W., Ruijsink, R. and De Wagter, C.** (2015). *The DelFly: Design, aerodynamics, and artificial intelligence of a flapping wing robot.* Springer.

[37]**Deck, S., Gand, F., Brunet, V. and Ben Khelil, S.** (2014). High-fidelity simulations of unsteady civil aircraft aerodynamics: stakes and perspectives. Application of zonal detached eddy simulation. *Philosophical Transactions of the Royal Society of London. A: Mathematical, Physical and Engineering Sciences,* **372,** pp. 20130325.

[38]**Denker, J. S.** (1996). *See How It Flies: Perceptions, Procedures and Principles of Flight.* TAB Books Inc.

[39]**Dickerson, B. H., Aldworth, Z. N. and Daniel, T. L.** (2014). Control of moth flight posture is mediated by wing mechanosensory feedback. *Journal of Experimental Biology,* **217,** pp. 2301-2308.

[40]**Dickinson, M. H., Lehmann, F. O. and Götz, K. G.** (1993). The active control of wing rotation by *Drosophila*. *Journal of Experimental Biology,* **182,** pp. 173-189.

[41]**Dickinson, M. H., Lehmann, F. O. and Sane, S. P.** (1999). Wing rotation and the aerodynamic basis of insect flight. *Science (New York, N.Y.),* **284,** pp. 1954-1960.

[42]**Dickinson, M. H. and Lighton.** (1995). Muscle efficiency and elastic storage in the flight motor of *Drosophila*. *Science,* **268,** pp. 87-90.

[43]**Dickinson, M. H.** (1992). Directional sensitivity and mechanical coupling dynamics of campaniform sensilla during chordwise deformations of the fly wing. *Journal of Experimental Biology,* **169,** pp. 221-233.

[44]**Dickinson, M. H.** (1999). Haltere-mediated equilibrium reflexes of the fruit fly, *Drosophila melanogaster*. *Philosophical Transactions of the Royal Society of London, B: Biological Sciences,* **354,** pp. 903-916.

[45]**Dickinson, M. H. and Tu, M. S.** (1997). The function of *Dipteran* flight muscle. *Comparative Biochemistry and Physiology Part A: Physiology,* **116,** pp. 223-238.

[46]**Digby, P. S. B.** (1958). Flight activity in the blowfly *Calliphora Erythrocephala*, in relation to light and radiant heat, with special reference to adaptation. *Journal of Experimental Biology,* **35,** pp. 1-19.

[47]**Dixon, A. F. G. and Mercer, D. R.** (1983). Flight behaviour in the Sycamore Aphid: Factors affecting take-off. *Entomologia Experimentalis et Applicata,* **33,** pp. 43-49.

[48]**Dudley, R. and Ellington, C. P.** (1990). Mechanics of forward flight in bumblebees: I. Kinematics and morphology. *Journal of Experimental Biology,* **148,** pp. 19-52.

[49]**Dudley, R.** (2002). *Book Review-The biomechanics of insect flight: form, function, evolution.* Princeton University Press, Princeton, NJ.

[50]**Dyhr, J. P., Morgansen, K. A., Daniel, T. L. and Cowan, N. J.** (2013). Flexible strategies for flight control: an active role for the abdomen. *Journal of Experimental Biology,* **216,** pp. 1523-1536.

[51]**Ellington, C. P.** (1985). Power and efficiency of insect flight muscle. *Journal of Experimental Biology,* **115,** pp. 293-304.

[52]**Ellington, C. P.** (1984a). The aerodynamics of hovering insect flight. I. The quasi-steady analysis. *Philosophical Transactions of the Royal Society of London.B, Biological Sciences,* **305,** pp. 1-15.

[53]**Ellington, C. P.** (1984b). The aerodynamics of hovering insect flight. III. Kinematics. *Philosophical Transactions of the Royal Society of London. B: Biological Sciences,* **305,** pp. 41-78.

[54]**Ellington, C. P.** (1984c). The aerodynamics of hovering insect flight. V. A vortex theory. *Philosophical Transactions of the Royal Society of London. B: Biological Sciences,* **305,** pp. 115-144.

[55]**Ellington, C. P.** (1984d). The aerodynamics of hovering insect flight. VI. Lift and power requirements. *Philosophical Transactions of the Royal Society of London.B, Biological Sciences,* **305,** pp. 145-181.

[56]**Ellington, C. P.** (1991). Limitations on animal flight performance. *Journal of Experimental Biology,* **160,** pp. 71-91.

[57]**Ellington, C. P., van, d. B., Willmott, A. P. and Thomas, A. L. R.** (1996). Leading-edge vortices in insect flight. *Nature,* **384,** pp. 626-630.

[58]**Elzinga, M. J., Dickson, W. B. and Dickinson, M. H.** (2012). The influence of sensory delay on the yaw dynamics of a flapping insect. *Journal of the Royal Society Interface,* **9,** pp. 1685-1696.

[59]**Enders, E. C., Boisclair, D. and Roy, A. G.** (2003). The effect of turbulence on the cost of swimming for juvenile Atlantic salmon (*Salmo salar*). *Canadian Journal of Fisheries and Aquatic Sciences,* pp. 1149.

[60]**Engels, T., Kolomenskiy, D., Schneider, K., Lehmann, F. O. and Sesterhenn, J.** (2016). Bumblebee flight in heavy turbulence. *Physical Review Letters,* **116,** pp. 028103.

[61]**Ennos, A. R.** (1988). The inertial cause of wing rotation in *Diptera*. *Journal of Experimental Biology,* **140,** pp. 161-169.

[62]**Ennos, A. R.** (1995). Mechanical behaviour in torsion of insect wings, blades of grass and other cambered structures. *Proceedings of the Royal Society of London. B: Biological Sciences,* **259,** pp. 15-18.

[63]**Ennos, A. R.** (1989). The kinematics and aerodynamics of the free flight of some *Diptera*. *Journal of Experimental Biology,* **142,** pp. 49-85.

[64]**Faruque, I. and Sean Humbert, J.** (2010a). Dipteran insect flight dynamics. Part 1: Longitudinal motion about hover. *Journal of Theoretical Biology,* **264,** pp. 538-552.

[65]**Faruque, I. and Sean Humbert, J.** (2010b). Dipteran insect flight dynamics. Part 2: Lateral-directional motion about hover. *Journal of Theoretical Biology,* **265,** pp. 306-313.

[66]**Fayyazuddin, A. and Dickinson, M. H.** (1996). Haltere afferents provide direct, electronic input to a steering motor neuron in the blowfly, *Calliphora*. *Journal of Neuroscience,* **16,** pp. 5225-5232.

[67]**Fisher, N. I.** (1993). *Statistical Analysis of Circular Data.* Cambridge University Press.

[68]**Fraenkel, G. and Pringle, J. W. S.** (1938). Biological sciences: Halteres of flies as gyroscopic organs of equilibrium. *Nature,* **141,** pp. 919-920.

[69]**Fry, S. N., Sayaman, R. and Dickinson, M. H.** (2003). The aerodynamics of free-flight maneuvers in *Drosophila*. *Science,* **300,** pp. 495-498.

[70]**Fry, S. N., Sayaman, R. and Dickinson, M. H.** (2005). The aerodynamics of hovering flight in *Drosophila*. *Journal of Experimental Biology,* **208,** pp. 2303-2318.

[71]**Fuller, S. B., Karpelson, M., Censi, A., Ma, K. Y. and Wood, R. J.** (2014a). Controlling free flight of a robotic fly using an onboard vision sensor inspired by insect ocelli. *Journal of the Royal Society Interface,* **11,** pp. 20140281.

[72]**Fuller, S. B., Straw, A. D., Peek, M. Y., Murray, R. M. and Dickinson, M. H.** (2014b). Flying *Drosophila* stabilize their vision-based velocity controller by sensing wind with their antennae. *Proceedings of the National Academy of Sciences,* **111,** pp. 1182-1191.

[73]**Fuse, M. and Truman, J. W.** (2002). Modulation of ecdysis in the moth *Manduca sexta*: the roles of the suboesophageal and thoracic ganglia. *Journal of Experimental Biology,* **205,** pp. 1047-1058.

[74]**Gao, N., Aono, H. and Liu, H.** (2009). A numerical analysis of dynamic flight stability of hawkmoth hovering. *Journal of Biomechanical Science and Engineering,* **4,** pp. 105-116.

[75]**Gao, N., Aono, H. and Liu, H.** (2011). Perturbation analysis of 6-DoF flight dynamics and passive dynamic stability of hovering fruit fly *Drosophila melanogaster*. *Journal of Theoretical Biology,* **270,** pp. 98-111.

[76]**Gilmour, K. M. and Ellington, C. P.** (1993). Power output of glycerinated bumblebee flight muscle. *Journal of Experimental Biology,* **183,** pp. 77-100.

[77]**Goldsmith, T. H. and Fernandez, H. R.** (1968). The sensitivity of housefly photoreceptors in the mid-ultraviolet and the limits of the visible spectrum. *Journal of Experimental Biology,* **49,** pp. 669-677.

[78]**Götz, K. G.** (1983). Bewegungssehen and Flugsteuerung bei der Fliege *Drosophila*. *In BIONA Report,* **2,** pp. 21-34.

[79]**Götz, K. G.** (1968). Flight control in *Drosophila* by visual perception of motion. *Kybernetik,* **4,** pp. 199-208.

[80]**Götz, K. G.** (1987). Course-control, metabolism and wing interference during ultralong tethered flight in *Drosophila Melanogaster*. *Journal of Experimental Biology,* **128,** pp. 35-46.

[81]**Guo, J. and Guo, A.** (2005). Crossmodal interactions between olfactory and visual learning in *Drosophila*. *Science,* **309,** pp. 307-310.

[82]**Haag, J., Wertz, A. and Borst, A.** (2010). Central gating of fly optomotor response. *Proceedings of the National Academy of Sciences,* **107,** pp. 20104-20109.

[83]**Haggard, P. and Wing, A. M.** (1990). Assessing and reporting the accuracy of position measurements made with optical tracking systems. *Journal of Motor Behavior,* **22,** pp. 315-321.

[84]**Haine, E.** (1955). Aphid take-off in controlled wind speeds. *Nature,* **175,** pp. 474-475.

[85]**Hanski, I. K., Stevens, P. C., Ihalempiä, P. and Selonen, V.** (2000). Home-range size, movements, and nest-site use in the siberian flying squirrel, pteromys Volans. *Journal of Mammalogy,* **81,** pp. 798-809.

[86]**Haslwanter, T.** (1995). Mathematics of three-dimensional eye rotations. *Vision research,* **35,** pp. 1727-1739.

[87]**Hastings A., Yeates D. and Hamilton J.** (Digital image) Anatomical atlas of flies (*Calyptrate*). http://www.ento.csiro.au/biology/fly/flyGlossary.html.

[88]**Hedrick, T. L.** (2008). Software techniques for two- and three-dimensional kinematic measurements of biological and biomimetic systems. *Bioinspiration and Biomimetics,* **3,** pp. 34001.

[89]**Hedrick, T. L., Cheng, B. and Deng, X.** (2009). Wingbeat time and the scaling of passive rotational damping in flapping flight. *Science,* **324,** pp. 252-255.

[90]**Hesselberg, T. and Lehmann, F.** (2007). Turning behaviour depends on frictional damping in the fruit fly *Drosophila*. *Journal of Experimental Biology,* **210,** pp. 4319-4334.

[91]**Higdon, J. and Corrsin, S.** (1978). Induced drag of a bird flock. *The American Naturalist,* **112,** pp. 727-744.

[92]**Hollick, F. S. J.** (1940). The flight of the dipterous fly *Muscina stabulans* fallen. *Philosophical Transactions of the Royal Society of London. B: Biological Sciences,* **230,** pp. 357-390.

[93]**Hubel, T. Y., Riskin, D. K., Swartz, S. M. and Breuer, K. S.** (2010). Wake structure and wing kinematics: The flight of the lesser dog-faced fruit bat, *Cynopterus brachyotis*. *Journal of Experimental Biology,* **213,** pp. 3427-3440.

[94]**Jensen, M.** (1956). Biology and physics of locust flight. III. The aerodynamics of locust flight. *Philosophical Transactions of the Royal Society of London. Series B, Biological Sciences,* **239,** pp. 511-552.

[95]**Jindrich, D. L. and Full, R. J.** (2002). Dynamic stabilization of rapid hexapedal locomotion. *Journal of Experimental Biology,* **205,** pp. 2803-2823.

[96]**Johnston, J. S. and Heed, W. B.** (1976). Dispersal of desert-adapted *Drosophila*: The Saguaro-breeding *D. nigrospiracula*. *The American Naturalist,* **110,** pp. 629-651.

[97]**Kennedy, J. S.** (1939). The behaviour of the desert locust (*Schistocerca gregaria* (Forsk.))(Orthopt.) in an outbreak center. *Transactions of the Royal Entomological Society of London,* **89,** pp. 385-542.

[98]**Kennedy, J. S.** (1940). The visual responses of flying mosquitoes. *Proceedings of the Zoological Society of London,* **A109,** pp. 221-242.

[99]**Klassen, W. and Hocking, B.** (1964). The influence of a deep river valley system on the dispersal of Aedes mosquitos. *Bulletin of entomological research,* **55,** pp. 289-304.

[100]**Koehl, M. A. R. and Reidenbach, M. A.** (2007). Swimming by microscopic organisms in ambient water flow. *Experiments in Fluids,* **43,** pp. 755-768.

[101]**Kunz, T. H., Gauthreaux, S. A., Jr, Hristov, N. I., Horn, J. W., Jones, G., Kalko, E. K., Larkin, R. P., McCracken, G. F., Swartz, S. M., Srygley, R. B. et al.** (2008). Aeroecology: probing and modeling the aerosphere. *Integrative and Comparative Biology,* **48,** pp. 1-11.

[102]**Lee, A.** (2013).Virtual Dub 1.9.9. http://www.virtualdub.org/.

[103]**Lehmann, F. O. and Dickinson, M. H.** (1997). The changes in power requirements and muscle efficiency during elevated force production in the fruit fly *Drosophila melanogaster*. *Journal of Experimental Biology,* **200,** pp. 1133-1143.

[104]**Lehmann, F. and Dickinson, M. H.** (1998). The control of wing kinematics and flight forces in fruit flies (*Drosophila spp.*). *Journal of Experimental Biology,* **201,** pp. 385-401.

[105]**Lehmann, F.** (2001). The efficiency of aerodynamic force production in *Drosophila*. *Comparative Biochemistry and Physiology Part A: Molecular & Integrative Physiology,* **131,** pp. 77-88.

[106]**Lehmann, F.** (2004). The mechanisms of lift enhancement in insect flight. *Die Naturwissenschaften,* **91,** pp. 101-122.

[107]**Lehmann, F., Dickinson, M. H. and Staunton, J.** (2000). The scaling of carbon dioxide release and respiratory water loss in flying fruit flies (*Drosophila spp.*). *Journal of Experimental Biology,* **203,** pp. 1613-1624.

[108]**Lehmann, F., Gorb, S., Nasir, N. and Schützner, P.** (2011). Elastic deformation and energy loss of flapping fly wings. *Journal of Experimental Biology,* **214,** pp. 2949-2961.

[109]**Lehmann, F. and Pick, S.** (2007). The aerodynamic benefit of wing–wing interaction depends on stroke trajectory in flapping insect wings. *Journal of Experimental Biology,* **210,** pp. 1362-1377.

[110]**Liao, J. C., Beal, D. N., Lauder, G. V. and Triantafyllou, M. S.** (2003). Fish exploiting vortices decrease muscle activity. *Science,* **302,** pp. 1566-1569.

[111]**Lin, T., Zheng, L., Hedrick, T. and Mittal, R.** (2012). The significance of moment-of-inertia variation in flight manoeuvres of butterflies. *Bioinspiration and Biomimetics,* **7,** pp. 044002.

[112]**Lissaman, P. B. S. and Shollenberger, C. A.** (1970). Formation flight of birds. *Science,* **168,** pp. 1003-1005.

[113]**Liu, B., Ristroph, L., Weathers, A., Childress, S. and Zhang, J.** (2012). Intrinsic stability of a body hovering in an oscillating airflow. *Physical Review Letters,* **108,** pp. 068103.

[114]**Liu, Y. and Sun, M.** (2008). Wing kinematics measurement and aerodynamics of hovering droneflies. *Journal of Experimental Biology,* **211,** pp. 2014-2025.

[115]**Lutz, F. E.** (1927). Wind and the direction of insect flight. *American Museum Novitates,* **29,** pp. 1-4.

[116]**Mardia, K. V.** (1976). Linear-angular correlation coefficients and rhythmometry. *Biometrika,* pp. 403-405.

[117]**Marshall, J.** (1935). On the sensitivity of the chemoreceptors on the antenna and fore-tarsus of the honey-bee, *Apis mellifica L. Journal of Experimental Biology,* **12,** pp. 17-26.

[118]**Mattingly, J. D.** (2002). *Aircraft Engine Design.* American Institute of Aeronautics and Astronautics, Inc.

[119]**May, M. L. and Hoy, R. R.** (1990). Leg-induced steering in flying crickets. *Journal of Experimental Biology,* **151,** pp. 485-488.

[120]**McCay, M. G.** (2003). Winds under the rain forest canopy: The aerodynamic environment of gliding tree frogs. *Biotropica,* **35,** pp. 94-102.

[121]**Meredith, M. A. and Stein, B. E.** (1986). Visual, auditory, and somatosensory convergence on cells in superior colliculus results in multisensory integration. *Journal of Neurophysiology,* **56,** pp. 640-662.

[122]**Miller, L. A. and Peskin, C. S.** (2005). A computational fluid dynamics of `clap and fling' in the smallest insects. *Journal of Experimental Biology,* **208,** pp. 195-212.

[123]**Miller, L. A. and Peskin, C. S.** (2009). Flexible clap and fling in tiny insect flight. *Journal of Experimental Biology,* **212,** pp. 3076-3090.

[124]**Moeslund, T. B., Hilton, A. and Krüger, V.** (2006). A survey of advances in vision-based human motion capture and analysis. *Computer Vision and Image Understanding,* **104,** pp. 90-126.

[125]**Mountcastle, A. and Daniel, T.** (2009). Aerodynamic and functional consequences of wing compliance. *Experiments in Fluids,* **46,** pp. 873-882.

[126]**Mronz, M. and Lehmann, F.** (2008). The free-flight response of *Drosophila* to motion of the visual environment. *Journal of Experimental Biology,* **211,** pp. 2026-2045.

[127]**Nachtigall, W. and Hanauer-Thieser, U.** (1992). Flight of the honeybee. V. Drag and lift coefficients of the bee's body; implications for flight dynamics. *Journal of Comparative Physiology. B: Biochemical, Systemic and Environmental Physiology,* **162,** pp. 267-277.

[128]**Neuhaus, W. and Wohlgemuth, R.** (1960). Über das Fächeln der Bienen und dessen Verhältnis zum Fliegen. *Zeitschrift fur Vergleichende Physiologie,* **43,** pp. 615-641.

[129]**Ortega-Jimenez, V. M., Greeter, J. S. M., Mittal, R. and Hedrick, T. L.** (2013). Hawkmoth flight stability in turbulent vortex streets. *Journal of Experimental Biology,* **216,** pp. 4567-4579.

[130]**Parry, D. A.** (1947). The function of the insect ocellus. *Journal of Experimental Biology,* **24,** pp. 211-219.

[131]**Pennycuick, C. J.** (1960). Gliding flight of the Fulmar petrel. *Journal of Experimental Biology,* **37,** pp. 330-338.

[132]**Pennycuick, C. J.** (1968). A wind-tunnel study of gliding flight in the pigeon *Columba Livia*. *Journal of Experimental Biology,* **49,** pp. 509-526.

[133]**Preiss, R. and Gewecke, M.** (1991). Compensation of visually simulated wind drift in the swarming flight of the dessert locust (*Schistocerca gregaria*). *Journal of Experimental Biology,* **157,** pp. 461-481.

[134]**Pringle, J. W. S.** (1948). The gyroscopic mechanism of the halteres of *Diptera*. *Philosophical Transactions of the Royal Society of London B: Biological Sciences,* **233,** pp. 347-384.

[135]**Ravi, S., Crall, J. D., Fisher, A. and Combes, S. A.** (2013). Rolling with the flow: bumblebees flying in unsteady wakes. *Journal of Experimental Biology,* **216,** pp. 4299-4309.

[136]**Richter, C. and Lipson, H.** (2011). Untethered hovering flapping flight of a 3D-printed mechanical insect. *Artificial Life,* pp. 73–86.

[137]**Riskin, D. K., Iriarte-Díaz, J., Middleton, K. M., Breuer, K. S. and Swartz, S. M.** (2010). The effect of body size on the wing movements of *pteropodid* bats, with insights into thrust and lift production. *Journal of Experimental Biology,* **213,** pp. 4110-4122.

[138]**Ristroph, L.** (2011). Paddling mode of forward flight in insects. *Physical Review Letters,* **106,** pp. 178103.

[139]**Ristroph, L., Bergou, A. J., Ristroph, G., Coumes, K., Berman, G. J., Guckenheimer, J., Wang, Z. J. and Cohen, I.** (2010). Discovering the flight autostabilizer of fruit flies by inducing aerial stumbles. *Proceedings of the National Academy of Sciences,* **107,** pp. 4820–4824.

[140]**Ristroph, L., Berman, G. J., Bergou, A. J., Wang, Z. J. and Cohen, I.** (2009). Automated hull reconstruction motion tracking (HRMT) applied to sideways maneuvers of free-flying insects. *Journal of Experimental Biology,* **212,** pp. 1324-1335.

[141]**Ristroph, L., Ristroph, G., Morozova, S., Bergou, A. J., Chang, S., Guckenheimer, J., Wang, Z. J. and Cohen, I.** (2013). Active and passive stabilization of body pitch in insect flight. *Journal of the Royal Society Interface,* **10,** pp. 20130237.

[142]**Robertson, R. M. and Johnson, A. G.** (1993). Collision avoidance of flying locusts: Steering torques and behaviour. *Journal of Experimental Biology,* **183,** pp. 35-60.

[143]**Rohrseitz, N. and Fry, S. N.** (2011). Behavioural system identification of visual flight speed control in *Drosophila melanogaster*. *Journal of the Royal Society Interface,* **8,** pp. 171-185.

[144]**Sachs, L.** (1978). *Angewandte Statistik.* Berlin: Axel Springer.

[145]**Sandeman, D. C. and Markl, H.** (1980). Head movements in flies (*Calliphora*) produced by deflexion of the halteres. *Journal of Experimental Biology,* **85,** pp. 43-60.

[146]**Sane, S. P., Dieudonné, A., Willis, M. A. and Daniel, T. L.** (2007). Antennal mechanosensors mediate flight control in moths. *Science,* **315,** pp. 863-866.

[147]**Sane, S. P.** (2003). The aerodynamics of insect flight. *Journal of Experimental Biology,* **206,** pp. 4191-4208.

[148]**Sane, S. P. and Dickinson, M. H.** (2002). The aerodynamic effects of wing rotation and a revised quasi-steady model of flapping flight. *Journal of Experimental Biology,* **205,** pp. 1087-1096.

[149]**Schilstra, C. and Hateren, J. H.** (1999). Blowfly flight and optic flow. I. Thorax kinematics and flight dynamics. *Journal of Experimental Biology,* **202,** pp. 1481-1490.

[150]**Scholz, J. P.** (1989). Reliability and validity of the WATSMART three-dimensional optoelectric motion analysis system. *Physical Therapy,* **69,** pp. 679-689.

[151]**Scholz, J. P. and Millford, J. P.** (1993). Accuracy and precision of the PEAK performance technologies motion measurement system. *Journal of Motor Behavior,* **25,** pp. 2-7.

[152]**Schützner, P.** (2016). *Time-resolved analysis of wing and body kinematics in freely maneuvering wild-type and transgenic fruit flies Drosophila.* Institute of Neurobiology, University of Ulm, Germany.

[153]**Sherman, A. and Dickinson, M. H.** (2003). A comparison of visual and haltere-mediated equilibrium reflexes in the fruit fly *Drosophila melanogaster*. *Journal of Experimental Biology,* **206,** pp. 295-302.

[154]**Shishkin, A., Schützner, P., Wagner, C. and Lehmann, F.** (2012). Experimental quantification and numerical simulation of unsteady flow conditions during free flight maneuvers of insects (ed. C. Tropea and H. Bleckmann). *Nature-Inspired Fluid Mechanics* Springer Berlin Heidelberg, pp. 65-79.

[155]**Shyy, W., Lian, Y., Tang, J., Liu, H., Trizila, P., Stanford, B., Bernal, L., Cesnik, C., Friedmann, P. and Ifju, P.** (2008). Computational aerodynamics of low Reynolds number plunging, pitching and flexible wings for MAV applications. *Acta Mechanica Sinica,* **24,** pp. 351-373.

[156]**Simmons, P. J.** (1982). The function of insect ocelli. *Trends in Neurosciences,* **5,** pp. 182-183.

[157]**Sohal, R. S.** (1982). Oxygen consumption and life span in the adult male housefly, *Musca domestica*. *Age,* **5,** pp. 21-24.

[158]**Sponberg, S. and Full, R. J.** (2008). Neuromechanical response of musculo-skeletal structures in cockroaches during rapid running on rough terrain. *Journal of Experimental Biology,* **211,** pp. 433-446.

[159]**Stark, W. and Johnson, M. A.** (1980). Microspectrophotometry of *Drosophila* visual pigments: Determinations of conversion efficiency in R1-6 receptors. *Journal of Comparative Physiology,* **140,** pp. 275-286.

[160]**Stengel, R. F.** (2004). *Flight Dynamics.* Princeton University Press.

[161]**Sterbing-D'Angelo, S., Chadha, M., Chiu, C., Falk, B., Xian, W., Barcelo, J., Zook, J. M. and Moss, C. F.** (2011). Bat wing sensors support flight control. *Proceedings of the National Academy of Sciences,* **108,** pp. 11291-11296.

[162]**Stuart, A. M.** (1958). The efficiency of adaptive structures in the nymph of *Rhithrogena Semicolorata* (Curtis) (*Ephemeroptera*). *Journal of Experimental Biology,* **35,** pp. 27-38.

[163]**Stull, R. B.** (1988). *An Introduction to Boundary Layer Meteorology.* Dordrecht: Kluwer Academic Publishers.

[164]**Suga, N. and Katsuki, Y.** (1961). Central mechanism of hearing in insects. *Journal of Experimental Biology,* **38,** pp. 545-558.

[165]**Sun, M., Wang, J. and Xiong, Y.** (2007). Dynamic flight stability of hovering insects. *Acta Mechanica Sinica,* **23,** pp. 231-246.

[166]**Sun, M. and Wu, J. H.** (2003). Aerodynamic force generation and power requirements in forward flight in a fruit fly with modeled wing motion. *Journal of Experimental Biology,* **206,** pp. 3065-3083.

[167]**Sun, M. and Xiong, Y.** (2005). Dynamic flight stability of a hovering bumblebee. *Journal of Experimental Biology,* **208,** pp. 447-459.

[168]**Swartz, S. M., Breuer, K. S. and Willis, D. J.** (2008). Aeromechanics in aeroecology: flight biology in the aerosphere. *Integrative and comparative biology,* **48,** pp. 85-98.

[169]**Taylor, G. K. and Thomas, A. L. R.** (2002). Animal flight dynamics II. Longitudinal stability in flapping flight. *Journal of Theoretical Biology,* **214,** pp. 351-370.

[170]**Taylor, G. J., Luu, T., Ball, D. and Srinivasan, M. V.** (2013). Vision and air flow combine to streamline flying honeybees. *Nature,* **3,** pp. 1-11.

[171]**Taylor, G. K. and Krapp, H. G.** (2007). Sensory systems and flight stability: What do insects measure and why? (ed. J. Casas and S.J. Simpson). *Advances in Insect Physiology* Academic Press, pp. 231-316.

[172]**Tobalske, B. W., Warrick, D. R., Clark, C. J., Powers, D. R., Hedrick, T. L., Hyder, G. A. and Biewener, A. A.** (2007). Three-dimensional kinematics of hummingbird flight. *Journal of Experimental Biology,* **210,** pp. 2368-2382.

[173]**Usherwood, J. R., Stavrou, M., Lowe, J. C., Roskilly, K. and Wilson, A. M.** (2011). Flying in a flock comes at a cost in pigeons. *Nature,* pp. 494-497.

[174]**van Breugel, F., Ern Teoh, Z. and Lipson, H.** (2010). A passively stable hovering flapping micro-air vehicle (ed. D. Floreano, J.-C. Zufferey, M. V. Srinivasan and C. Ellington). Springer Berlin Heidelberg, pp. 171-184.

[175]**van Breugel, F., Regan, W. and Lipson, H.** (2008). From insects to machines. *Robotics & Automation Magazine, IEEE,* **15,** pp. 68-74.

[176]**Vance, J. T., Faruque, I. and Humbert, J. S.** (2013). Kinematic strategies for mitigating gust perturbations in insects. *Bioinspiration and Biomimetics,* **8,** pp. 016004.

[177]**Vogel, S.** (1981). *Life in Moving Fluids: The Physical Biology of Flow*. Princeton University Press.

[178]**Vogel, S.** (1966). Flight in *Drosophila*. *Journal of Experimental Biology,* **44,** pp. 567-578.

[179]**Voss, F.** (1914). Vergleichende Untersuchungen über die Flugwerkzeuge der Insekten. Einleitendes. *Verhandlungen der Deutschen Gesellschaft,* **24,** pp. 118-142.

[180]**Wagner, H.** (1986). Flight performance and visual control of flight of the free-flying housefly (*Musca Domestica L.*) I. Organization of the flight motor. *Philosophical Transactions of the Royal Society of London B: Biological Sciences,* **312,** pp. 527-551.

[181]**Walker, J. A.** (2002). Rotational lift: something different or more of the same? *Journal of Experimental Biology,* **205,** pp. 3783-3792.

[182]**Walker, S. M., Thomas, A. L. R. and Taylor, G. K.** (2008). Deformable wing kinematics in the desert locust: how and why do camber, twist and topography vary through the stroke? *Journal of the Royal Society Interface,* **6,** pp. 734-747.

[183]**Wang, Z. J.** (2000). Two dimensional mechanism for insect hovering. *Physical Review Letters,* **85,** pp. 2216-2219.

[184]**Wang, H., Zeng, L., Liu, H. and Yin, C.** (2003). Measuring wing kinematics, flight trajectory and body attitude during forward flight and turning maneuvers in dragonflies. *Journal of Experimental Biology,* **206,** pp. 745-757.

[185]**Wang, Z. J.** (2005). Dissecting insect flight. *Annual Review of Fluid Mechanics,* **37,** pp. 183-210.

[186]**Washburn, J. O. and Washburn, L.** (1984). Active aerial dispersal of minute wingless arthropods: Exploitation of boundary-layer velocity gradients. *Science,* **223,** pp. 1088-1089.

[187]**Wehrhahn, C., Poggio, T. and Bülthoff, H.** (1974). Tracking and chasing in houseflies (*Musca*). *Biological Cybernetics,* **45,** pp. 123-130.

[188]**Weimerskirch, H., Bonadonna, F., Bailleul, F., Mabille, G., Dell'Omo, G. and Lipp, H.** (2002). GPS tracking of foraging albatrosses. *Science,* **295,** pp. 1259-1259.

[189]**Weimerskirch, H., Martin, J., Clerquin, Y., Alexandre, P. and Jiraskova, S.** (2001). Energy saving in flight formation. *Nature,* **413,** pp. 697-698.

[190]**Weis-Fogh, T. and Alexander, R. M.** (1977). The sustained power output from striated muscle. *In Scale Effects in Animal Locomotion (ed. T.J. Pedley),* pp. 511–525.

[191]**Weis-Fogh, T.** (1949). An aerodynamic sense organ stimulating and regulating flight in locusts. *Nature,* **164,** pp. 873-874.

[192]**White, F.** (2006). *Viscous Fluid Flow.* McGraw-Hill Higher Education.

[193]**Wootton, R. J., Herbert, R. C., Young, P. G. and Evans, K. E.** (2003a). Approaches to the structural modelling of insect wings. *Philosophical Transactions of the Royal Society of London B: Biological Sciences,* **358,** pp. 1577-1587.

[194]**Wootton, R. J., Herbert, R. C., Young, P. G. and Evans, K. E.** (2003b). Approaches to the structural modelling of insect wings. *Philosophical Transactions of the Royal Society of London B: Biological Sciences,* **358,** pp. 1577-1587.

[195]**Wootton, R. J.** (1992). Functional morphology of insect wings. *Annual Review of Entomology,* **37,** pp. 113-140.

[196]**Yanoviak, S. P., Munk, Y., Kaspari, M. and Dudley, R.** (2010). Aerial manoeuvrability in wingless gliding ants (*Cephalotes atratus*). *Proceedings of the Royal Society of London. B: Biological Sciences,* **277,** pp. 2199-2204.

[197]**Yorozu, S., Wong, A., Fischer, B. J., Dankert, H., Kernan, M. J., Kamikouchi, A., Ito, K. and Anderson, D. J.** (2009). Distinct sensory representations of wind and near-field sound in the *Drosophila* brain. *Nature,* **458,** pp. 201-205.

[198]**Zanker, J. M.** (1990). The wing beat of *Drosophila melanogaster*. I. Kinematics. *Philosophical Transactions of the Royal Society of London. B, Biological Sciences,* **327,** pp. 1-18.

[199]**Zanker, J.** (1988). How does lateral abdomen deflection contribute to flight control of *Drosophila melanogaster*? *Journal of Comparative Physiology A,* **162,** pp. 581-588.

[200]**Zar, J. H.** (2010). *Biostatistical Analysis.* Pearson Prentice Hall.

[201]**Zdunich, P., Bilyk, D., MacMaster, M., Loewen, D., DeLaurier, J., Kornbluh, R., Low, T., Stanford, S. and Holeman, D.** (2007). Development and testing of the mentor flapping-wing micro air vehicle. *Journal of Aircraft,* **44,** pp. 1701-1711.

[202]**Zhang, Y. and Sun, M.** (2010). Dynamic flight stability of a hovering model insect: lateral motion. *Acta Mechanica Sinica,* **26,** pp. 175-190.

7. Personal details

Name:	Mohd Nazri Mohd Nasir
Date of birth:	24th June 1982
Place of birth:	Melaka, Malaysia

Education:

January 1989-November 1994	Chenderah Primary School, *Jasin, Melaka, Malaysia*
January 1995-November 1997	Sultan Muhammad Secondary School, *Batu Berendam, Melaka, Malaysia*
January 1998-November 1999	MARA Junior Science College, *Terendak Camp, Melaka, Malaysia*
June 2000-April 2003	Universiti Teknologi MARA, *Shah Alam, Selangor, Malaysia* Diploma in Mechanical Engineering (Aerospace)
September 2003-April 2005	The University of Manchester, *Manchester, United Kingdom* Bachelor of Engineering in Aerospace Engineering
September 2006-April 2008	Delft University of Technology, *Delft, The Netherlands* Master of Science (Aerospace Engineering)

PhD Study:

September 2009-December 2015	University of Ulm, *Ulm, Germany* Technical University of Darmstadt, *Darmstadt, Germany*
Supervisor	Prof. Dr. Fritz-Olaf Lehmann, Rostock Prof. Dr.-Ing. Cameron Tropea, Darmstadt
Founding agency	Ministry of Education, *Malaysia* Universiti Teknologi Malaysia, *Malaysia* German Science Foundation

Internship:

October 2003-November 2003	Malaysia Airline System (MAS), *Subang, Malaysia*